Title
The Beginnings of Cold Ion Outflow at Mars: Supply and Energization near the Exobase

Author
Hanley, Kathleen Gwen

Publication Date
2023

Peer reviewed|Thesis/dissertation

The Beginnings of Cold Ion Outflow at Mars: Supply and Energization near the Exobase

by

Kathleen Gwen Hanley

A dissertation submitted in partial satisfaction of the

requirements for the degree of

Doctor of Philosophy

in

Physics

in the

Graduate Division

of the

University of California, Berkeley

Committee in charge:

Doctor David Mitchell, Co-chair
Professor Stuart Bale, Co-chair
Professor Forrest Mozer
Professor Imke de Pater

Spring 2023

The Beginnings of Cold Ion Outflow at Mars: Supply and Energization near the Exobase

Abstract

The Beginnings of Cold Ion Outflow at Mars: Supply and Energization near the Exobase

by

Kathleen Gwen Hanley

Doctor of Philosophy in Physics

University of California, Berkeley

Doctor David Mitchell, Co-chair

Professor Stuart Bale, Co-chair

The study of planetary ionospheres dates back thousands of years, to humanity's first attempts to explain the polar aurora. Ionospheric physics is a study of one pathway for energy to enter a planetary atmosphere: transfer from sunlight and solar wind plasma to planetary plasma, and from the planetary plasma to the neutral atmosphere. In the modern era of ionospheric physics, electrostatic analyzers with attached time-of-flight velocity analyzers are excellent tools for the study of planetary ionospheres because they can measure mass-resolved 3-dimensional ion velocity distribution functions over a wide range of energies and fluxes, with large fields-of-view and moderate angular resolution.

One example of an electrostatic analyzer with attached time-of-flight section is the SupraThermal And Thermal Ion Composition (STATIC) instrument onboard the Mars Atmosphere and Volatile EvolutioN (MAVEN) mission. MAVEN has been collecting data since 2014 with the goal of illuminating how Martian climate and habitability have been affected by the escape of the atmosphere to space. To that end, STATIC was designed to measure the main ionospheric and escaping species, operating from deep in the collisional atmosphere out to the tenuous exosphere and magnetotail. STATIC samples ion velocity distribution functions every 4 seconds across a field-of-view covering 2π steradians for ions with energies between 0.1 eV and 30 keV and masses between 1 and 60 amu. This work will treat STATIC as a case study in order to examine some of the challenges associated with using electrostatic analyzers in space, including the effects of background counts, spacecraft potential, and supersonic spacecraft motion on the measurement and analysis of distribution functions. Before the discussion of those details, we first provide an introduction to the geometry of electrostatic analyzers and how the measured count rates are related to physical quantities.

This work also describes the results of several investigations in which MAVEN-STATIC data were used to examine the beginnings of cold ion outflow at Mars. Models of the Martian

ionosphere show that the vast majority of ions are created at altitudes near 120 km, the location of the main ionospheric peak. The peak is located deep in the collisional atmosphere, where collisions are theorized to keep the ions in thermal equilibrium with the cold neutral atmosphere. The vast majority of the ionospheric ions are therefore gravitationally bound to the planet. Most ions that have the potential to escape the planet's gravity are created near a boundary called the exobase, where the mean free path between collisions becomes equal to the scale height and the ions no longer thermalize with the neutrals. The exobase can be considered the top of the collisional atmosphere and varies between 140 and 210 km altitude dependent on local time and season. In the present epoch, 10-20% of atmospheric loss is attributable to the loss of ions from hundreds or thousands of kilometers above the main peak and the exobase region. The mechanisms by which ions gain enough energy to escape the planet's gravity between the exobase and the altitudes where they escape are not yet understood, but we have used STATIC data to begin analysis of ion distribution functions in the vicinity of the exobase.

The analysis of ion velocity distribution functions measured near the exobase is experimentally challenging because the spacecraft travels supersonically with respect to the cold ions, affecting observations of both the energy and angular distributions. The details of how the instrumentation affects measurements of the distribution function must be understood in detail in order to extract accurate plasma parameters. In this work, we describe many of the procedures used to extract accurate plasma parameters from STATIC data. We use these corrections to begin to bridge the gap between studies of ion outflow conducted high above the exobase and studies of the cold, thermal ionosphere near the main peak.

Specifically, we report the first measurements of Martian ionospheric ion temperatures since the Viking landers in 1975 and 1976, including the results of both a case study and a statistical study of over 10,000 MAVEN orbits. Unexpectedly, ion temperatures are significantly elevated over neutral gas temperatures many scale heights below the exobase, and none of the obvious mechanisms for ion heating explained the observed temperature difference. This surprising result was noted both in the case study and the study using the majority of the STATIC dataset, suggesting that a fundamental piece of physics is missing from current models of the Martian ionosphere.

Finally, we also report the results of a statistical study with the goal of determining where signatures of ion energization are observed in STATIC data. By fitting the measured distribution functions with drifting Maxwell-Boltzmann distributions, we identified distributions in which suprathermal ions produced a significant portion of the measured energy flux. Most distributions are well-described by the Maxwell-Boltzmann distribution below the exobase region—in other words, the neutral atmosphere dominates low-altitude ion dynamics. Suprathermal ions are observed just above the exobase at all solar zenith angles. A comparison of results inside and outside Mars' strong crustal magnetic field regions showed that more thermal plasma is observed inside crustal fields on the dayside, while more suprathermal plasma is observed inside crustal fields on the nightside. These results suggest

that crustal fields shield dayside plasma from energization by the solar wind while enhancing energization and outflow on the nightside.

The techniques developed in this work provide tools for continued investigation into the physics of initial ion acceleration at Mars using STATIC data, while the results reported here provide context for case studies in which the processes responsible for ion acceleration can be analyzed. The study of initial ion acceleration at Mars is just one context in which electrostatic analyzers in combination with time-of-flight analyzers provide insight into the physics that cannot be matched by any other instrument.

For my Mom, who has given me everything

Contents

List of Figures

List of Tables

Acknowledgments

It takes a village to write a thesis, and this thesis would not have been written without my village. I am so lucky to have so many people to thank for helping me get to where I am today.

To my advisors, Dave, Jim, and Chris, your knowledge and mentorship are unmatched and I cannot thank you enough. Working with you for the last five years has given me the knowledge and confidence I needed to truly call myself a scientist. Thank you also to those who helped me to stay on track in the Berkeley Physics department—Stuart Bale, Joelle Miles, Jonathan Wurtele, Forrest Mozer, and Imke de Pater. And a special thank you to Dave Brain. Dave, I asked you for a reference letter and instead you offered me a job with the MAVEN team, setting me on a path that has been so rewarding for me.

I want to acknowledge the legacy of Chuck Carlson, the inventor of the top hat analyzer, without whom none of the work in this thesis would be possible. My thanks also to all of my collaborators who helped to shape each chapter of this work, as well as Davin Larson and everyone else who has contributed a piece of software to the IDL SPEDAS library.

My sincerest gratitude to my family and friends, whose unwavering support has shaped me into the person I am today. Mom, Dad, Morgan, and all of my grandparents—I am so thankful to have spent my life with you as my loudest cheerleaders. Thank you for everything. And to my found family, especially my roommates, Oscar and Danielle, I will never be able to thank you enough for accepting me with open arms and supporting me with all your hearts. I love you all!

Next, a shoutout to all the students and postdocs who have commiserated with me over the years—Eryn, Roger, Melissa, Sky, Annie Kate, Andréa, Murti, Neesha, Rebecca, Ace, Chris, Milo, Brackney, Charlie, Tracy, Shane, and many more whom I'm sure I'm forgetting. Thanks for all the sympathy, and let me know if you ever want thesis comments from me!

Finally, to all the others that have helped out along the way—the entire SSL Planetary Science Division, especially Shaosui, Rob, Shannon, Roberto, Phyllis, and Abby; Andy Nagy; Bill Peterson; the Brain group; the Bale group; and my other Physics and EPS peers—thank you for your support, your questions, your critiques, and all the free food.

Chapter 1

Introduction

1.1 An Introduction to Planetary Ionospheres

Any planetary object with a neutral gas atmosphere in the presence of a star is likely to have an ionosphere, a layer of ionized gas where free electrons and ions exist in equal numbers. This layer of ionized gas interacts collisionally with the neutral atmosphere and electromagnetically with the stellar wind flowing out from the star, providing an additional pathway for the star to deposit energy into the planetary system. Study of Earth's ionosphere dates back thousands of years to when people first tried to explain the beautiful aurora dancing in the polar skies. However, the origin of the aurora was only correctly theorized as being a result of "the electric corpuscles from the sun drawn in out of space" in 1908 by Kristian Birkeland. In this introduction, we will establish a theoretical understanding of ionospheres, including how they form and how energy flows between different species, in order to set the stage for the research that will be presented in later chapters.

Theory of the Dayside Ionosphere

The existence of the ionosphere is a natural consequence of the interaction of stellar radiation with a neutral gas atmosphere, whether that atmosphere is bound to its parent body due to gravity (e.g. a planet) or transient (e.g. a comet). As radiation of appropriate wavelengths to ionize the major neutral species is absorbed by the dayside atmosphere, ions and electrons are created in equal numbers. These ions and free electrons interact with the neutral atmosphere via ballistic collisions, with each other via Coulomb collisions, and with the electric and magnetic fields. Chemical reactions can transfer energy between different species, and plasma transport can transfer energy to different regions of the ionosphere.

A general description of the dayside ionosphere of a planet was published by Chapman in 1931 [11]. Chapman described the interaction of ionizing radiation with a neutral atmosphere in hydrostatic equilibrium. For simplicity, we make the additional assumptions here that the atmosphere is a single species and isothermal. In this case, the atmospheric number density n falls off exponentially with altitude z with a scale height H determined by the gas temperature

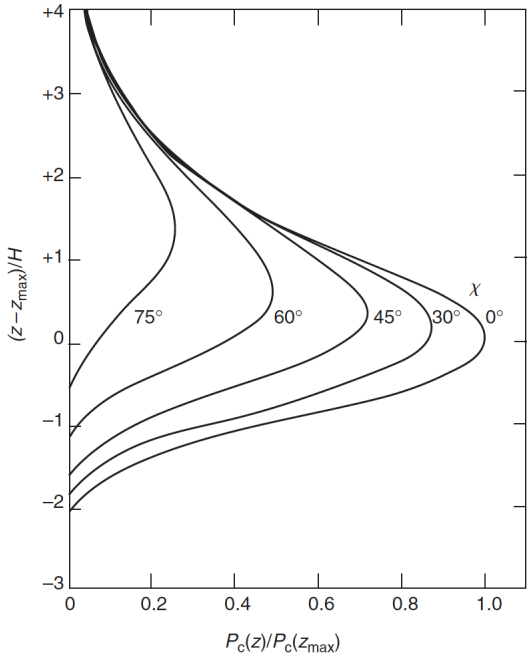

Figure 1.1: Normalized Chapman ion production rates as a function of altitude z (in units of scale height H) and solar zenith angle χ, reproduced from [84].

T, its molecular mass m, and the acceleration due to gravity g:

$$n(z) = n_0 \exp\left(\frac{-mg(z-z_0)}{kT}\right) = n_0 \exp\left(\frac{-(z-z_0)}{H}\right) \tag{1.1}$$

where k is Boltzmann's constant and n_0 is the density at a reference altitude z_0 (called z_{max} in Figure 1.1). For such an atmosphere, the Chapman function $Ch(z_0, \chi_0)$ relates the column density of the plasma to neutral gas density, altitude, and the angle of incidence of the ionizing radiation χ:

$$\int_{z_0}^{\infty} n(z) ds_\lambda = n(z_0) H(z_0) Ch(z_0, \chi_0) \tag{1.2}$$

where ds_λ is the path length through the atmosphere for radiation of wavelength λ. An example of Chapman function ion production rates is shown in Figure 1.1. The plasma density is highest at the altitude at which the optical depth for the ionizing radiation reaches unity, meaning that the peak density occurs at higher altitudes for more oblique angles of incidence. The χ dependence means that the angle between local zenith and the position of the star in the sky, called solar zenith angle (SZA) if the star is our Sun, is a useful coordinate for understanding the local structure and energetics in an ionosphere. For a plane-stratified

atmosphere, $ds_\lambda = \sec\,\chi\; dz$, meaning $Ch(z_0, \chi_0) = \sec\,\chi_0$, which is a good approximation for $\chi < 75°$ [84]. In the absence of the plane parallel approximation, the Chapman function is determined analytically and is highly useful for characterizing the ionosphere at higher SZAs.

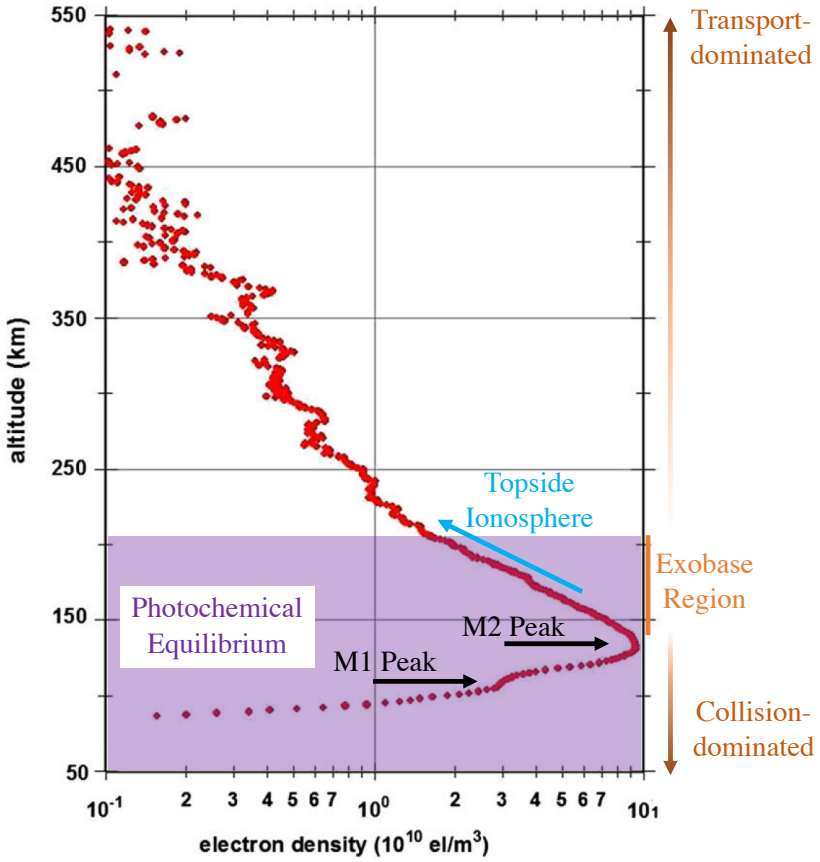

Figure 1.2: Regions of Mars' ionosphere overlaid on a typical electron density profile obtained from Mars Express radio occultation data, modified from [93]. See text for an explanation of the features.

In addition to SZA, ionospheric plasma is also highly structured with respect to altitude. An example of this structure in the Martian ionosphere is shown in Figure 1.2. Ionospheres are typically separated into two regions, the collision-dominated lower ionosphere and the collisionless, transport-dominated upper ionosphere, with a transition layer in between. These regions are indicated by the brown arrows on the right of Figure 1.2. In the lower ionosphere, ion dynamics are controlled by the cold, dense neutral atmosphere due to high ion-neutral collision rates. The two peaks labeled M1 and M2 in Figure 1.2 are the result of photoionization by photons of different wavelengths; higher energy photons can penetrate deeper into the atmosphere before being absorbed.

The exobase region, where the mean free path between collisions becomes equal to the gas scale height, marks the transition region to the upper ionosphere. The exobase is marked by a solid orange line on the right of Figure 1.2. Up to the top of the exobase region, the ionosphere is in photochemical equilibrium (i.e. local ion production rates equal loss rates, and the density profile is well-described by a Chapman function). The photochemical equilibrium region is marked in purple in Figure 1.2. Within a few scale heights above the exobase, collision rates drop dramatically and electromagnetism begins to influence ion motion. Even on bodies with no intrinsic magnetic field, the stellar wind carries a magnetic field that interacts with planetary plasma. In this altitude regime, plasma can be transported large distances by electromagnetic forces, so the dynamics are determined by the fields, and can be highly sensitive to high-altitude interaction with the stellar wind. The remainder of this work will focus on planetary bodies in our solar system, so we will refer to the stellar wind as the solar wind.

This high-altitude interaction controls the vertical extent of the ionosphere. The altitude region above the main peak is often referred to as the "topside," as shown by the blue arrow in Figure 1.2. For many ionospheres, e.g. those of Venus and comets, the upper boundary of the topside is formed by the balance between the dynamic pressure of the solar wind and the thermal pressure of the ionospheric plasma. Such a boundary is called an "ionopause." This model assumes pressure balance throughout the system, as solar wind plasma does not interact directly with ionospheric plasma. That is, the dynamic pressure of the solar wind is assumed to be equal to the thermal and dynamic pressure of the plasma behind the bowshock formed by the solar wind deflecting past the planetary obstacle; in turn, that pressure is assumed equal to the thermal plasma pressure in the ionosphere. The ionopause is identified by a dramatic decrease in planetary plasma density; it moves inward and outward as the dynamic pressure of the solar wind varies and pressure balance requires different ionospheric density. The ionopause would be indicated by the top of the orange region in the illustration of Mars' induced magnetosphere in Figure 1.3; however, the term is not typically used in the Mars community because a sharp decrease in plasma density is often not observed at Mars. (Indeed, such a feature is not visible in Figure 1.2.) Instead, a sharp change in plasma composition from planetary heavy plasma to solar wind plasma is typically observed at a boundary referred to as the "ion composition boundary."

So far we have described the production and structure of the dayside ionosphere, but not how energy is transported through it. Figure 1.4 is a block diagram illustrating how energy flows from the Sun, through the ionosphere, and is eventually deposited into the neutral atmosphere. Energy is input in the form of extreme ultraviolet (EUV) and X-ray photons, which can directly deposit energy into neutrals via photodissociation or by exciting a bound electron. Some fraction of EUV and X-ray photons create ion-electron pairs, depositing most of the energy into the lighter electrons. The electrons then transfer energy to ions or neutrals via collisions. Thermal equilibrium for ions is maintained by balancing energy input from Coulomb collisions with electrons and energy output into neutrals via chemistry or ballistic collisions. Conduction, diffusion, and electromagnetic transport processes redistribute energy spatially.

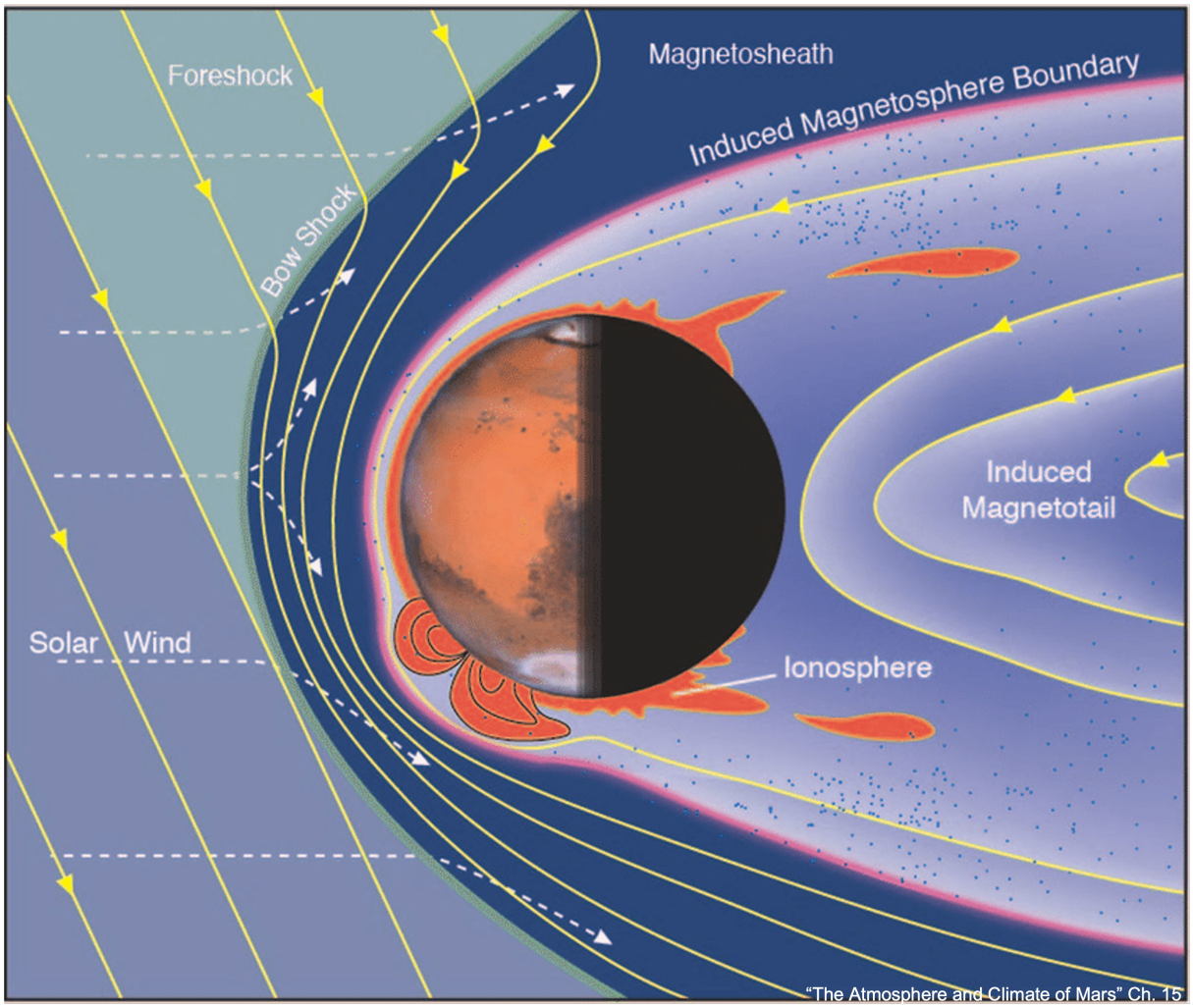

Figure 1.3: A cartoon of the Martian magnetosphere, reproduced from [7]. Yellow solid lines represent solar wind magnetic field lines, while white dashed lines represent the flow of solar wind plasma. Orange regions indicate cold planetary plasma while blue dots represent ions picked up by the solar wind convection electric field. Planetary crustal magnetic fields trap cold plasma at high altitudes in the Southern hemisphere. The solar wind is shocked as it encounters the planetary obstacle, creating the bowshock and foreshock regions. Inside the magnetosheath, magnetic field lines pile up outside the induced magnetosphere boundary, shown in pink. Behind the planetary obstacle, field lines form an elongated magnetotail as they slide over the poles.

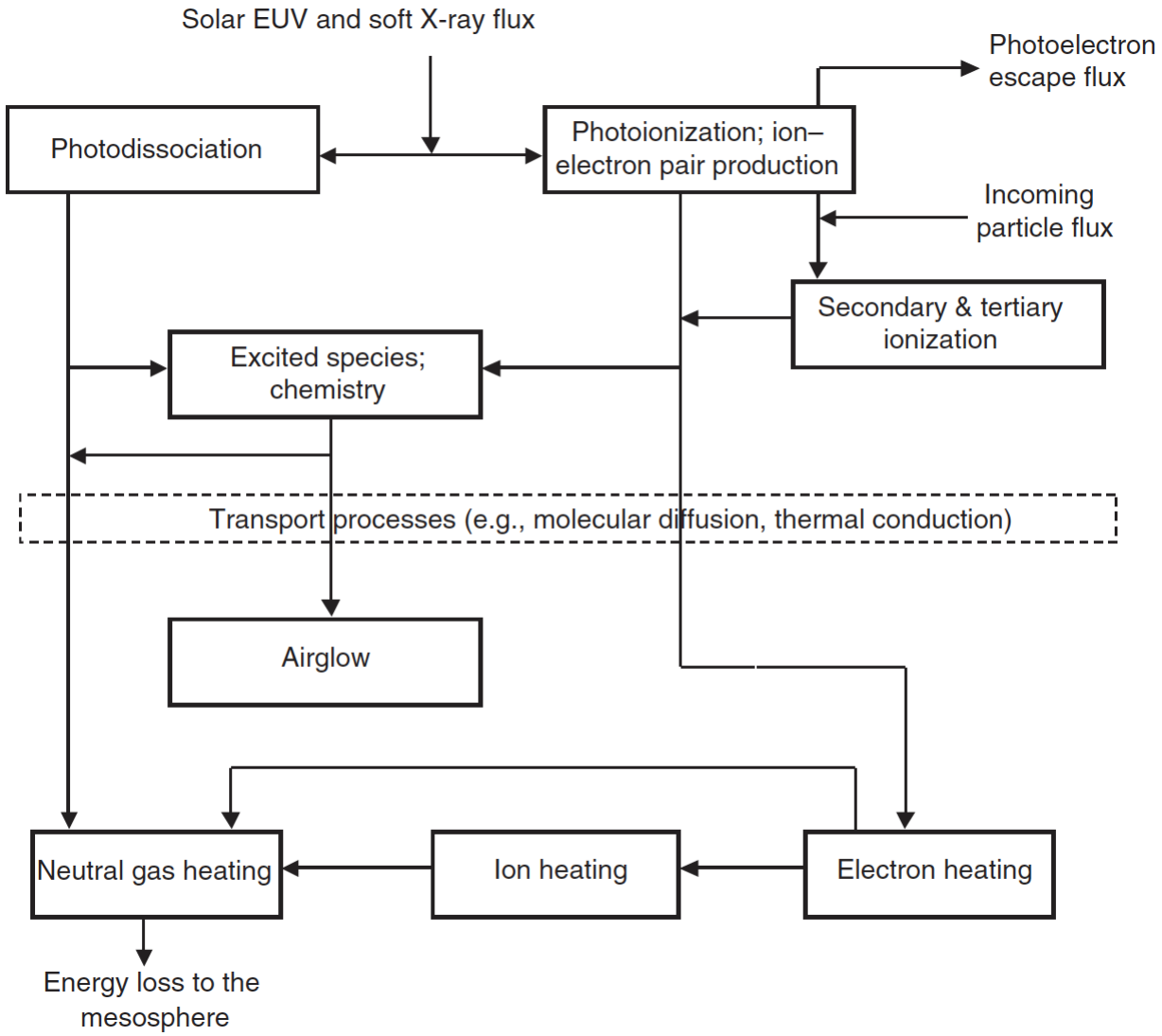

Figure 1.4: A block diagram of energy flow through the ionosphere, reproduced from [84].

In the lower ionosphere, where collisions prevent ion transport with respect to neutral gas, ion and electron temperatures are expected to approach the temperature of the cold neutral atmosphere. There are so many more neutrals than charged particles (at Mars, >6 orders of magnitude more) that the neutrals act as a highly efficient heat sink for the plasma. At higher altitudes, where the plasma is decoupled from the neutrals, temperatures can be higher, especially on the nightside, where densities are lower and solar wind plasma precipitation can deposit large amounts of energy.

Nightside Ionospheric Structure

Our description of the dayside ionosphere relied on a star as a source of energy in the form of photons, which create ions from the neutral gas. On the nightside, where photoionization does not occur, a comprehensive theoretical description of ionospheres is much more difficult. Ions can be transported from the dayside, but eventually recombine with electrons to become neutral. Recombination is strongly dependent on altitude because collision rates drop off rapidly with altitude. Collision cross-sections (and thus rates) are also species-dependent, so as the ionosphere rotates into the night, both the composition and altitude profile change. Some ions, with recombination times of hours or longer, can survive the entire night. However, the only way to create new ions deep on the nightside is via impact ionization. These source mechanisms result in an ionosphere with much lower densities than dayside (1-2 orders of magnitude lower at Mars).

The vertical boundary of the ionosphere is significantly different on the nightside. While the dayside is capped by a pressure-balance boundary or a change in ion composition, the nightside ionosphere is elongated into a "magnetotail" by the flow of stellar plasma. This extended magnetic field geometry, which can be seen in Figure 1.3, allows cold planetary plasma to escape down magnetic field lines (orange blobs in Figure 1.3). For comets, the plasma is not gravitationally bound and escapes down the magnetotail. However, for more massive planetary bodies, only a small fraction of the plasma is able to overcome gravity and escape to space.

1.2 Composition, Structure, and Energy Balance in Mars' Ionosphere

While the previous section aimed to introduce the general concepts associated with planetary ionospheres, here we discuss the details specific to the Mars ionosphere. Dayside ion densities are well-described by a Chapman function [93]. Though Mars' dominant atmospheric neutral is CO_2, the dominant ion is O_2^+ due to a very fast chemical reaction between photoionized CO_2^+ and neutral O [69]. The main ionospheric peak occurs near 120 km altitude at the subsolar point, rising to 180 km near the terminator [67, 40]. The peak is typically deep within the collisional atmosphere, as the exobase region varies between 140 km at night and 210 km at the subsolar point, as well as seasonally [53].

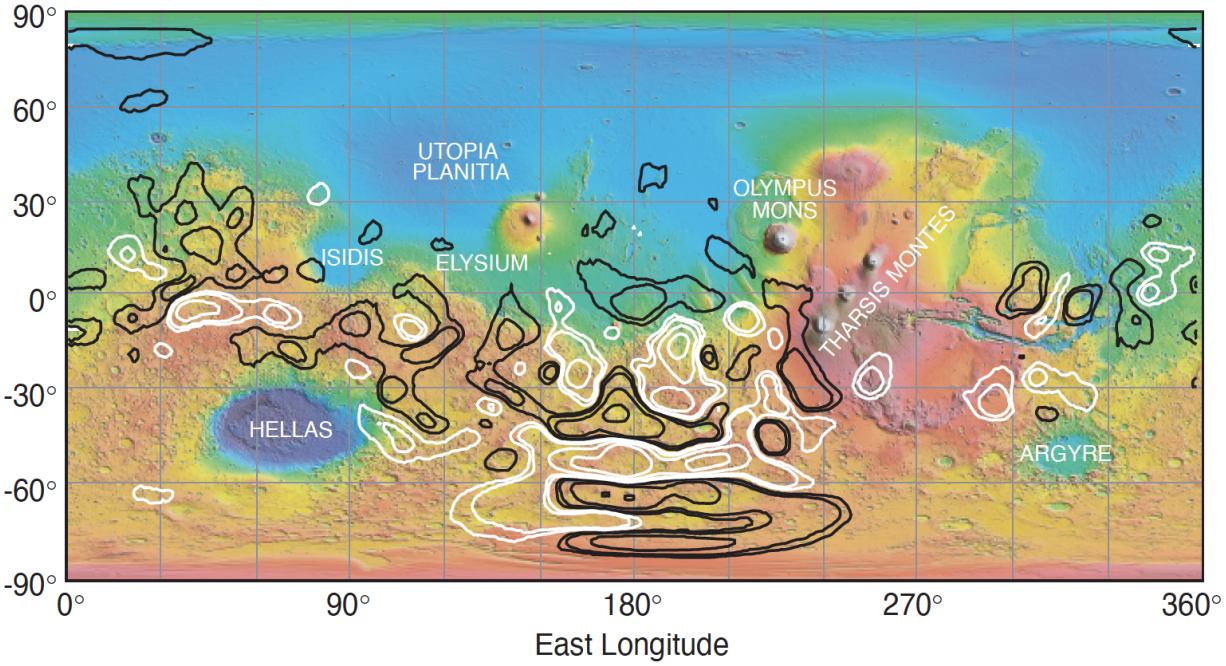

Figure 1.5: Crustal magnetic field contour map overlaid on a map of Mars' topography, reproduced from [15].

On the nightside, Mars' ionosphere is much patchier than on the dayside, where densities vary smoothly with solar zenith angle. This unique characteristic is due to Mars' so-called "hybrid magnetosphere," a combination of an Earth-like global magnetosphere and a Venus-like magnetosphere induced by the solar wind interaction with the ionosphere. A cartoon of the hybrid magnetosphere is shown in Figure 1.3. The Earth-like magnetism is a result of the remnant crustal magnetism discovered by Mars Global Surveyor (MGS) in 1999 [1]. A map of the crustal fields as measured from the 400 km MGS orbit is shown in Figure 1.5. The crustal fields are concentrated in the planet's Southern Hemisphere and create localized "mini-magnetospheres" that are strong enough to stand off the solar wind dynamic pressure despite the lack of a global magnetic field at Mars [55]. These mini-magnetospheres are illustrated by the black magnetic field lines trapping orange planetary plasma in the Southern hemisphere in Figure 1.3. Magnetic cusps, or regions of vertical magnetic field between the mini-magnetospheres, are believed to host phenomena typically associated with global dipole fields, such as aurora [62, 22]. This complicated pattern of magnetic topologies leads to patchiness of Mars' nightside ionosphere, as impact ionization can only occur along magnetic field lines that are "open" to the solar wind at one end. The "closed" mini-magnetospheres prevent impact ionization, leading to regions with very low plasma densities.

Both NASA's MGS and the European Space Agency's Mars Express missions carried

plasma instrumentation to study the upper ionosphere, with their nominal periapsis altitudes at 400 km and 300 km altitude respectively. The first measurements of the lower ionosphere were made by the Viking landers in 1976 [85] and not repeated for 40 years. These landers were equipped with retarding potential analyzers (RPAs) to measure charged particle energy spectra. The RPA measurements were used to derive two profiles of ion density, composition, and temperature as a function of altitude between ∼120-350 km [47]. Since the Viking missions, most efforts of the Mars ionosphere modeling community have gone towards reproducing these two profiles, with varying degrees of success.

The temperature profiles retrieved from Viking data have proven to be more difficult to reproduce than the density profiles. Models typically set the ion temperature equal to the neutral temperature at some altitude below the exobase because high collision rates are expected to force ions and neutrals to equilibrate. At higher altitudes, ion temperature is either estimated from the neutral and electron temperatures or calculated by solving the heat equation, including some topside heat source in order to improve agreement with the Viking data. The nature of this heat source is often unspecified, and the physics of how the energy is transported downwards is not explained. However, understanding how energy is transported through an ionosphere is crucial for understanding how the solar wind drives atmospheric loss and affects planetary climate over geologic timescales.

1.3 The Use of Electrostatic Analyzers to Study Planetary Ionospheres

Since the first detection of Earth's ionosphere via radio waves in 1901, a huge variety of instrumentation has been developed to study charged particles and waves in space environments. In this work, we will investigate one such instrument, the electrostatic analyzer. Electrostatic analyzers (ESAs) have been used to study charged particles in space environments since the early 1960s, when the Solar Plasma Analyzer onboard the Mariner 2 mission to Venus was used to measure the solar wind energy spectrum for the first time [72]. Since solar wind ions are primarily protons and alpha particles traveling at the same speed, experimenters can typically distinguish the two species using an ESA with sufficient energy resolution. However, planetary ionospheres often host a much more varied composition, with ions of different species showing up at similar energies. The addition of a time-of-flight (TOF) velocity analyzer allows for the measurement of mass-resolved three-dimensional velocity distribution functions and makes ESAs ideal instruments for studying planetary ionospheres, albeit with their own associated challenges. One of the earliest examples of such an instrument is the 2001 Cluster ion spectrometry experiment, launched by the European Space Agency to study Earth's magnetosphere [80].

A similar instrument was included onboard the Mars Atmosphere and Volatile EvolutioN (MAVEN) mission, the major goal of which is to understand the effect that atmospheric escape to space has had on Martian climate and habitability [54]. The SupraThermal And

Thermal Ion Composition (STATIC) instrument onboard MAVEN was designed to resolve the main ionospheric and escaping species at Mars, H^+, H_2^+, He^+, O^+, O_2^+, and CO_2^+, while sampling the energy spectra of the dense plasma populations near the ionospheric main peak as well as the tenuous pickup ion populations in the exosphere [70].

The use of an instrument like STATIC in the Mars ionosphere for the first time has provided an unprecedented look at every phase of ion escape, which MAVEN has shown is an important pathway for atmospheric loss in the present epoch [52]. STATIC is equipped with an electrostatic attenuator that provides a factor of 10 reduction in flux, as well as a mechanical attenuator that reduces fluxes by a factor of 100 over half the field-of-view. These attenuators make STATIC capable of measuring ion fluxes over a huge dynamic range, from the ionospheric main peak (where collisional coupling to the neutral atmosphere dominates ion dynamics) to the more tenuous upper ionosphere and magnetosheath (where electromagnetic forces can energize ions). With a programmable 64-step energy sweep and an intrinsic energy resolution of 16%, STATIC can sample ion populations from thermal energies down to 0.1 eV up to highly energetic solar wind particles at 30 keV.

Additionally, STATIC uses electrostatic deflectors, toroidal geometry, and a tophat aperture to achieve a 90°x360° field-of-view. Its location on MAVEN's Articulated Payload Platform means that the instrument can be oriented so that the majority of the ion distribution is nearly always in its field-of-view. In combination with MAVEN's highly inclined, elliptical, precessing orbit, the STATIC design allows for the direct observation of mass-resolved 3-D ion velocity distribution functions at many different altitudes and solar zenith angles. These observations mean that the evolution of the ion distribution function can be studied directly: experimenters can observe where, when, and under what conditions ion energization occurs, as well as where, when, and under what conditions ion escape can occur.

This introduction has been intended to motivate the use of electrostatic analyzers combined with TOF analyzers for the study of planetary ionospheres. While these instruments are challenging to construct and calibrate, the immense scientific return available makes them worth the trouble. STATIC data have been used to characterize ion escape with great success by the MAVEN team [8, 21, 56, 59, 14, 48, 52, 90, 75]; however, less work has been done towards understanding the physics controlling the beginning of cold ion outflow, in which cold planetary plasma is somehow accelerated to escape energy. Studying the initial stages of cold ion outflow is crucial, as the ionosphere near the exobase is likely to be a significant source of escaping ions. The remainder of this work will begin to address this gap in the study of ion escape at Mars.

One major reason for the existence of this gap is that data analysis in the initial acceleration region, between 200 km and 1000 km, is experimentally challenging. Spacecraft typically travel supersonically with respect to the cold gas and plasma in this region, so that ions are focused into a narrow beam that spans only a few measurement bins. Thus, the instrument response function must be well-characterized and the measurements corrected in order for the data to be interpreted accurately. Many details of the STATIC instrument response will be discussed in Chapter 2, which also describes the basic principles behind electrostatic analyzers and their use in space-based experiments. Chapter 2 includes a description of

work I led designing data products for the upcoming Escape and Plasma Acceleration and Dynamics Explorers (ESCAPADE) mission to Mars. The focus of Chapter 3 is a project I led helping to validate methods of measuring ion temperature with STATIC, including more details of the instrument response. Chapter 4 presents the results of applying those methods to over 10,000 MAVEN orbits, as well as a project I led developing an algorithm to identify the presence of suprathermal ions in STATIC data. A more detailed summary of the work in this document is provided in Chapter 5.

Chapter 2

Measuring major ion distribution functions with electrostatic analyzers

2.1 Introduction

This chapter is intended to serve both as an introduction to electrostatic analyzers (ESAs) for data analysts, as well as an in-depth reference for instrumentalists on certain topics such as background subtraction. We will discuss the measurement of major ion distribution functions with the Mars Atmosphere and Volatile EvolutioN SupraThermal And Thermal Ion Composition (MAVEN-STATIC) instrument [70], starting from how ions are steered into the instrument to generate counts. The basic principles discussed here can be applied to any ESA, though some caveats specific to STATIC will be discussed in detail. For a limited discussion of techniques to measure minor ion distribution functions with STATIC, interested readers are directed to [75].

2.2 Operating Principles of Electrostatic Analyzers

The cylindrical ESA was first described in 1929 [50] and the spherical design in 1938 [77]. One of the first applications of ESAs in space physics was the experimental confirmation of the existence of the continuous solar wind by Mariner 2 [72]. Since then, ESAs have been sent all over the Solar System, from the Sun [92, 60] to Pluto [68] and the comet Rosetta [73]. In the most basic sense, ESAs are just carefully shaped metal plates with electrical potentials applied to them. As charged particles pass near the charged plates, their paths bend towards or away from the surface, with the amount and direction of bending depending on the relative charges. Applying just the right potential to the surfaces allows particles of interest to be directed to a detector. Though the basic operational principle is simple, proper calibration and operation of ESAs is quite complex, especially for space-based experiments. The immense scientific return available from these instruments means that careful ground and in-flight calibration are incredibly important.

The Spherical Electrostatic Analyzer

The operating principle of the top hat spherical ESA is illustrated in Figure 2.1. The charged particle enters from the aperture at the top and experiences an electric field which is a function of the potential difference across the hemispheres, $\frac{dV}{dr}$. The electric field is directed radially and attracts the particle towards the inner hemisphere (or repels it from the outer). Since the electric field can only deflect the particle by a finite amount as it traverses the analyzer, only particles traveling at certain speeds reach the detector at the end of the analyzer. Particles with higher or lower speeds are outside the "energy passband" and impact the outer or inner hemisphere rather than reaching the detector. The potential difference across the hemispheres is varied in time, "sweeping" the energy passband in order to sample the full distribution of ambient plasma. To derive an expression for the energy of the particles in the passband, we will consider particles entering normal to the aperture and traveling on spherical trajectories for simplicity. In reality, particles traveling at different acceptance angles and along non-circular trajectories mean that the real energy passband is a function of both angle and energy. Including these caveats makes the calculation complicated enough that simulations and ground calibrations are typically used to determine the true energy and angular dependence of the passband. The expression we will derive below should be considered a back-of-the-envelope estimate.

Assuming a spherical trajectory of normal incidence, the centripetal force experienced by a particle of mass m, speed v, and energy E traveling at radius R is $mv^2/R = 2E/R$. The force is generated by the potential difference ΔV so that for a particle of charge q

$$\frac{2E}{R} = q\frac{dV}{dr}\bigg|_{r=R} \tag{2.1}$$

or

$$\frac{E}{q} = \frac{R}{2}\frac{dV}{dr}\bigg|_{r=R} \tag{2.2}$$

The plates have radii R_1 and R_2, a fixed hemisphere gap $\Delta R = R_2 - R_1$, and a tunable potential difference $\Delta V = V_2 - V_1$. The analyzer can be modeled as a spherical capacitor for the purpose of computing the charge on the inner hemisphere, which enables the use of Gauss' law to calculate the electric field $-\frac{dV}{dr}$. The charge on the inner hemisphere is $4\pi\epsilon_0\frac{\Delta V}{\Delta R}R_2R_1$. Now the electric field between the hemispheres is

$$-\frac{dV}{dr} = \frac{\Delta V}{\Delta R}\frac{R_2R_1}{r^2} \tag{2.3}$$

Combining equations 2.2 and 2.3 yields, for the energy of a particle on a spherical trajectory at radius R,

$$\frac{E}{q} = \frac{\Delta V}{\Delta R}\frac{R_2R_1}{2R} \tag{2.4}$$

The potential between the plates as a function of radius is given by

$$V(r) = \frac{\Delta V}{\Delta R}\frac{R_2R_1}{r} \tag{2.5}$$

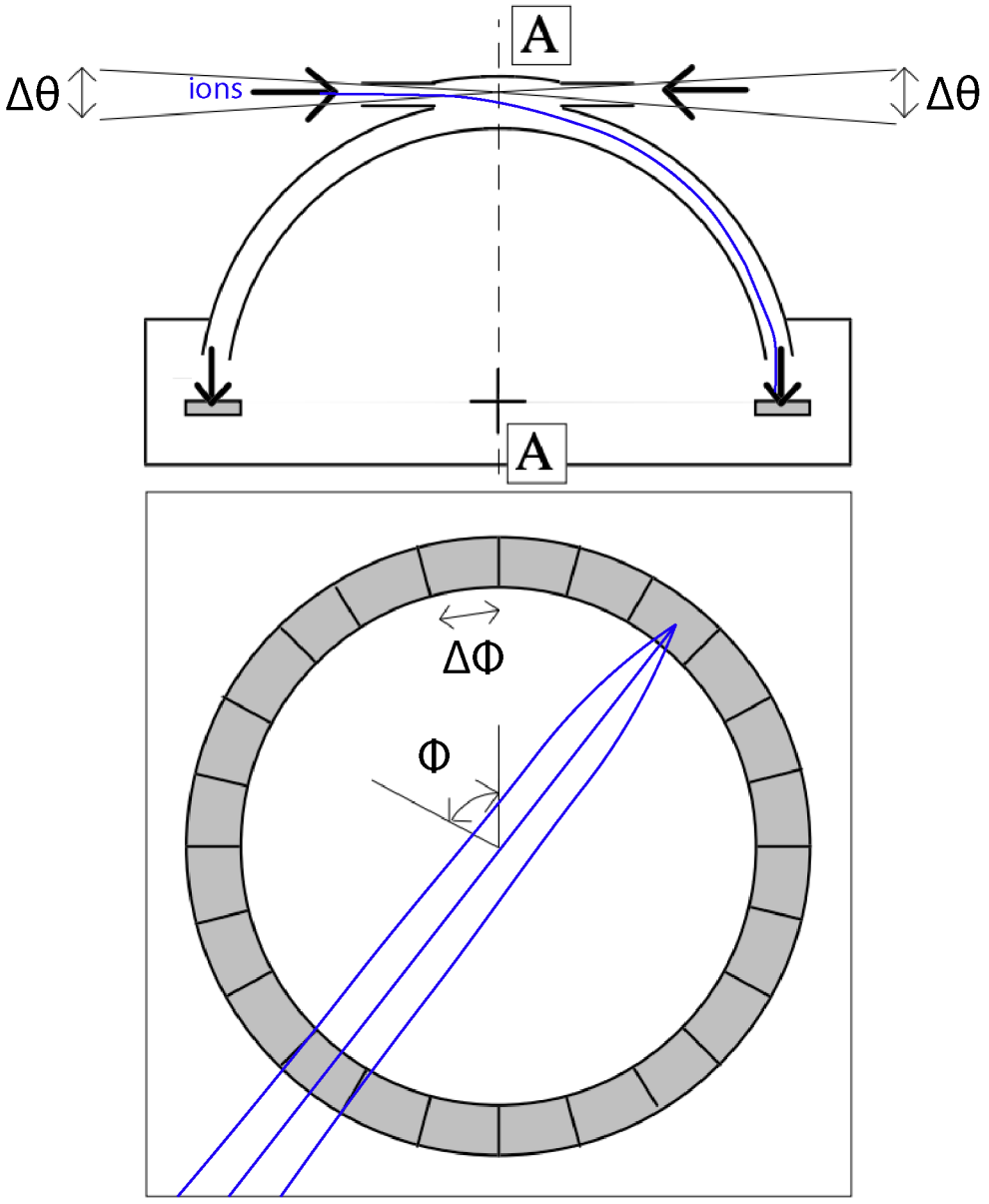

Figure 2.1: An illustration depicting a spherical top hat electrostatic analyzer, adapted from [74]. The axis of symmetry is indicated by the dashed line AA. This analyzer has a fan-shaped instantaneous FOV covering a solid angle $\Delta\theta$ by ϕ, with 24 azimuthal anodes of width $\Delta\phi$. Typical trajectories taken through the analyzer are illustrated in blue. The focusing of particles in the azimuthal direction is typically equally good regardless of the angle of entry.

The center of the energy passband is the energy of a particle on a spherical trajectory at the radius where the potential is halfway between the potential on either plate. We can solve for this radius R_V using equation 2.5. We find

$$R_V = \frac{2R_1R_2}{R_1 + R_2} = \frac{R_1R_2}{R_c} \tag{2.6}$$

where R_c is the center radius of the analyzer. Evaluating equation 2.4 at R_V yields the center energy of the passband E_c:

$$\frac{E_c}{q} = \frac{R_c}{\Delta R}\frac{\Delta V}{2} \tag{2.7}$$

Since the hemisphere gap is narrow compared to the hemispheres, equation 2.7 shows that spherical ESAs allow for measuring particles at higher energy-per-charge than the potential difference across the hemispheres. The ratio between the center energy and the potential difference is known as the analyzer constant, k, and typically ranges from 5–10. (Sometimes a different definition of analyzer constant is used, k=$R_c/\Delta R$.)

The edges of the energy passband ΔE can be assumed to be the same as the energy of a particle on a spherical trajectory adjacent to a hemisphere [74]. Evaluating 2.4 at $R_{1,2}$ therefore yields the energy at the edges of the passband, $E_{1,2}$:

$$\frac{E_{1,2}}{q} = \frac{R_{2,1}}{\Delta R}\frac{\Delta V}{2} \tag{2.8}$$

The width of the passband is given by the difference E_1 – E_2:

$$\frac{\Delta E}{q} = \frac{\Delta V}{2} \tag{2.9}$$

An important property of ESAs is that for spherical trajectories, the ratio $\Delta E/E$ is a constant, $\frac{1}{2k}$.

In real analyzers, non-circular trajectories cause the energy response to be slightly asymmetrical. More particles with energies higher than the center energy are able to navigate the analyzer if they enter near the inner hemisphere, while more particles with energies less than the center energy can navigate the analyzer near the outer hemisphere. The reader is referred to [77] and Chapter 5 of [74] for further discussion of the effects of non-circular trajectories.

Regardless of the angle of entry or if the trajectory was spherical, most particles are traveling in a narrow beam upon exiting the spherical ESA. This focusing effect is highly useful for experimentalists, as it allows for the placement of additional detectors, such as time-of-flight velocity analyzers, at the ESA exit. The focusing also enables highly accurate measurements of the position where the particle impacts the detector.

A significant advance in ESA design was made in 1982 with the invention of the top hat analyzer by Chuck Carlson [9]. The top hat design, which raises a "cap" portion of the outer hemisphere, allows particles to enter the analyzer from a fan-shaped field-of-view that

covers 360° in one plane, rather than particles entering from a small aperture at one end of the hemispheres. Top hat ESAs are typically operated on spinning spacecraft in order to achieve a field-of-view wider than only a few degrees in the plane perpendicular to the 360° coverage plane. Energy sweeps must be timed to the spin period. On a three-axis-stabilized spacecraft, the instrument itself is rotated using a scan platform in order to increase the coverage, resulting in time resolutions on the order of minutes. This design was used for the ASPERA-3 instrument onboard Mars Express [5]. Without the invention of the top hat analyzer, none of the work described in this thesis would be possible.

In addition to the top hat, electrostatic deflectors have often been used to increase the ESA fields-of-view. Deflectors can be operated at either polarity to either "push" or "pull" charged particles towards the aperture. By sweeping through different electric potentials on deflectors on either side of the entrance aperture, particles from a large portion of phase space can be sampled. Electrostatic deflectors enable the use of high time resolution ESAs on three-axis-stabilized spacecraft. Positively charged deflectors are appropriate for most applications, since negatively charged deflectors cannot be operated in sunlight due to the production of photoelectrons.

An Introduction to Microchannel Plates

Thus far we have discussed the optics of the spherical ESA, but the detector used to count particles that navigate the optics is equally important. Detectors such as channel electron multipliers and microchannel plates (MCPs) are commonly used to detect charge pulses associated with impacts by charged particles. The reader is directed to [94] for an extensive discussion of MCP operating principles. We will briefly explain the function of an MCP here.

Because the electrical impulse from a single particle impact is so small, the MCP relies on turning a single charged particle into cascades of electrons that create a charge pulse large enough to be measurable by a preamplifier (Figure 2.2). The "microchannels" are long tubes, closely spaced together within a conducting plate. The tubes are cut at an angle to the surface of the MCP, the "bias angle," so that they run diagonally through the plate. An electrical potential difference is imposed across the tubes, attracting charged particles towards one end. As a particle travels down the tube and bounces off the sides, it is accelerated past the impact ionization energy of the surfaces of the tubes. With each collision with the walls, more and more electrons are freed from the surface and attracted toward the end of the tube. The result is that the first cloud of secondary electrons creates exponentially more, resulting in typical gains exceeding $>10^3$ for one plate. Most MCPs are arranged in chevron pairs or Z-stacked triplets, with each plate having opposite bias angles to prevent feedback where electrons from the second or third MCP scatter up into the previous plate. Using two or three MCPs results in typical gains of $>10^{5-6}$.

MCPs must be operated such that the bias voltage is high enough that the charge pulse resulting from each particle looks the same regardless of the particle energy, but low enough that the microchannels do not saturate. If the MCP is exposed to high count rates, the

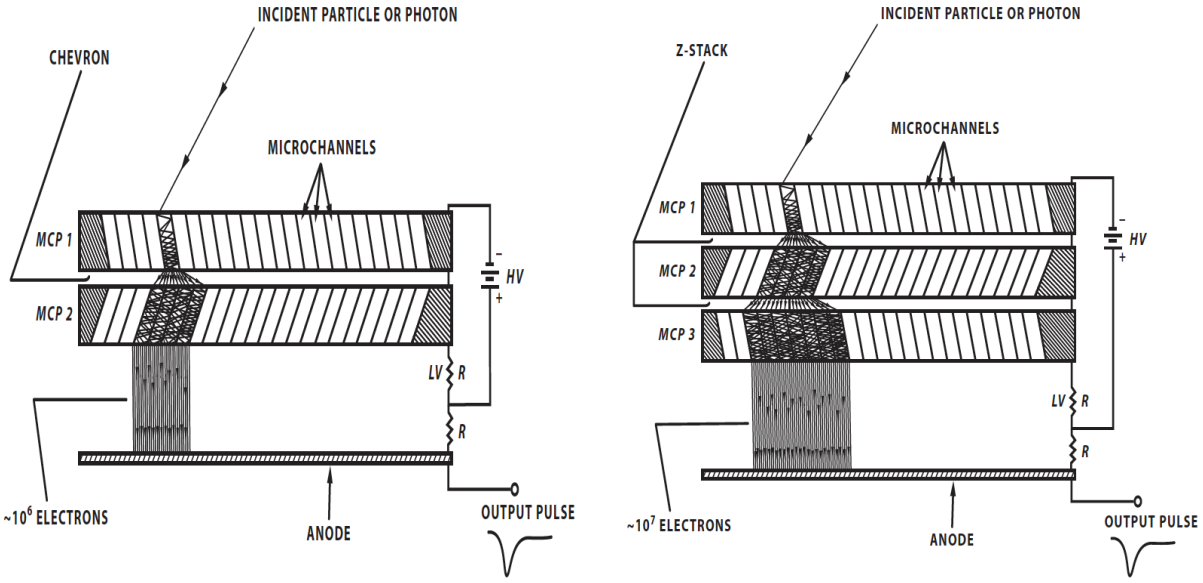

Figure 2.2: A cartoon of a microchannel plate (MCP) in a chevron (left) and Z-stack (right) orientation, reproduced from [94]. The incident particle creates a cascade of electrons, which creates exponentially more electrons at the second and third plates. The charge pulse generated by the electron cascade impacting a conducting anode is large enough to be measured.

charge pulses may begin to "droop" as the microchannels have insufficient time to recharge between events. This behavior makes dead-time corrections a nontrivial function of count rate history, so MCP droop should be avoided by controlling the count rate and the bias voltage. For space-based ESAs, the charge pulses generated by the MCPs are typically measured using preamplifiers attached to discrete anodes, which allow for high count rates and moderate angular resolution. For example, the STATIC instrument onboard MAVEN, with 16 discrete 22.5° anodes, can typically handle count rates up to 200 kHz without significant droop.

The STATIC Instrument and Time-of-Flight Velocity Analyzers

The STATIC instrument is a toroidal top hat ESA with an associated time-of-flight velocity analyzer (TOF) that was designed to separate Mars' main ionospheric and escaping species: H^+, O^+, O_2^+, and CO_2^+ (Figure 2.3). A toroidal ESA was chosen over a spherical design in order to shift the point where ions are focused to 90° from the entrance aperture; the geometry of a spherical ESA causes the focal point to occur at ∼75°, a less optimal position for the time-of-flight section. The top hat design in combination with electrostatic deflectors allows for 360° x 90° coverage (with the caveat that electrostatic deflectors are less effective

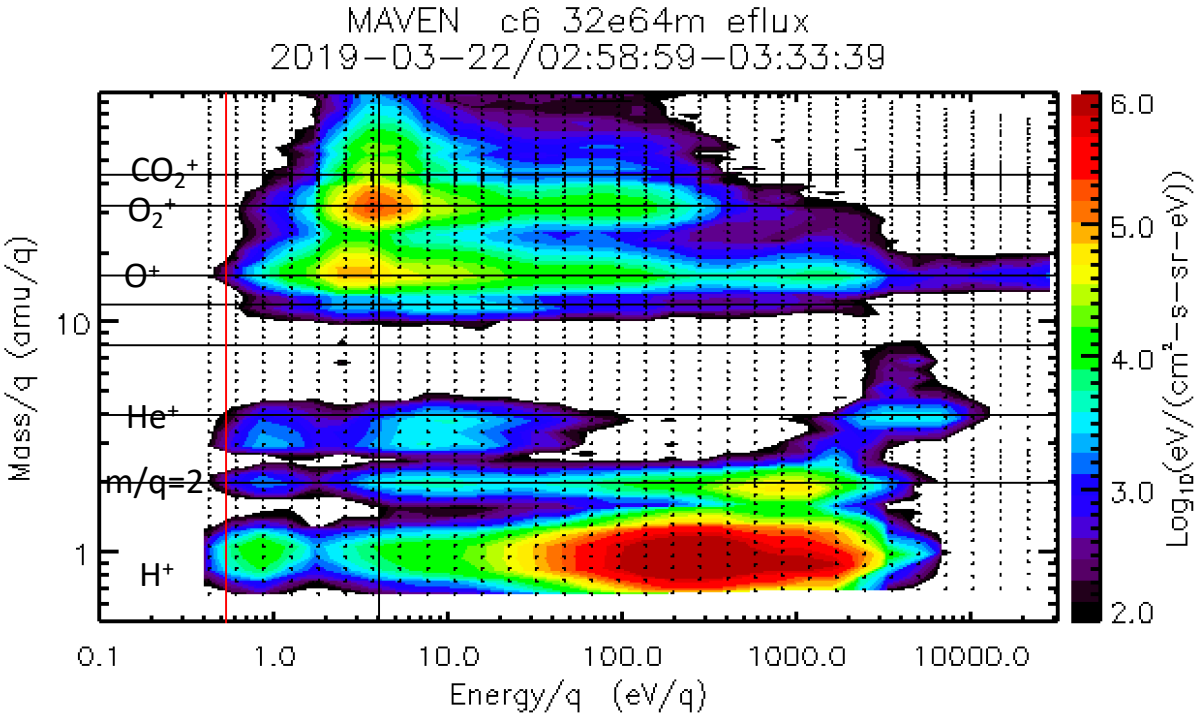

Figure 2.3: STATIC energy-mass spectrogram integrated over ∼34 minutes to illustrate mass separation. Black dots indicate sampled energy-mass bins. Horizontal black lines indicate commonly observed ion masses. The vertical red line indicates average spacecraft potential throughout the interval. The vertical black line indicates the average ram energy of O_2^+.

at energies above ∼4 keV, leading to a narrower FOV). 64 energy bands are sampled every 4 seconds.

Once the ion energy is known from the ESA, a time-of-flight velocity analyzer is used to separate ions by mass-to-charge ratio. An ion exiting the ESA is accelerated by -15 kV before striking a thin carbon foil, where a cloud of electrons is generated. Electrons in the cloud are accelerated by +12 kV and impact the MCP. The charge cloud generated by the MCP lands on an inner ring of anodes, creating a charge pulse that splits to travel towards each edge of the anode. The 16 anodes are connected into a chain by delay line chips, which introduce a 2 ns delay between anodes. The two halves of the split charge pulse travel in opposite directions around the circular chain of anodes; we will arbitrarily call the clockwise pulse A and the counterclockwise pulse B. Depending on which anode was impacted, either pulse A or B reaches the end of the chain first. (Without the delay line chips, the pulse would reach both ends nearly simultaneously.) The anodes at the end of the chain are not connected by a delay line chip; instead, they are connected to a time-to-amplitude conversion circuit. (The time-to-amplitude converter (TAC) technique is described in [94].) For the sake

of our discussion, we will assume pulse A reaches the end of the anode-delay line chain first, where it activates two constant current sources that begin to charge two capacitors. When pulse B arrives, it closes off one of these current sources, stopping one of the capacitors from charging, and activates a different constant current source to charge a third capacitor. The charge on the first capacitor can be read out to measure time elapsed. The difference in arrival time T at the end of the chain is used to determine which anode was struck by the charge cloud (TB-TA).

Meanwhile, two capacitors are still charging—one activated by pulse A, and one activated by B. The ion has sufficient energy to pass through the first thin foil due to the post-acceleration, so it keeps flying in a straight line and hits a second thin foil, where another cloud of electrons is generated. The ion has typically charge-exchanged to a neutral by this point, and a thick foil is placed between the second thin foil and the MCP in order to stop neutrals and residual ions from striking the MCP directly. The second cloud of electrons is also accelerated, this time to impact a different portion of the MCP. Below this portion of the MCP is an outer ring of anodes, and another charge pulse splits to travel around the outer anode-delay line chain, which has its own set of 2 ns delay line chips. We arbitrarily call the clockwise outer-ring pulse C and the counterclockwise outer-ring pulse D. When pulse C reaches the end of the delay line, it turns off the current source activated by pulse A, and turns on a different current source to begin charging a fourth capacitor. Now the time-of-flight can be calculated from (TC-TA). When the final charge pulse, D, arrives at the counterclockwise end of the stop delay line, it shuts off the last two current sources: the one activated by pulse B, and the one activated by C. Again, the difference in arrival time (TD-TC) is used to calculate which anode was struck, and the time-of-flight can be calculated from (TD-TB). Mass lookup tables (MLUTs), populated based on ground calibrations, are used to bin TOF measurements into different mass channels. In addition to redundancy, this delay line technique of calculating TOF provides the benefit of reducing background counts through coincidence verification, which will be discussed in Section 2.3. The technique also reduces the number of cables required to connect the sensor to the electronics. For a full description of the caveats associated with the STATIC TOF design, readers are directed to [70].

2.3 Converting from Counts to Physical Units: The Geometric Factor, Background Subtraction, and Spacecraft Potential

The discussion so far has been written from an instrument-focused perspective, using units of counts registered by a detector. To convert from the language of engineering to the language of science, units that relate to real-world quantities such as flux are desirable. Accurate conversion to physical units requires accurate background subtraction, extensive ground, in-flight, and cross-calibration to determine instrument constants and detector efficiencies, and

a method of correcting for spacecraft potential.

The Geometric Factor and Unit Conversion

The first step in converting from count rates to physical units is application of a constant of proportionality known as the geometric factor. For a top hat ESA such as STATIC, the number of counts, N, in an energy-solid angle bin is directly proportional to the energy flux measured by the instrument. The constant of proportionality is the geometric factor, which varies with energy and solid angle.

When combined with knowledge of the detector efficiency, the geometric factor can be used to convert counts to physical units. In essence, the instrument is tuned to sample a portion of phase space defined by look direction and the center of the ESA energy band. We will denote the energy width of each phase space bin by dE and the solid angle covered by each bin by $d\Omega$. Over the course of one integration, the detector measures the count rate (1/s) of particles through the aperture ($1/cm^2$) in the phase space bin defined by the center energy (eV), $d\Omega$ (1/sr), and dE (1/eV). By sweeping through different look directions and energy bands, the count rate in different phase space bins is measured. We define the geometric factor $g_{eff}(E,\Omega)$, including all efficiencies, from the relationship between the differential directional energy flux $\frac{d\tilde{J_E}}{dEd\Omega}$ and counts N during one integration t:

$$\frac{d\tilde{J_E}(E,\Omega)}{dEd\Omega} = \frac{N(E,\Omega)}{g_{eff}(E,\Omega)t}\hat{n} \tag{2.10}$$

where $\hat{n}$ is a vector normal to the entrance aperture. Differential directional energy flux has units of $eV/cm^2/s/sr/eV$, and the geometric factor has units of eV cm^2 sr/eV. To calculate the differential directional number flux of particles in $1/cm^2/s/sr/eV$, it is necessary to divide by the energy:

$$\frac{d\tilde{J}(E,\Omega)}{dEd\Omega} = \frac{1}{E}\frac{N(E,\Omega)}{g_{eff}(E,\Omega)t}\hat{n} \tag{2.11}$$

So far the physical units we have focused on have been differential and directional. They can be integrated over the energy range and field-of-view of the instrument in order to calculate the total energy or number flux measured by the instrument. The last differential directional unit we will discuss is phase space density, or velocity distribution function, from which physical quantities such as density, temperature, and bulk plasma velocity can be calculated by taking moments or from model fitting. Phase space density typically has units of $cm^{-3}(km/s)^{-3}$, so the process of converting units is more involved than going from 2.10 to 2.11. The derivation is easiest to follow if considered as unit conversion in combination with a change of variables, since phase space density is a function of velocity rather than energy.

$d\vec{J}$ has units of $1/cm^2/s$ and is related to the phase space density by:

$$d\tilde{J} = \tilde{v}f(\tilde{v})d\tilde{v} = \frac{dE}{E}\frac{N(E,\Omega)}{g_{eff}(E,\Omega)t}d\Omega\hat{n} \tag{2.12}$$

Our aim is to obtain an expression for $f(\tilde{\mathrm{v}})$. The next step is to expand the volume element in spherical coordinates. Canceling the solid angle dependence on both sides leaves:

$$\tilde{\mathrm{v}} f(\tilde{\mathrm{v}}) \mathrm{v}^2 \mathrm{dv} = \frac{\mathrm{dE}}{\mathrm{E}} \frac{\mathrm{N(E,\Omega)}}{\mathrm{g}_{eff}(\mathrm{E},\Omega)\mathrm{t}} \hat{n} \tag{2.13}$$

$\frac{\mathrm{dE}}{\mathrm{E}}$ is constant for ESAs, so it is useful to write dv in terms of v^2. Noting that $\mathrm{v\ dv} = \mathrm{d}(\frac{\mathrm{v}^2}{2})$, we can write:

$$f(\tilde{\mathrm{v}}) \mathrm{v}^2 \mathrm{d}(\frac{\mathrm{v}^2}{2}) \hat{v} = \frac{\mathrm{dE}}{\mathrm{E}} \frac{\mathrm{N(E,\Omega)}}{\mathrm{g}_{eff}(\mathrm{E},\Omega)\mathrm{t}} \hat{n} \tag{2.14}$$

Because $\hat{v}$ must be equal to $\hat{n}$, it is now clear that each portion of the distribution function is sampled when the look direction is pointed towards that part of phase space. Since the left hand side of 2.14 only contains even powers of velocity, it is now directly proportional to the energy, $\frac{1}{2}\mathrm{mv}^2$:

$$f(\tilde{\mathrm{v}}) \mathrm{v}^2 \mathrm{d}(\frac{\mathrm{v}^2}{2}) = f(\tilde{\mathrm{v}}) (\frac{2\mathrm{E}}{\mathrm{m}}) \mathrm{d}\frac{\mathrm{E}}{\mathrm{m}} \tag{2.15}$$

With this substitution, we can now solve for $f(\tilde{\mathrm{v}}) = f(\mathrm{E},\Omega)$ in terms of the experimental quantities that were measured as a function of energy and solid angle:

$$f(\mathrm{E},\Omega) = \frac{\mathrm{m}^2}{2\mathrm{E}^2} \frac{\mathrm{N(E,\Omega)}}{\mathrm{g}_{eff}(\mathrm{E},\Omega)\mathrm{t}} \tag{2.16}$$

As a note, ion masses are often calculated in $\mathrm{eV/(km/s)^2}$ for the purposes of this calculation. In that case, the final step is converting 1 power of km^{-1} into 1 power of cm^{-1}, picking up a factor of 10^5 on the way.

We have now defined the geometric factor in terms of various physical quantities. The importance of understanding an instrument's geometric factor and its variations throughout the parameter space cannot be overstated. Typically, an instrument's geometric factor is calculated using optics simulations. Ground calibrations are then used to ensure proper construction of the sensor. In an ideal, perfectly symmetric analyzer, g_{eff} does not vary with rotation angle about the symmetry axis; in reality, g_{eff} typically varies in different look directions due to small deformations or misalignment of the plates and variations in detector efficiency. In order to ensure accurate results, experimenters should take care to quantify the variation of $\mathrm{g}_{eff}(\mathrm{E},\Omega)$ during ground calibrations. MCP efficiency can change over time, so periodic in-flight calibrations are also necessary. For a derivation of the value of the geometric factor, the reader is directed to [43]. Descriptions of ground calibration procedures may be found in [94, 70].

One caveat we have glossed over so far is detector deadtime, which must be corrected before conversion to physical units described by Equations 2.10–2.16. The instrument electronics can only process one event at a time, effectively shortening the accumulation time over which counts are measured. Many components of the electronics can introduce dead time, but typically one or two components have the largest effect. Some systems, termed

"nonparalyzable," are not affected by the impact of additional particles during the time it takes to process one event. In contrast, "paralyzable" systems restart the clock for each event, meaning that processing time is lengthened by additional events and instrument performance can be severely degraded at high count rates. Non-paralyzable detectors can be used reliably over a range of count rates over 10 times wider than the range of rates over which paralyzable detectors are reliables [74]. Methods for measuring dead time effects and examples of dead time corrections are discussed in [74, 94].

Background Subtraction

Perfect knowledge of the geometric factor does not help experimenters if the signals of interest are lost in instrumental noise. Background subtraction requires understanding of where background counts are generated inside the instrument, as well as an understanding of the environment in which the sensor will be used in order to eliminate counts that are "real," but uninteresting for science (e.g. ions sputtered off the spacecraft).

The STATIC instrument is designed to minimize many sources of background counts, and further processing is done on the ground to remove background that does make it into the data. Many sources of background are eliminated from STATIC data by requiring coincidence in the time-of-flight circuit – that is, requiring start and stop signals to occur in the same anode within a set period of time. These sources of eliminated background include (B1) photons or energetic particles reaching the detector by penetrating the walls of the instrument, (B2) radioactive decay in the MCP, (B3) field emission in the TOF, (B4) "cross-talk" events where secondary electrons spill over into adjacent anodes, and (B5) events lacking a "start" or "stop" pulse due to start and stop efficiencies that are less than 1 (typically 0.7 and 0.4, respectively). Scattered electrons inside the TOF can cause (B6) nearly simultaneous start and stop pulses, which can be eliminated by requiring a minimum duration for the time of flight. (These TOF=0 events can show up in the data due to an unfortunate choice of capacitor that does not entirely discharge between events. These counts are removed from the data using an empirical correction.) Other sources of background counts were mitigated through careful design choices, such as the placement of the thick foil between the stop foil and the MCP. The thick foil suppresses (B7) ghost peaks caused by a delayed stop signal, which would be produced from neutrals and negative ions striking the MCP in events where a stop signal is not generated at the stop foil. The different sources of ghost peaks, including ghost peaks caused by positive ions striking the MCP, are described in detail by [70]. Finally, the internal hemispheres were serrated and coated with a blacking called Ebonol-C to reduce (B8) internal particle forward scattering and photon scattering. The introduction of this coating caused other problems, which will be discussed in Section 2.5.

Not all background counts can be suppressed through coincidence logic and careful design choices. In total, 17 types of background signals have been identified in STATIC, which are described in Table 2.1. The 8 sources that were just described do not contribute significantly to the data and are not further detailed here. (In addition to the exception of background

6 noted above, another exception is background 3, which can occasionally produce a background count if field emission produces an electron near the Start foil. The electron can then impact the analyzer walls and produce an ion that gets post-accelerated into the TOF. Additionally, single-pulse events can contribute to coincidence background at high event rates, as will be discussed below.) Some of the remaining sources of background, which do appear in the science data, result from nonlinear behavior of a capacitor in the TOF circuit, which was discovered during ground calibration and is described by [70].

Source of Background Counts	**Description of Signal**	**Mitigation Strategy**
1. Penetrating radiation		Coincidence logic
2. Radioactive decay in MCP		Coincidence logic
3. Field emission in TOF		Coincidence logic
4. Cross-talk		Coincidence logic
5. Single-pulse events		Coincidence logic
6. TOF=0 events from scattered electrons		Require minimum TOF
7. Ghost peaks caused by delayed stop by negative ion/neutral		Place thick foil between stop foil and MCP
8. Internal scattering of particles/photons		Serrated inner hemisphere and blackened hemispheres
9. Ions sputtered off spacecraft	Low energy, low flux, composed of fragments of adsorbed gases	Mount and point instrument away from spacecraft
10. Forward-scattered protons	Low-energy protons in solar wind	Angle & scallop surfaces away from aperture
11. Different particles trigger start and stop (coincident events)	$\propto$ rate^2, nearly flat in mass dimension	Use attenuators to control count rate; empirical correction
12. Energy straggling through carbon foils	High-mass tail $\propto$ rate	Use thin foils and post-acceleration; empirical correction
13. Valid or crosstalk event after StartNoStop event due to non-linear TOF capacitor	Mass channel contamination at high event rates, $\propto$ rate^2	Ensure capacitors discharge completely between events; empirical correction
14. H^+ ions from H_2^+ molecule emerge from stop foil, reflect, and produced delayed stop signal	Ghost peak at known TOF $\propto$ rate	Place thick foil between stop foil and MCP; emprical correction
15. Molecular ion fragments that produce a delayed start pulse	Low-mass shoulder $\propto$ rate	Empirical correction
16. Ions that bounce off grids and posts	Low energy, comes from known direction	Empirical correction
17. Internally produced ions from start foil electrons accelerated back into the ESA	Composed of atomic fragments of adsorbed gases	Empirical correction

Table 2.1: Types of background that may affect STATIC data. The first 8 sources typically do not register as counts, except at high count rates.

Some of these sources of background will likely never be removed from STATIC data in an automated fashion. Fluxes of ions sputtered off the spacecraft (B9) are so small that

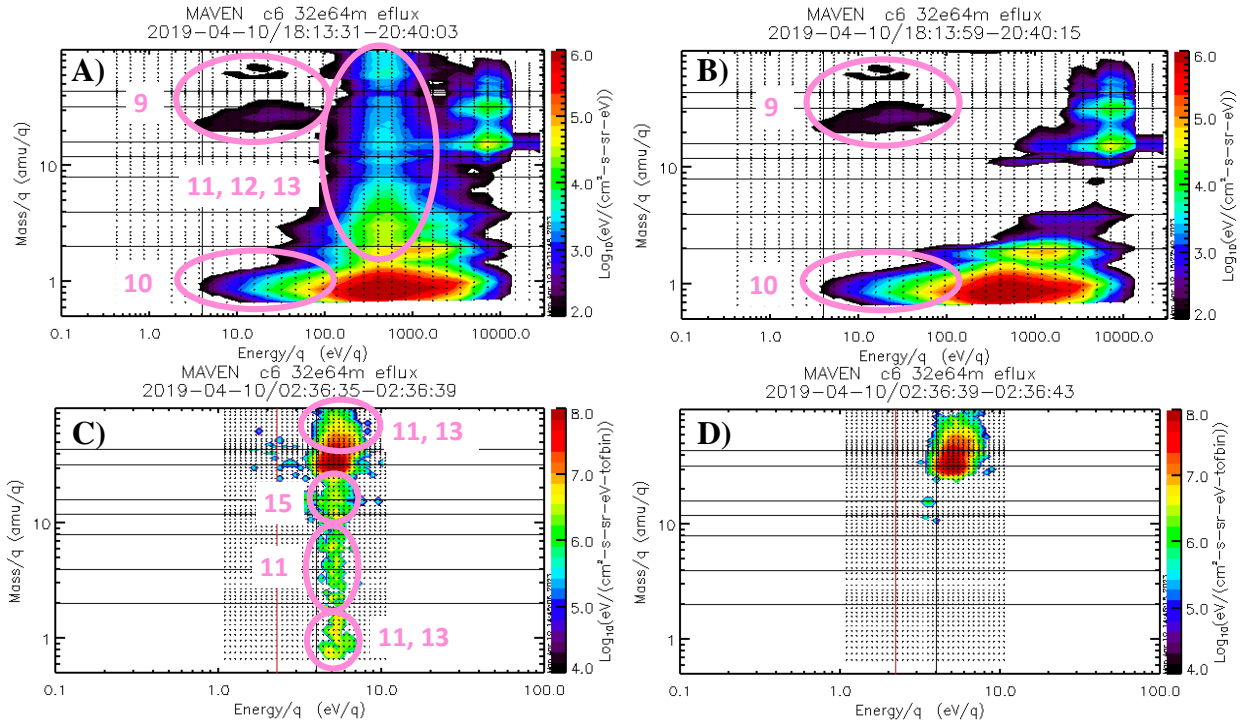

Figure 2.4: Energy-mass spectrograms from in-flight data. Black dots indicate sampled bins. Horizontal black lines indicate masses of common ions. Vertical black lines indicate the expected ram energy of O_2^+, and vertical red lines indicate spacecraft potential. Pink circles indicate different background sources. Panel A: Integrated distribution showing the solar wind and planetary heavy ions. Panel B: Panel A after background subtraction. Panel C: Single measurement showing planetary heavy ions. Panel D: Panel C after background subtraction.

they can't be identified in individual measurements and require averaging over a long periods for identification, therefore their removal is not attempted and can generally be ignored in comparison to scientifically interesting distributions such as pickup ions. Background 9 is typically observed at low energies (<40 eV) and is composed of fragments of CO_2 adsorbed onto the surface of the spacecraft (i.e. CO^+ and CO_2^{++}.). An example of background 9 is visible in Figure 2.4A as the low-energy and low-flux signature at mass 28 (likely CO^+). Background 10 consists of protons that forward-scattered off internal surfaces in the ESA or inelastically scattered off aperture posts, grids or the spacecraft during the energy sweep. Their angular and energy distributions are complex enough to discourage an empirical description, particularly because they can be easily ignored to make accurate calculations of solar wind parameters by imposing limits on the energies and angles included in the calculation. An example of Background 10 is shown in Figure 2.4A.

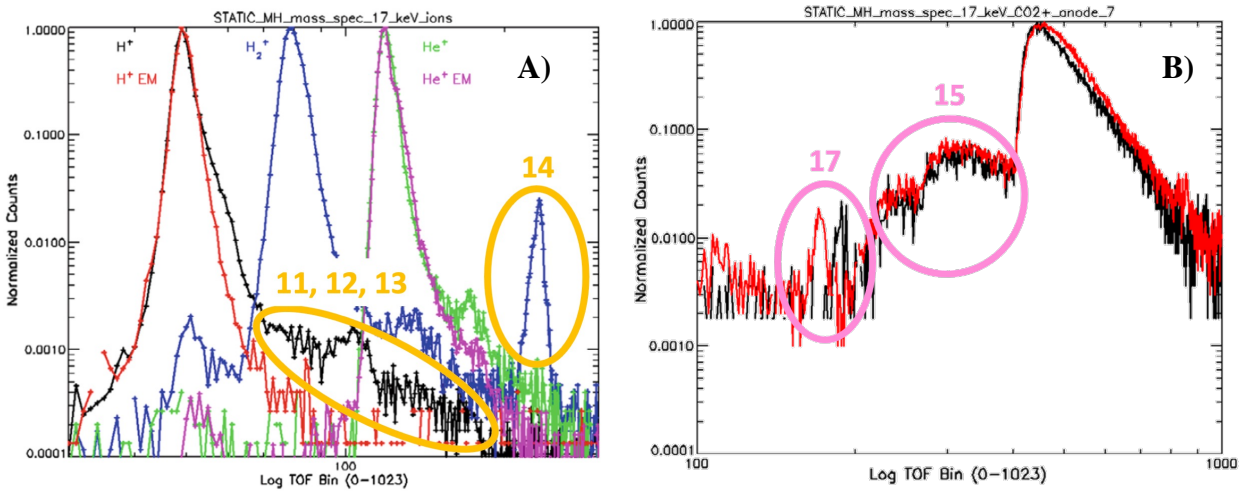

Figure 2.5: Examples of background sources in STATIC, circled in orange/pink. See text for details. Panel A: Mass spectrogram showing H^+, H_2^+, and He^+ for both the engineering and flight models, reproduced from [70]. Panel B: Mass spectrogram for CO_2^+, reproduced from [70]. The black (red) line is 5 (2) keV ions with a 12 (15) keV post-acceleration.

Automated corrections have been developed to remove counts caused by (B11) coincident events, (B12) energy straggling, (B13) the incorrect TOF measurements caused by hysteresis resulting from a nonlinearity in the RC discharge of a TOF capacitor, (B14) fragmented H^+ ions from an H_2^+ molecule reflecting before striking the thick foil and producing a ghost peak, (B15) fragments of a molecular ion after the start foil striking an internal TOF surface and producing a delayed secondary electron start event, (B16) ions scattered off the grids/posts when the mechanical attenuator is closed, and (B17) ions produced internally by backscattered electrons. Figure 2.3 shows an example of data for which background subtraction has been performed successfully; the success of the developed background subtraction algorithms is most obvious because of the lack of vertical bands contaminating the mass channels located at the same energies as the proton and O_2^+ peaks. The remainder of this section will describe these sources of background in greater detail.

Background 11 is primarily a problem for high count rates such as in the solar wind beam, when multiple particles are inside the TOF at the same time. For some fraction of events, different particles produce the start and stop signals, or one signal is produced by penetrating radiation or a noise count in the MCP. Alternatively, a StartNoStop (i.e. an event that produces a start pulse but not a stop pulse within the finite TOF window) closely followed by a Stop can produce a count that appears to be real. Background 11 is colocated with the main beam in energy and angle. The signal is roughly constant in the mass dimension, with a second-order falloff towards higher masses. This second-order falloff is because a single-pulse Stop is equally likely to occur at any point in the finite-length TOF

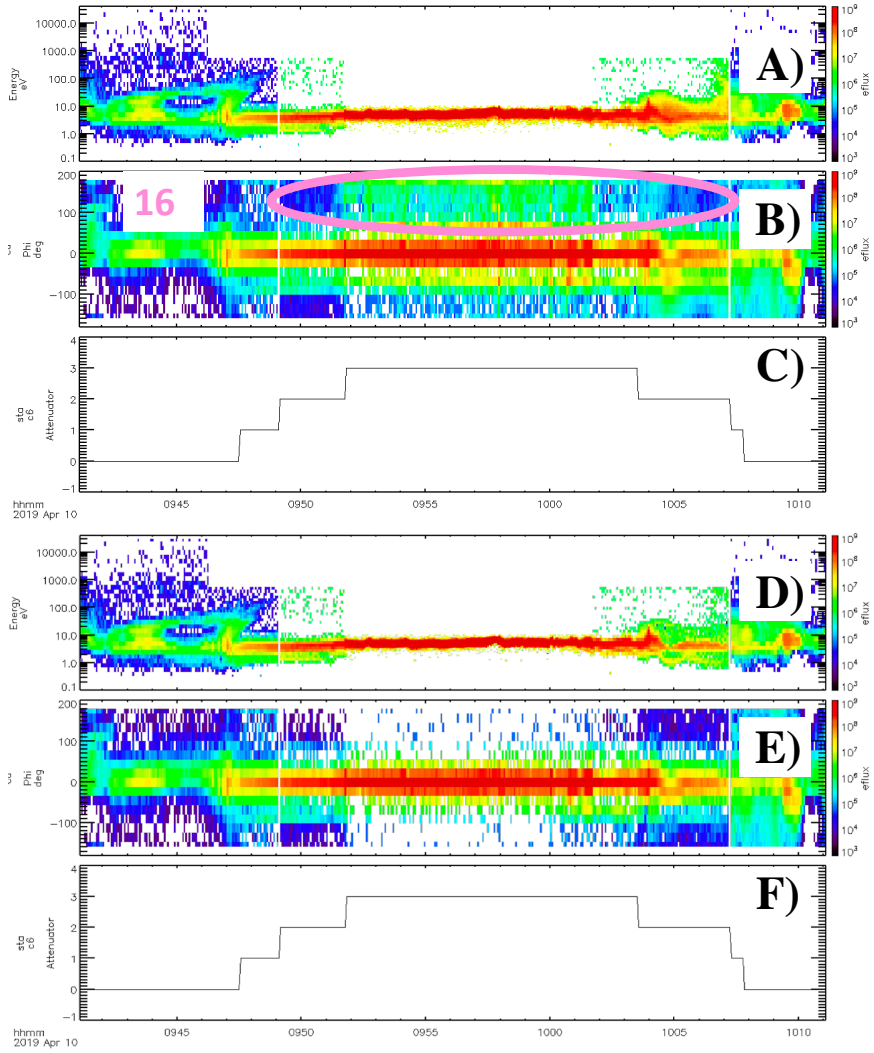

Figure 2.6: STATIC data from a single periapsis pass. Background counts reflected off the grids and posts when the mechanical attenuator is closed are indicated by the pink circle. Panel A,D: Energy spectrogram before and after subtraction. Panel B,E: Anode distribution before and after subtraction. Panel C,F: Attenuator state. The mechanical attenuator is engaged in states 2 and 3.

measurement window, but if two Stops occur shortly after a StartNoStop, only the first Stop creates a background count.

One consequence of the use of carbon foils to generate start and stop pulses for the TOF is the "energy straggling" which produces Background 12. Ions lose different amounts of energy upon colliding with the start foil, resulting in a slower-than-expected TOF which manifests as a high-mass tail. This effect is most obvious for protons and is minimized by

using the thinnest possible carbon foils, with the tradeoff that thinner foils are more difficult to mount inside the instrument. The high mass tail is removed for protons and alphas, but not for heavier ions. Instead, heavy ions are allowed to have broader mass peaks and fitting algorithms are used to improve mass separation.

Background 13 is a nonlinear version of background 12 which is only noticeable at high rates. This background source is unique to STATIC due to an unfortunate choice of capacitor in the TOF circuit. The TOF circuit uses a constant current source to charge a capacitor, with the start and stop pulses gating the current, and an analog-to-digital converter to measure the capacitor voltage. After an event, the capacitor is discharged to ready it for the next event. At high event rates, the capacitor discharge is not complete, leaving some residual charge, due to an unfortunate nonlinearity in that capacitor. If a second event occurs shortly after a heavy ion or StartNoStop event, a significant amount of charge can remain in the capacitor which can result in an incorrect TOF on the following event. The nonlinear behavior of the TOF circuit is modeled and the high mass tail is removed from ions with mass-to-charge ratios of 1 or 2. Backgrounds 11 (coincidence), 12 (straggling), and 13 (nonlinear coincidence) produce overlapping signatures, meaning that characterizing them is difficult. Energy straggling can be characterized during times of low count rates, and the coincidence backgrounds at high count rates. Background 11 is directly proportional to the square of the count rate. Remaining background counts are assumed to be due to background 13 so that an empirical formula can be used to correct for the nonlinearity in the TOF capacitor. Backgrounds 12 and 13 are anode-dependent due to differences in the carbon foils and the nonlinearities in the TOF electronics. It is possible to characterize each anode independently because STATIC is pointed many different ways during the high altitude segment of different orbits, so the solar wind beam can be observed in any anode. Backgrounds 11, 12, and 13 are visible on the black proton spectrum in Figure 2.5A, as well as in Figure 2.4.

The 14th type of background that could affect STATIC is a ghost peak produced by positive ions at a known TOF. The ghost peak, visible on the blue H_2^+ line in Figure 2.5A, is caused by ions or fragments failing to produce a normal stop signal. $\sim$10% of dissociated H atoms from H_2^+ fragmentation emerge from the stop foil as positive ions and lack enough energy to reach the thick foil. Instead, they reflect to strike the stop foil a second time and produce a delayed stop pulse, causing a ghost peak at a particular TOF. The ghost peak is only visible for H_2^+ because energy straggling overpowers the ghost peak for heavier molecular ions. The ghost peak is useful for differentiating H_2^+ from other ions with mass-to-charge ratios of 2, such as He^{++}.

Ion fragmentation resulting in low-mass "shoulders" on molecular ion distributions was observed during ground calibration of STATIC (Figures 33 and 34 of [70], and Figure 2.5B in this work). This 15th background source is believed to be produced when molecular ions impact the start foil or a nearby surface and dissociate into two fragments. Neither fragment produces a normal start pulse—instead, one fragment impacts a nearby surface at a high angle of incidence, producing secondary electrons resulting in a delayed start pulse, while the other fragment produces a normal stop pulse. This background is known to be

produced inside the TOF because the signal does not shift with TOF voltage, only with the incoming energy of the molecular ion. A formula was empirically determined to correct this background for mass bins > 10 amu.

Background 16 is a straightforward correction in comparison to others. These ions, which scatter off the grids and posts to enter the analyzer from the anti-ram direction, typically comprise about 3% of the density, but their angular distributions are complex enough to discourage an empirical description. This background source is only removed for distributions measured below 500 km when the mechanical attenuator is closed, where the majority of ions enter the instrument in the ram anode (7). The spacecraft moves supersonically with respect to heavy ions in this altitude regime, so that any low-energy heavy ions that enter the analyzer outside anodes 5-9 can be assumed to have bounced back into the instrument after hitting a grid or post. This is a problem because the mechanical attenuator reduces counts from the ram direction by a factor of 100, but does not cover the anti-ram direction, meaning that a small number of reflected ions can create a signal comparable to the attenuated ram beam. An example of such a signal is shown in Figure 2.6.

Background 17 occurs when secondary electrons produced on the front of the Start foil are accelerated back into the ESA. Two grounded grids are included at the analyzer exit to prevent the strong electric fields from the TOF post-acceleration from leaking into the ESA. Some fraction of backscattered electrons pass through the grids into the ESA, where they can produce ions from gas adsorbed onto the walls. These ions are produced at low energies, so they typically impact the inner hemisphere of the ESA. However, some small fraction of these ions may exit the ESA, where they are then accelerated into the TOF to create a background count. Most of background 17 is actually produced by backscattered electrons impacting the exit grids and producing ions from gas adsorbed onto the grids, which are then accelerated into the TOF. Like background 9, these ions are produced from fragments of adsorbed gases, this time from the walls of the instrument rather than the spacecraft exterior. Background 17 is known to be produced inside the TOF from backscattered electrons because the peak shifts with the post-acceleration voltage, which can be seen in Figure 2.5B.

Spacecraft Potential

Any object immersed in a space plasma will acquire an electric potential such that the net current flowing from the plasma to the object is zero. Ion currents drive the potential positive, while electron currents drive the potential negative. For a spacecraft comprised of both conducting and insulating parts, different parts of the spacecraft will acquire different potentials to achieve zero net current locally. Science instruments are grounded to the conducting part of the spacecraft, so the potential of the conducting parts of the spacecraft relative to the ambient plasma many Debye lengths away is referred to as the "spacecraft potential."

Correcting for the electric potential and motion of the spacecraft is often desirable in order to analyze the low energy distribution function in the reference frame of the plasma. Note that correction is only important if the spacecraft potential is comparable to the ion

energy. If the spacecraft potential is only a few Volts, then keV ions are hardly affected. On the other hand, large spacecraft potentials can preclude the measurement of low-energy particles or reduce the energy resolution by accelerating particles into higher energy (i.e. wider) bins. In this section we will focus on correcting for spacecraft potential, which can be estimated using a variety of different methods.

The measured energy E_{meas} per charge (q) of charged particles of with respect to the spacecraft is related to the spacecraft potential V by:

$$E = q(V + E_{meas}/q) \tag{2.17}$$

where E is the energy in the plasma frame. A negatively charged spacecraft attracts positively charged ions, meaning they are observed at higher energies than if the spacecraft were uncharged. If the spacecraft potential changes slowly with respect to the sweep time, then each energy bin can simply be shifted by -qV to calculate the ion energy before its interaction with the spacecraft.

Spacecraft potentials are estimated from STATIC data using this principle. In the Martian ionosphere, MAVEN's spacecraft potential is typically near zero, or driven negative due to the imbalance of ion and electron currents to the spacecraft. This imbalance is caused by the fact that ions impact the spacecraft only as a narrow beam facing the ram direction, while the lighter, faster electrons impact the spacecraft from all directions. If the spacecraft is oriented without large conducting areas facing the ram flow, the spacecraft potential can be driven negative. The energy of the ions can be expanded into a directed bulk flow and a randomly oriented thermal component. The thermal component determines the width of the distribution function, while the bulk flow determines the center velocity of the distribution function. In the spacecraft frame, one component of the bulk flow is equal and opposite to the spacecraft velocity, and other components may be present, such as winds or drifts. Therefore the energy of the peak of the distribution function is:

$$E_{peak} = \frac{1}{2}m(\overrightarrow{v}_{wind} - \overrightarrow{v}_{sc})^2 - qV \tag{2.18}$$

The spacecraft velocity is typically well-known. If the winds and drifts are small compared to the spacecraft speed, then the spacecraft potential can be estimated using the peak energy of a distribution function. When MAVEN is below 180 km altitude, where it travels supersonically with respect to the dominant ion O_2^+, spacecraft potential is estimated from the peak energy of the O_2^+ distribution function. MAVEN's typical speed below 180 km is 4.2 km/s, or 2.9 eV for O_2^+. In this altitude regime, ion dynamics are controlled by the neutral atmosphere. While measurements of ion winds are not currently possible with STATIC, neutral winds at Mars are estimated to have speeds on the order of 200 m/s [81], which would correspond to an error of 0.007 V in spacecraft potential. Given that STATIC's dE/E is 16% [70], or 0.46 eV at 2.9 eV, the error is negligible and assuming zero wind is justified.

At altitudes above 300 km, where flows and drifts can be caused by electromagnetic forces, neglecting the drift speed is a bad assumption. In this altitude regime, distributions tend

to be broader, with ions observed at a wider spread of energies. If the spacecraft potential is negative, the minimum energy at which positive singly charged ions are observed is equal to the spacecraft potential. The lowest energy where protons are observed in STATIC data is used to estimate negative spacecraft potentials above 300 km. For altitudes between 180 and 300 km, the less negative of the two estimates is used. If the more negative value were used, then some energy bins with counts would be associated with negative energies, which is nonphysical.

MAVEN's spacecraft potential is typically negative in high density plasmas and in shadow. Positive potentials, which force positively charged ions to lower energies, should not be quantified by positive ion analyzers, although the shifted ram energy method may work as long as the potential is small enough that the peak can still be clearly resolved. It is more reliable to use electron analyzers to estimate positive spacecraft potentials. A sharp break in the electron energy spectrum will be observed at the positive spacecraft potential.

Because the distribution function is conserved along any trajectory in phase space (Liouville's theorem), the energy gained or lost by traversing spacecraft potential can simply be subtracted off once the spacecraft potential is known, assuming the spacecraft potential does not change during a measurement.

If the spacecraft potential does change during a measurement, the correction becomes significantly more difficult. Each accumulation bin should be corrected individually based on the average spacecraft potential during the accumulation, rather than assuming constant spacecraft potential throughout the energy sweep. Such a correction requires higher time cadence data from another instrument, such as a Langmuir probe. The procedure used to perform this correction for STATIC data, enabling significantly improved accuracy in ion densities and temperatures, is described by [32].

2.4 Managing Data Rates

The previous sections have been intended to demonstrate how instruments like STATIC produce data, as well as how the data are corrected for instrumental effects and contamination. One challenge of using these instruments in space is the large amount of data that is generated compared to the small amount of data that can be transmitted back to Earth. For example, at STATIC's maximum data volume, the onboard computer could create packages of counts as a function of 64 energies, 16 deflector angles, 16 anode angles, and 1024 TOF bins every 4 seconds. If counts are reported with 8 bits, every 4-second measurement would result in a staggering >100 Mbit array. Instead, the field programmable gate array (FPGA) inside the instrument sums data over various dimensions to reduce the amount of data reported to the onboard computer, MAVEN's Particles and Fields Data Processing Unit (PFDPU). Adjacent deflector, anode, or energy bins can be summed to reduce data volume. TOF bins are grouped into 64 mass channels, which vary slightly for each energy bin. Some of this data reduction is done by the FPGA, and the PFDPU performs further reduction before transmitting 22 standard data products back to Earth.

These standard data products must be designed with care by experimenters, who must pay close attention to mission requirements and calibration needs while keeping opportunistic science in mind. As an example, we will explain the procedure used to define data products for the Escape and Plasma Acceleration and Dynamics Explorers (ESCAPADE) mission's two ion ESAs, which are toroidal top hat analyzers similar to STATIC. The ESCAPADE ESA-ion (EESA-i) analyzers have 10 narrow and 6 wide anodes across 247.5° rather than 16 evenly sized anodes across 360°. Additionally, the energy-deflector sweeps are conducted over a period of 8 seconds, rather than 4 seconds. EESA-i typically produces 4 standard science products and 3 housekeeping products.

The ESCAPADE mission and instrument requirements that were used to guide the creation of data products are summarized as follows:

- Thermal (energy$<$ 2 eV) ion densities must be known within 30%;
- Suprathermal (2 eV $<$ energy $<$ 20 keV) ion energy fluxes must be known within 35%;
- Ion energies must be known within 25%;
- Light ions (M$<$4 amu) must be distinguished from heavy ions (M$>$16 amu);
- The field-of-view should cover 2π steradians with 30°x30° resolution;
- Sample times must be shorter than 20 seconds below 1000 km altitude and shorter than 40 seconds above 1000 km altitude.
- Including all data products, the average bitrate from the instrument must not exceed 210 bps (includes margin).

Two sets of the 4 standard data products were created for ESCAPADE due to the difference in required time resolution above and below 1000 km. The high altitude data products are summarized in Table 2.2 and the low altitude products are summarized in Table 2.3. For each data product in each altitude region with b bits per sample,

$$\text{bitrate} = \frac{\text{b}\mathrm{f}_1\mathrm{f}_2\mathrm{n}_\mathrm{E}\mathrm{n}_\mathrm{M}\mathrm{n}_\theta\mathrm{n}_\phi}{\text{ct}} \tag{2.19}$$

where f_2 is the fraction of the orbit in each altitude region and the other abbreviations are defined in Table 2.2. The average bitrate for all science data products is 174.95 bps. In addition to the science data products, three housekeeping data products used for in-flight calibrations are downlinked as often as possible while keeping the total bitrate below the required 210 bps. For comparison, MAVEN-STATIC is typically allotted 7000-14000 bps depending on the distance between Earth and Mars.

The primary science data product in both altitude regions is the Fine 4D data product, consisting of 3D velocity distribution functions for 3 mass bins that correspond to H^+, O^+, and O_2^+. Counts in adjacent energy bins are summed to reduce the number of bins from 64

Quantity	Fine 4D	Fine Energy	Fine Mass	Solar Wind
Energy Range	1.5 eV - 30 keV			20 - 200 eV
# Energy Bins, n_E	32	64	1	32
# Theta Bins, n_θ	8	1	1	8
# Phi Bins, n_ϕ	11	1	1	4
# Mass Bins, n_M	3	3	64	2
Sample Time, t	32 s	8 s	16 s	72 s
Fraction of Sweeps Downlinked, f_1	0.89			0.11
Estimated Compression Ratio, c	22.13	4.67	1.58	12.32
Average Bitrate	76.00 bps	32.74 bps	16.13 bps	1.84 bps

Table 2.2: A description of the 4 standard data products created by the ESCAPADE EESA-i instrument above 1000 km. On average, 89.59% of the ESCAPADE orbit is above 1000 km. The solar wind product is created from a single 8-second integration obtained every 72 seconds (8/72 = 0.11), using a specialized energy table. Data collected from each 8-second integration during the other 64 seconds of each 72-second cycle are summed to create 2 Fine 4D packets, 8 Fine Energy packets, and 4 Fine Mass packets. Compression ratios were estimated by resampling data obtained by MAVEN-STATIC to resemble the proposed data products, then compressing packets using the ESCAPADE flight software.

to 32, reducing the packet size by a factor of 2. Due to the layout of the EESA-i anodes, it is impossible to create evenly sized bins by summing adjacent anodes, so 11 anode bins are created with as equal sizes as possible. The average angular bin size is 11.1°x22.5°.

The other science data products obtained throughout the orbit are the Fine Energy and Fine Mass products. The Fine Energy product has the same 3 mass bins as the Fine 4D product, but is summed over all directions. All 64 energy bins are preserved, providing an energy resolution of 14.3%. Such fine energy resolution is useful for measuring temperatures of beam-like ion distributions, such as thermal ions focused into a beam as the spacecraft moves past supersonically. The Fine Mass product contains 64 mass channels, enabling the identification of minor ions, but is integrated over all angles and energies. This product is intended to inform experimenters about the presence of minor ions, which can bias calculations of ion density, temperature, and bulk velocity. The Fine Energy and Mass products can also be used to identify the transition from cold plasma dominated by planetary heavy ions to light, energetic solar wind ions at finer time resolution than the Fine 4D product. Observing plasma flow across these boundaries is a major goal of the ESCAPADE mission which is enabled by decreasing sample times.

One data product, the Solar Wind product, is only produced above 1000 km. This product uses a specialized energy sweep to achieve finer energy resolution, meaning that

Quantity	Fine 4D	Fine Energy	Fine Mass
Energy Range	0.5 eV - 4 keV		
# Energy Bins	32	64	1
# Theta Bins	8	1	1
# Phi Bins	11	1	1
# Mass Bins	3	3	64
Sample Time	8 s		
Fraction of Sweeps Downlinked	1.0		
Estimated Compression Ratio	22.13	4.67	1.58
Average Bitrate	39.74 bps	4.22 bps	4.28 bps

Table 2.3: A description of the 3 standard data products created by the ESCAPADE EESA-i instrument below 1000 km. Changes from the high altitude products are highlighted in red. On average, 10.41% of the ESCAPADE orbit is below 1000 km.

adjacent integrations cannot be summed together to reduce data volume. At altitudes above 1000 km, 8 integrations are performed using the nominal energy sweep of 1.5 eV-30 keV, followed by a 9th integration using the solar wind energy sweep of 20-200 eV. 8 deflector bins and 4 anode bins are downlinked to make sure the solar wind is within the field-of-view.

Different time resolutions were chosen for high and low altitudes to maximize science return while keeping the average bitrate within the data budget. At high altitudes, the fine 4D product is a sum of 4 adjacent 8-second sweeps, yielding a time resolution of 32 seconds. Decreasing the time resolution to 16 or 8 seconds significantly increases the data volume, while 32-second resolution meets the requirement of < 40 seconds. The Fine Mass product is a sum of 2 8-second sweeps, while the Fine Energy product is downlinked for every sweep. These products enable experimenters to understand some effects seen in the Fine 4D product that might be due to the long integration time or the presence of minor ions.

At low altitudes, where features of interest have smaller length scales, all data products are produced at the finest possible time resolution, 8 seconds. The data volume remains manageable because altitudes <1000 km are only $\sim$10% of the orbit. A different energy sweep is also used to obtain finer energy resolution measurements of thermal ions (dE/E = 13% for the Fine Energy product).

The final three data products produced by EESA-i are used primarily for calibration. The first is the rates product, which is downlinked for every 8-second sweep and used for background subtraction (see Section 2.3). If the count rate in the energy-theta-phi bin with the highest rate is known, the rates in every energy-theta-phi bin can be estimated from the peak rate, using the number of counts in each bin as a weighting factor. Therefore the rates product can be very small, consisting only of the count rate in the energy-theta-phi

bin with the highest rate, the anode number, and the energy-theta bin number. The start and stop rates can differ because the efficiency with which secondary electrons are generated is a property of the individual carbon foils. The different efficiencies also result in events where a start or stop pulse can be missing. Some events are determined to be invalid by the TOF logic as discussed in Section 2.3. Because the number of bits required is so small, it is possible to downlink 6 rates (Start, Stop, StartNoStop, StopNoStart, valid, and invalid) for the 3 anodes adjacent to the peak anode. The final rates product therefore consists of 22 numbers downlinked every 8 seconds: the number of the energy-theta step with the peak rate, the 6 rates from the 3 anodes where the peak rate occurs, and the 3 anode numbers.

The other two housekeeping data products are very large products that are downlinked infrequently, only a few times per orbit. One product is 64 energies by 64 masses and integrated over all look directions. This product resembles the 'c6' STATIC data product and is useful for characterizing coincident backgrounds. The other product is integrated over all energies and look directions but separates the mass channels into the maximum of 512 TOF bins. The TOF product is useful to characterize energy straggling for different species and look for changes in the behavior of the carbon foils.

The goal of this section has been to show how the large amounts of data generated by modern ESAs can be summed and down-sampled in order to maximize science return and enable quantification of errors while maintaining a reasonable data volume. Different combinations of data products can be used to meet all the science goals of a mission – for example, the EESA-i Solar Wind data product is optimized to address ESCAPADE mission requirements related to monitoring upstream conditions at Mars, while the other data products enable the study of cold planetary ions, precipitating ions, and pickup ions.

In the next section, we will examine instrumental effects that can result in errors in data interpretation.

2.5 Pitfalls for Experimenters

There are many potential complications in analyzing data from modern ESAs, not all of which are predictable and not all of which can be easily corrected for in an automated fashion. For example, STATIC encountered an unanticipated problem that came to be known as "ion suppression," which is believed to be a consequence of oxidation of the Ebonol-C coating of the top cap and hemispheres. It is thought, though it cannot be proven, that the work function of the Ebonol-C was altered by interactions with high fluxes of atomic oxygen in Mars' atmosphere, resulting in an effective detuning of the ESA. Only the surfaces exposed to atomic oxygen were altered, meaning that the degree of alteration of the work function decreases further into the ESA. The voltage difference across the hemispheres is not uniform along the path traversed by the ions. The detuned ESA acts like two ESAs in series which are set to slightly different energies, reducing the total throughput of the analyzer. Identifying this problem was not straightforward, in particular because the effect is not constant in time or across different portions of the entrance aperture. This situation can be avoided

or mitigated by using chemically inert coatings. (Note that Ebonol-C, as a cupric oxide, was thought to be chemically inert before MAVEN launched. ESCAPADE's ESA-i will use gold-black in place of Ebonol-C in hopes of avoiding this problem.) Once the unexpected behavior of the ESA was understood, it took years of data analysis to develop automated corrections for this issue. The corrections work well enough that thermal ion densities and temperatures can be determined to within 10-20%.

One example of an issue that is not always correctable in an automated way is determining whether the bulk of the ion distribution is within the FOV. Sometimes this is easy, if a beam-like distribution lies in the center of the FOV. However, if the beam enters the analyzer near the edges, this calculation can be less straightforward to automate as the beam appears to 'flap' in and out of the FOV. Determining whether the bulk of the distribution is in the FOV is more difficult for broader distributions; an experimenter can never be certain about what is missing from the data. Sometimes the spacecraft itself can block portions of the FOV, but experimenters must consider whether they want to include partially blocked anodes in their analyses.

Other potential complications result from the inherent difficulties of making measurements on a moving platform. As the spacecraft moves through the ambient plasma, the analyzer constantly samples different populations, meaning that untangling spatiotemporal changes is impossible with a single measurement platform. The ESCAPADE mission is intended to address this problem by sending two spacecraft to Mars in a string-of-pearls configuration. However, sending multiple spacecraft does not solve every problem; near plasma boundaries or other highly dynamic environments, distribution functions might change on timescales faster than the instrument's energy sweep, so that any measured distribution function represents an average of two or more distinct distribution functions.

As an example, we will discuss one event where the distribution function was known to vary faster than the STATIC sweep time, which was described by [33]. During the studied event, proton densities were modulated at the same frequency as observed low-frequency magnetosonic waves ($\sim$0.05 Hz, see Figure 2.7). Steepening of the wave fronts in the time series data was suggested to be a signature of adiabatic heating of the proton gas. From ideal gas theory, it can be shown that the relationship between the density and temperature of the gas at the peak and trough of the fluctuations has the form:

$$\frac{T_2}{T_1} = \left(\frac{N_2}{N_1}\right)^{\gamma-1} \tag{2.20}$$

The hypothesized relationship was observed for 4 of the 7 observed wave cycles, while the other 3 wave cycles did not exhibit the expected behavior (Figure 2.8). While the wave period was longer than the STATIC energy sweep period of 4 seconds, the steepened edge of the wave was observed over $<$4 seconds. Because the shape of the proton distribution function changed significantly during the course of the measurement, the distribution constructed from the STATIC data was distorted and the anticipated relationship was not observed.

Using a simulated instrument, it is possible to show how the 4-second time resolution leads to the distortion in the measured distribution function. The virtual instrument samples a

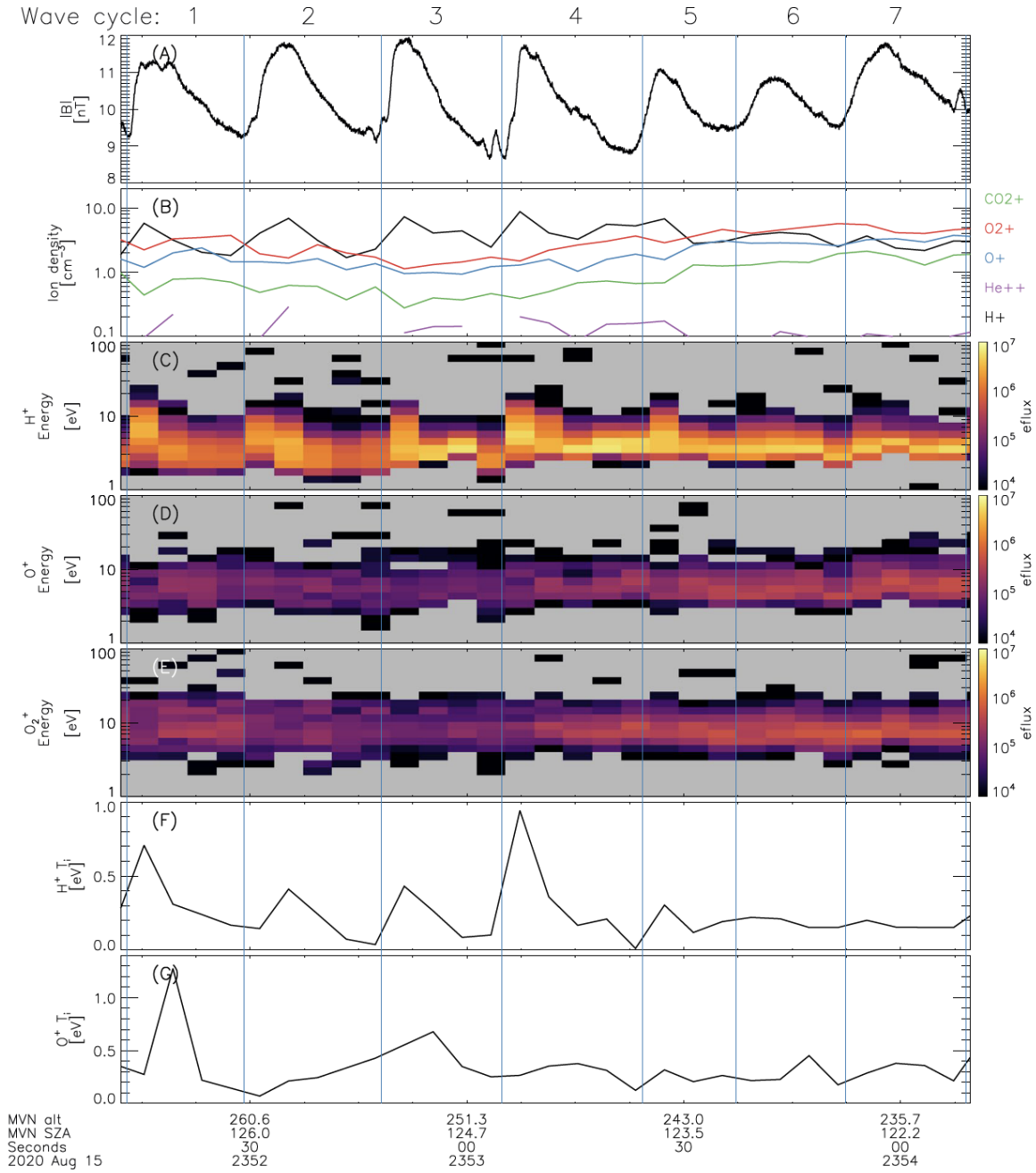

Figure 2.7: An example of a magnetosonic wave heating protons observed by MAVEN, reproduced from [33]. Panel A: Magnetic field amplitude. Panel B: STATIC ion densities. Panels C,D,E: STATIC energy fluxes for H^+, O^+, and O_2^+. Panels F,G: STATIC ion temperatures for H^+ and O^+.

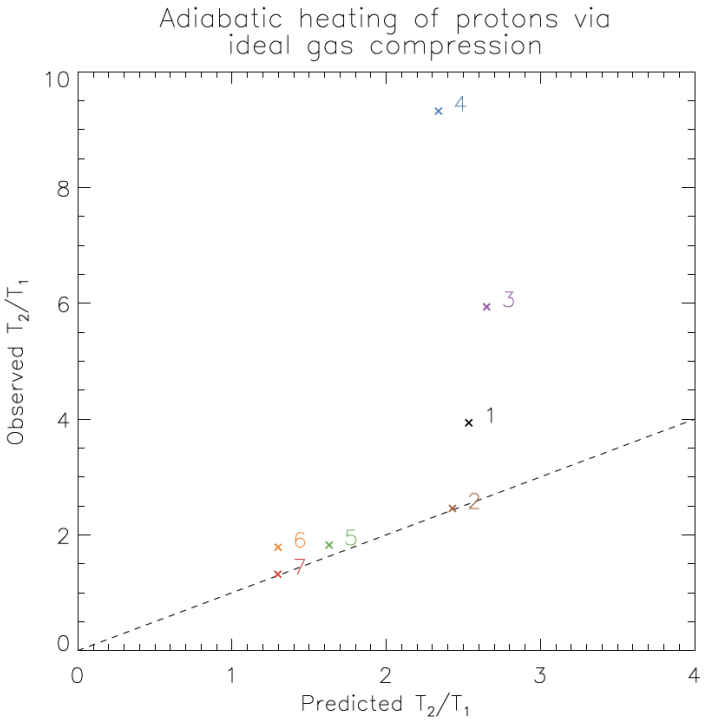

Figure 2.8: The relationship between the observed and predicted ratio $\frac{T_2}{T_1}$ reproduced from [33]. The dashed line indicates where the observations match the prediction. The observations are well explained by the theory for wave cycles 2, 5, 6, and 7, but not but cycles 1, 3, and 4.

simulated distribution function across 16 anodes while sweeping through energy and deflector steps during a set integration time, like the real instrument. The simulated distribution function can be constant or allowed to vary in time, so that the single distribution constructed by the virtual instrument can be compared to the input distributions.

During the event, the proton density was expected to be modulated in phase with the magnetosonic wave, so that 32 Hz measurements from MAVEN's magnetometer [16] could be used to guide the simulation of the proton distribution. The protons were modeled as a drifting Maxwell-Boltzmann distribution, including all known instrumental effects, with the density varying between $1.5/\text{cm}^3$ at the wave trough to $7/\text{cm}^3$ at the wave peak, consistent with the measured proton densities. For 3 of the wave cycles, the steepened edge of the wave was observed over a much shorter time than the 4-second sweep time (Figure 2.7A). Figure 2.9 illustrates the effect of the changing distribution function on the result of the measurement taken by the virtual instrument: the sampled distribution (black dots) is not representative of the changing distribution function (orange lines) throughout the sweep period. Since the distribution function is distorted, higher order moments that correspond

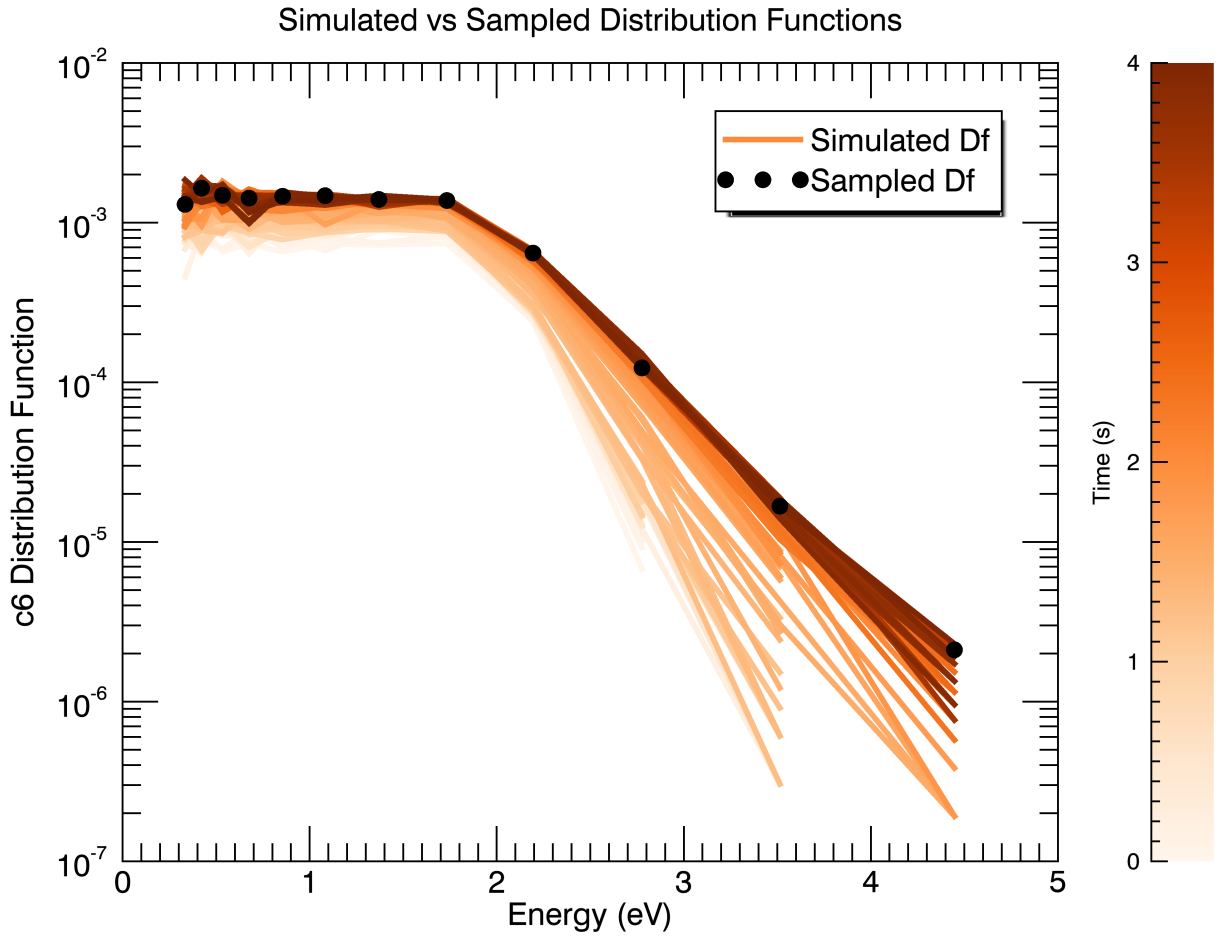

Figure 2.9: The 128 orange lines show how simulated proton distribution functions, based on 32 Hz magnetometer data, are likely to have changed throughout STATIC's 4-second measurement period. The black dots indicate the distribution actually sampled by a virtual instrument. See the text for more details.

to physical quantities such as density and temperature will be inaccurate. Similarly distorted measurements resulted in the failure of Equation 2.20 for 3 of the 7 wave cycles during the case study.

The operation of other instruments may also interfere with measurement of the distribution function. For example, a Langmuir probe can change the spacecraft potential throughout its I-V sweeps. If the timing of the I-V sweep lines up with the low-energy portion of the ESA energy sweep, the changing spacecraft potential can cause the acceptance energy of the ESA to change during the sweep, resulting in inaccurate measurements of the ion density.

The timing of the I-V sweeps must be coordinated with ESA energy sweeps in order to avoid such behaviors. On MAVEN, the I-V sweeps are generally timed so that the portion of the sweep during which the spacecraft potential changes quickly aligns with the high-energy portion of the STATIC energy sweep, where spacecraft potential is small compared to the energy.

2.6 Summary

This chapter has provided an introduction to using space-based electrostatic analyzers to measure mass-resolved ion velocity distribution functions, with a special focus on the MAVEN-STATIC instrument. We have discussed the geometry of electrostatic analyzers from optics to detectors, including the use of time-of-flight velocity analyzers. Details of converting from counts to physical units were provided, including correcting for spacecraft potential and an in-depth discussion of the background sources observed by STATIC. An example of the data products generated by an instrument similar to STATIC, the ESCAPADE ESA-i, was described. Finally, some examples of how the data can be biased by the instrument were discussed.

The previous sections have explained how a STATIC-like instrument can be used to measure accurate velocity distribution functions, with an emphasis on understanding how the design of the instrument affects its measurement capabilities. In the next chapter, we will develop the tools needed to systematically analyze velocity distribution functions and understand the physical properties of the ambient plasma, such as its density and temperature.

Chapter 3

Calculating major ion temperatures from distribution functions

3.1 Introduction

The previous section provided a guide for experimenters to accurately derive major ion distribution functions from space-based electrostatic analyzers. In this section, we will discuss the experimental challenges associated with analyzing these distribution functions, with a particular focus on calculating cold ion temperatures. The remainder of this chapter was published in the Journal of Geophysical Research: Space Physics in 2021 under the title "In Situ Measurements of Thermal Ion Temperature in the Martian Ionosphere" [45].

Ion temperature is an important parameter that influences the structure and evolution of atmospheres [84]. Ion temperatures affect collision and chemical reaction rates, so precise knowledge of ion temperatures and the chemical processes operating in planetary atmospheres enables a more thorough understanding of composition and structure in the photochemical region [36]. Ion temperatures also influence atmospheric dynamics and energetics. Specifically, hotter temperatures allow more ions to overcome gravity and reach altitudes above the exobase, where electromagnetic forces can accelerate ions to escape velocity. Understanding how ions are supplied to the exosphere is important for a complete description of ion escape during the present epoch [12], and can illuminate how ion loss might have varied under different conditions at earlier times. At Mars, ion escape to space is believed to be one of the major mechanisms through which the once Earth-like (i.e. 0.1-1 bar) atmosphere was lost [52], and escape of hot O through the dissociative recombination of O_2^+ dominates atmospheric loss in the present epoch [69, 52]. Measurements of ion temperature are necessary in order to investigate the poorly understood supply of planetary ions to the exosphere, their acceleration to higher altitudes, and the critical role that ion temperature is likely to have played in the climate evolution of the planet.

At Mars, ion temperature measurements thus far have been limited. The first measurements were made by retarding potential analyzers (RPAs) during the descents of the two

Viking landers in 1976 [47]. These measurements relied on fits of overlapping signals, and are sensitive to assumptions made about the relative abundances of different ions. Additionally, RPAs are sensitive to total current, and thus only provide a 1-D measurement. Subsequent measurements of 3-D ion temperature moments were provided by the ASPERA-3 instrument onboard Mars Express [5]. ASPERA-3 measurements are limited to altitudes above 300 km, too high to sample the cold ionospheric populations observed by Viking and in a regime where the spacecraft speed is usually smaller than the ions' thermal speed. Measuring colder ion temperatures at lower altitudes, where spacecraft velocities are larger than ion thermal velocities, is more complex and requires careful consideration of instrumental effects.

The basic structure of Mars' dayside ionosphere is well understood. Comprehensive reviews of the dayside ionosphere are available in [84], [93], and [44]. The dayside ionosphere is primarily a result of ionization and dissociation of atmospheric CO_2 by sunlight. The CO_2^+ is quickly converted to O_2^+ through chemical reactions, making O_2^+ the dominant ion. Since the ionosphere is dominated by a single species, the variation of ion density with altitude and solar zenith angle (SZA) is well-described by a Chapman function at low altitudes, with the ionospheric peak typically occurring near altitudes of 120 km at the sub-solar point and increasing to ∼180 km near the terminator [29, 30, 23, 42]. On the nightside, major sources of plasma include electron impact ionization and transport from the dayside [37, 57, 35, 41, 2], which is a function of ion temperature.

The vast majority of investigations of ion temperatures at Mars have relied on models which attempt to reproduce the two Viking descent profiles. Some of the first models created after the Viking missions [13, 38, 82] used Viking measurements as inputs to investigate the composition and structure of the ionosphere; [82] showed that accounting for the heat released during atmospheric chemical reactions was important for reproducing Viking profiles. Since Viking, many new types of models have been developed and used to study the Mars system. While each model includes different physics, many of the underlying assumptions are the same. Below the exobase (∼140-210 km), where the mean free path of a particle is shorter than its scale height, theory suggests that high collision rates will force ions, neutrals, and electrons to equilibrate. Most models, e.g. [4, 19, 65, 6, 63], assume that ion and neutral temperatures quickly converge a few scale heights ($\frac{kT_n}{m_n g} \sim 11$ km) below the exobase region, with the electron temperature converging at some lower altitude. At higher altitudes, the ion temperature is either estimated from the neutral and electron temperatures [19, 6], or calculated from kinetic or fluid approximations, often including some heat source from above the ionosphere (e.g. plasma waves) to improve agreement with Viking observations [4, 65, 63].

In this paper, we present the first measurements of thermal ion temperatures at Mars since the Viking RPAs. The Mars Atmosphere and Volatile EvolutioN (MAVEN) spacecraft has been in a 75° inclination elliptical orbit, with a typical periapsis altitude of ∼150 km, since late 2014 [54]. Orbit precession allows periapsis to sample all local times and latitudes from 75° S to 75° N. To date, the orbit has made seven revolutions in local time over a span of 3.3 Mars years. During nine one-week periods called Deep Dips (DDs), MAVEN lowered

its periapsis to ∼120 km, which approaches the top of the well-mixed lower atmosphere and samples the ionospheric main peak. In this study, we have used data collected by the SupraThermal And Thermal Ion Composition (STATIC) instrument to calculate O_2^+ temperatures for more than 150 MAVEN orbits spanning DDs 5-9. These new ion temperature measurements provide important new constraints on ionospheric chemistry and structure.

3.2 Methods for Calculating Accurate Cold Ion Temperatures

The STATIC instrument is a toroidal top hat electrostatic analyzer with electrostatic deflectors and a time-of-flight analyzer [70], located at the end of a 2-m boom on MAVEN's Articulated Payload Platform. Ions within a selected energy band pass through the analyzer and enter the time-of-flight section. By sweeping the analyzer and deflector voltages in a 4-second cycle, STATIC measures ions in 64 energy bins ranging from 0.1 eV to 30 keV over a 360°x90° field of view with mass resolution capable of distinguishing the main ionospheric and escaping species: CO_2^+, O_2^+, O^+, and H^+. To increase its dynamic range, STATIC is equipped with both a mechanical attenuator, which reduces ram fluxes by a factor of 100, and an electrostatic attenuator, which reduces fluxes by a factor of 10 across the entire field of view. Each attenuator can be activated independently. The five-dimensional (time, energy, azimuthal angle, polar angle, and mass) distribution functions are summed and possibly downsampled over one or more of the five dimensions, creating lower-resolution data products to reduce the amount of data that must be stored and transmitted to Earth. For most data products, pairs of adjacent energy bins are summed to reduce the number of energy bins to 32 or less.

We use two different data products, "c6" and "c8," to make two independent calculations of O_2^+ temperatures for each measured distribution. The c6 data product is summed over both angles to produce a distribution with 32 energy channels and 64 mass channels. We refer to the measurement based on the c6 data product, which calculates temperature based on ion velocity along the ram direction (Figure 3.1), as the "energy beamwidth." The c8 data product is summed over mass and instrument azimuth to produce a distribution of 32 energies and 16 deflection angles. At low altitudes, the ionosphere is dominated by a single species (O_2^+) and the instrument is oriented such that the deflection angle is orthogonal to the ram direction. This allows for a measurement of temperature based on velocity perpendicular to the ram direction, using the electrostatic deflectors. The temperature measurement based on c8 data is referred to as the "angular beamwidth." Background subtraction is performed separately for each data product and will be described in detail in a forthcoming publication.

Plasma temperature is usually calculated by integrating the second moment of a measured velocity distribution function $f_M(\vec{v})$ across the field of view of the instrument, and dividing

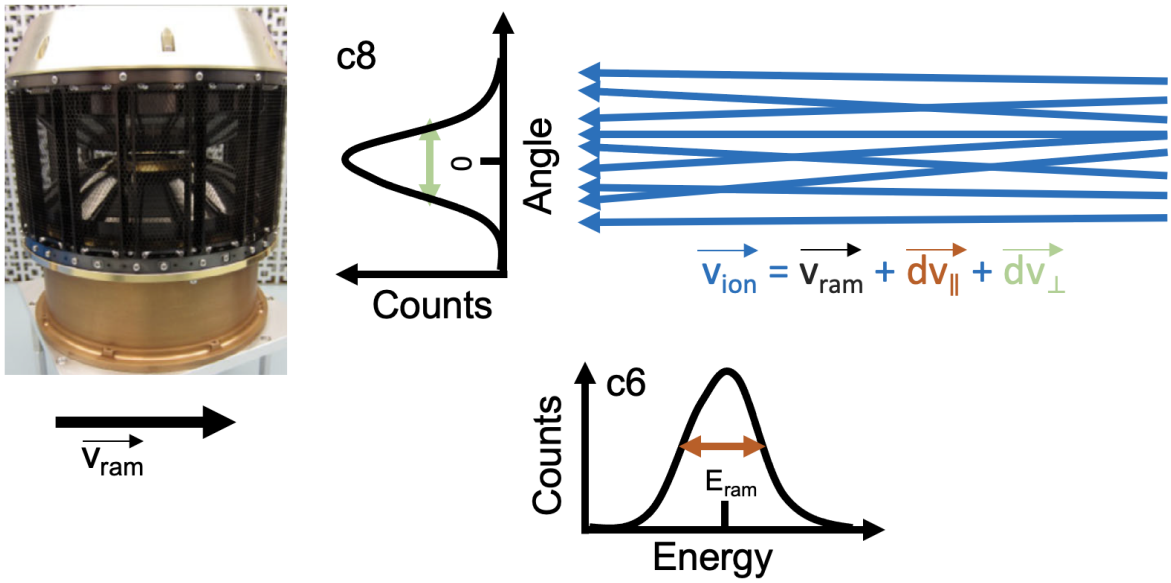

Figure 3.1: This schematic illustrates how STATIC measures the temperature of a cold ion beam while traveling supersonically. In the frame of the instrument, which has a spacecraft potential of V_{sc}, ions with charge q enter from the ram direction with energy $E_{\rm ram} = \frac{1}{2}{\rm m}v_{\rm ram}^2 - {\rm q}V_{sc}$. The variance of the velocity distribution function around the ram velocity provides a measurement of the temperature. Deviations in the velocity component parallel (perpendicular) to the ram direction are measured using the energy (angular) beamwidth from the c6 (c8) data product.

by the zeroth order moment, the density n:

$$T = \frac{1}{n}\int m(\vec{v} - \vec{v}_{\rm bulk})^2 f_M(v,\theta,\phi) v^2 \sin\theta dv d\theta d\phi \tag{3.1}$$

where m is the ion mass, $\vec{v}$ is the total ion velocity, and $\vec{v}_{\rm bulk}$ is the bulk flow velocity in the spacecraft frame. Equation 3.1 is valid if ion thermal velocities are greater than the spacecraft velocity because ions can enter the analyzer from any part of the field of view. However, for a spacecraft traveling much faster than the ion thermal velocity, as is the case for MAVEN periapsis passes, accurate determination of the ion temperature is more difficult. In this scenario, ions enter the analyzer as a beam centered on the single anode which faces into the ram direction. Integrating the measured distribution function over the instrument field of view using Equation (1) will yield an inaccurate result since typical beamwidths of 6° are much smaller than the anode resolution (22.5°). If the instrument is oriented as depicted in Figure 3.1, the temperature can still be accurately determined by calculating the variance of the distribution as a function of velocity parallel or perpendicular to the instrument. Both

temperature measurement methods rely on the assumption that the measured distribution is beam-like, i.e. the spacecraft travels supersonically so that thermal velocities are much less than the ram velocity (Figure 3.1). For omnidirectional c6 data, a beam is defined as a distribution in which 75% of the counts are measured in a certain number of energy bins surrounding the bin with the most counts after background subtraction, with the number of bins used depending on the instrument's energy and angular resolution. The threshold of 75% was chosen empirically to minimize data gaps while making sure derived temperatures are physically meaningful (see Section 3.3, paragraph 5).

An example of STATIC c6 and c8 data collected during a periapsis pass during a Deep Dip is shown in Figure 3.2A,B. Gaps in the energy flux in Figure 3.2A,B occur when the geometric factor changes during a measurement due to a change in mode or attenuator state. There are more data gaps in the c8 data due to how the onboard Data Processing Unit operates. If the velocity distribution function $f(v)$ is Maxwellian, the variance σ^2 of the measured distribution $f_M(v)$ is related to the temperature:

$$\sigma^2 = \int (v - v_{\rm bulk})^2 f_M(v) \mathrm{d}v = \frac{k_{\rm B}(\mathrm{T_{ion}} + \mathrm{T_{AC}})}{m} \tag{3.2}$$

where $\mathrm{k_B}$ is Boltzmann's constant; $\mathrm{T_{ion}}$ is the temperature of the ion distribution; $\mathrm{T_{AC}}$ is an analyzer correction due to a combination of instrumental effects; and v is the velocity parallel (perpendicular) to the ram direction for the energy (angular) beamwidth, corrected for spacecraft potential. The analyzer correction term appears because the measured distribution function $f_M(v)$ is a convolution of the actual distribution $f(v)$ and the analyzer response function $g(v)$, which can both be approximated by gaussians:

$$f_M(v) \sim (f * g)(v) \sim \int \exp \frac{-(v' - v_{\rm bulk})^2}{2\sigma_f^2} \exp \frac{-(v' - v)^2}{2\sigma_g^2} \mathrm{d}v' \tag{3.3}$$

where $\sigma_f^2 = \frac{k_{\rm B}\mathrm{T_{ion}}}{m}$, and $\sigma_g^2 = \frac{k_{\rm B}\mathrm{T_{AC}}}{m}$, and we have omitted the prefactors that determine the units. Since the convolution of two gaussians is a gaussian with a width equal to the sum of their individual widths, the finite contribution to σ^2 from instrumental broadening can just be subtracted off. When the distribution is broad enough that Equation (1) is valid (i.e. $\mathrm{T_{ion}} \gg \mathrm{T_{AC}}$), the instrument response can be ignored.

The conversion of count rate to $f_M(v)$ requires knowledge of spacecraft potential. Spacecraft potential is estimated from the STATIC data at 4 s cadence. At low altitudes (<180 km), potentials are estimated from the difference between the expected O_2^+ ram energy and the measured beam energy. At higher altitudes (>300 km), potentials are estimated from the minimum energy at which protons are observed. Between 180 km and 300 km, the lower of the two potential estimates is used, with some qualifications on count rates. In addition, this estimate is modified to account for the effect of changes in spacecraft potential produced by current-voltage (IV) sweeps conducted by MAVEN's Langmuir Probe and Waves (LPW) experiment [23] during each 4 s ion measurement.

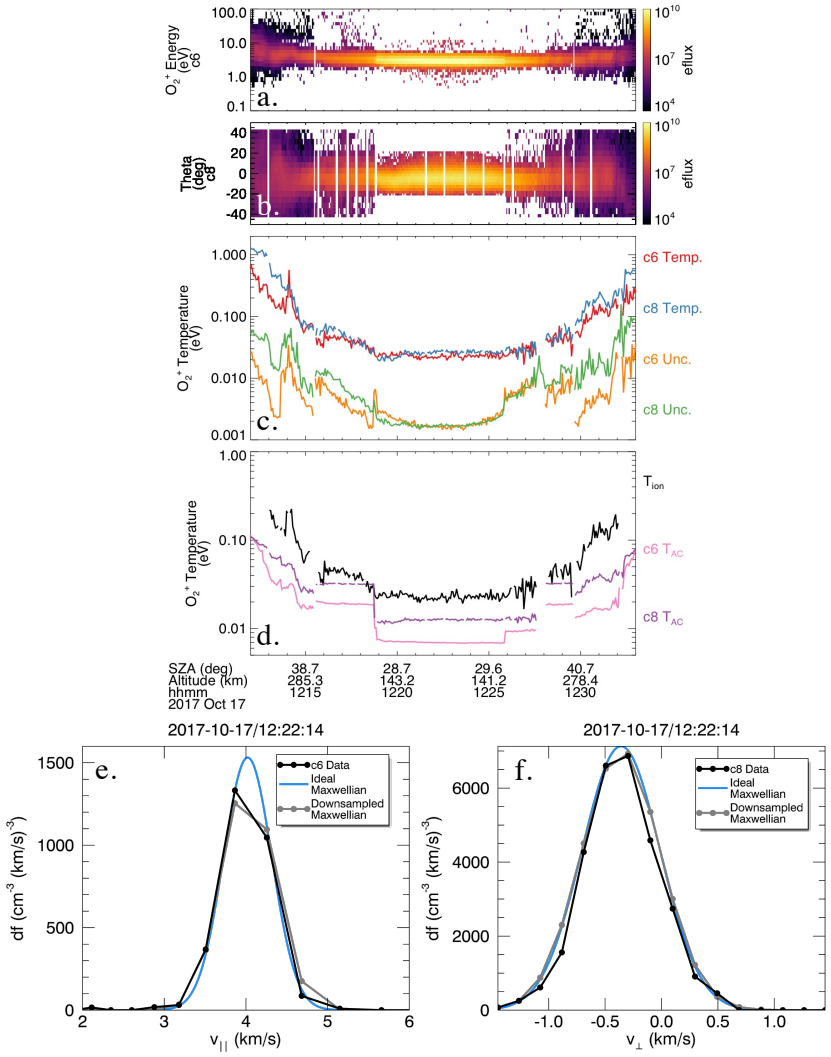

Figure 3.2: Panel A: c6 energy spectrogram for O_2^+ during one periapsis pass. Energy flux has units of eV/cm^2/s/steradian/eV. Panel B: c8 deflector angle distribution. Panel C: Measured O_2^+ energy (angular) beamwidth temperatures in red (blue), and statistical uncertainties in orange (green). Panel D: Final O_2^+ temperature in black and analyzer corrections for the energy and angular beamwidths in pink and purple. Discontinuities in T_{AC} reflect changes in mode and attenuator state, which impact instrument resolution. Panel E,F: A c6 (c8) distribution function, not corrected for spacecraft motion. The blue line is not a fit, but represents an ideal Maxwellian with the same temperature and bulk velocity as the measured distribution. The peak of the measured distribution is used as a scaling factor. The ideal Maxwellian is downsampled by averaging over each STATIC energy bin to produce the gray points. Peak magnitudes differ due to assumptions made about angular coverage of c6 data.

The analyzer correction is calculated and subtracted for each measured distribution through a process described in Section 3.2. The energy and angular beamwidth temperatures generally agree very well through periapsis (Figure 3.2C). Differences can result from the presence of a significant suprathermal population, rapid changes in spacecraft potential during a measurement, a change in beam velocity due to a change in winds (generally negligible) during a measurement, errors in the corrections for non-ideal analyzer response, errors in background subtraction, and statistical fluctuations. The uncertainties associated with each measurement method are shown in Figure 3.2D. Once the temperature has been calculated, the assumption of a Maxwell-Boltzmann distribution can be verified with a model (Figure 3.2E,F).

An algorithm was developed to (1) determine if each temperature calculation is likely to be valid and (2) select the most reliable of the two values (energy or angular beamwidth). Measurements can be invalidated if the count rate is too low; if $T_{AC} > 2T_{ion}$; if the spacecraft potential is unknown or is < -3.5 V; or if the peak of the distribution lies outside the field of view. The measurement with the smallest T_{AC}, usually the energy beamwidth, is considered to be most reliable. In regions where the algorithm might switch back and forth between data products at adjacent timestamps, potentially introducing false temperature fluctuations into the profiles, a second round of processing forces the algorithm to choose one method. Secondary processing is necessary on orbits where both calculations require larger corrections, such as orbits with highly negative spacecraft potential. For the majority of MAVEN periapsis passes, including the Deep Dip passes described here, the errors are small and do not significantly impact the results.

Removal of systematic errors

Before the temperature is calculated, the data are first corrected for an instrument effect known as "ion suppression." As different parts of the sensor are exposed to different fluxes of atomic oxygen at different altitudes and solar zenith angles, internal analyzer surfaces experience small changes in surface potential (contact potential or work function) due to chemical changes from exposure. These non-uniform changes have resulted in a time-varying detuning of the electrostatic analyzer. However, the effect of this detuning, other than reducing analyzer sensitivity (i.e. height of the distribution function), has an almost negligible impact on measured temperature (i.e. width of the distribution function). We include it primarily to rule out its influence on our measurements. By August 2015, sensitivity returned to a level that allowed reliable corrections for the sensitivity reduction to be applied for energies > 3 eV. We only use data collected after September 2015 in this analysis.

The analyzer correction T_{AC} is calculated independently for the energy and angle beamwidths and consists of 2 empirically derived terms: (1) $T_{response}$, a correction for the finite energy and angular resolution of the instrument and (2) $T_{scatter}$, a scattering term which is activated when the O_2^+ ram energy (after passing through the spacecraft potential) is > 4 eV. We will now explain the origin and form of each term in T_{AC}.

The analyzer response term corrects for the broadening introduced by the instrument's finite energy and angular resolution. Even if STATIC sampled a perfectly monoenergetic beam, the beam would appear to have some finite width due to the finite analyzer response as seen in Figures 12 and 13 of [70]. Additional broadening (i.e. smearing out in energy) is introduced by the onboard summing of adjacent energy bins described in Section 3.2. For any electrostatic analyzer with a high-voltage power supply, any ripple in the power supply will also introduce broadening, although this effect has not been observed for STATIC. Each of these effects can be removed using a term of the form:

$$T_{response} = \frac{\Delta E}{E} E_c \tag{3.4}$$

in which $T_{response}$ is given in eV, $\frac{\Delta E}{E}$ is the empirically determined analyzer response, and E_c is the characteristic energy obtained by dividing the beam's energy flux by its flux. This form results from the analyzer having an energy acceptance ΔE which is proportional to E, and from the use of a logarithmic energy sweep.

A scattering term was included in T_{AC} because energy dependent ion backscattering is observed by STATIC. At periapsis, ions that are scattered off the entrance aperture posts are sometimes detected entering the analyzer from the anti-ram direction. These ions are not observed when the spacecraft potential is near zero and the O_2^+ ram energy is $\sim$3 eV. However, for spacecraft potentials $<$ -1 V and O_2^+ ram energies $>$ 4 eV, these backscattered ions are observed with increasing relative flux with ion energy. These backscattered ions are eliminated in our temperature analysis. However, the same scattering processes are expected to happen on surfaces internal to the analyzer, resulting in an effective energy broadening. This energy broadening from scattering was first detected through changes in measured temperature associated with an observational procedure that caused spacecraft potential to change by 2 V on adjacent orbits. The broadening due to scattering was only observed when the O_2^+ beam energy was $>$ 4 eV, and the effective change in resolution was observed to plateau at higher energies. A search of the literature did not reveal any theory or measurements that describe scattering of low energy ions off surfaces (most low energy ions charge exchange to become neutrals). We therefore developed an empirical formula with the observed characteristics to correct for the scattering. The formula was verified using observational procedures that shifted the O_2^+ beam energy on adjacent orbits, so that temperatures measured under similar environmental conditions could be compared. The verification procedure will be described in detail later in this section.

Broadening due to internal scattering was removed using a correction of the form:

$$T_{scatter} = \begin{cases} 0 & \text{if } E_c < E_{scatter} \\ S_1 E_c \left(\frac{(E_c - E_{scatter})}{E_{scatter}} \right)^{S_2} & \text{if } E_{scatter} \leq E_c < (E_{scatter} + \Delta E_{scatter}) \\ S_1 E_c \left(\frac{(E_{scatter} + \Delta E_{scatter})}{E_{scatter}} \right)^{S_2} & \text{if } E_c \geq (E_{scatter} + \Delta E_{scatter}) \end{cases} \tag{3.5}$$

in which $E_{scatter}$ is the lowest energy at which scattering is observed and $E_{scatter} + \Delta E_{scatter}$ is the energy at which the broadening due to scattering stops increasing. The values of $E_{scatter}$,

Parameter	Energy Value	Angular Value
$E_{scatter}$	4.0	4.0
$\Delta E_{scatter}$	2.0	2.0
S_1	0.0065	0.0025
S_2	0.8	0.8

Table 3.1: STATIC Analyzer Correction Constants

$\Delta E_{scatter}$, S_1, and S_2 were determined empirically, and they differ for the energy and angular beamwidths (Table 3.1). Note that $T_{scatter}$ is zero for Deep Dip orbits, where the spacecraft potential is close to zero.

The forms and constants used for each term in T_{AC} were verified independently of one another. The procedures used to validate each correction will be described below.

The last known source of systematic error is variation in the spacecraft potential during the STATIC measurement of a cold ion beam. According to Liouville's theorem, the distribution function is corrected for spacecraft potential by simply adding the spacecraft potential to the measured ion energy, shifting the distribution function to lower energies for negative spacecraft potentials. However, the IV sweeps conducted by LPW can cause the spacecraft potential to change significantly (by tenths of a Volt) during the portion of STATIC's energy sweep when the ion beam is measured. Fortunately, LPW monitors these changes with sufficiently high time resolution so that the spacecraft potential can be calculated separately during each STATIC energy step. Without this correction, ion energies are shifted by the wrong spacecraft potential, which significantly alters the shape of the distribution function.

Sources of uncertainty

Sources of uncertainty in STATIC ion temperature measurements include random errors from statistical fluctuations, uncertainty in the spacecraft potential, and unidentified systematic errors in estimated T_{AC}, which are expected to be negligible. We have employed a set of rigorous processes to identify, correct, and validate sources of uncertainty in derived ion temperatures, which are described in detail in the next section. Our validation techniques suggest that uncertainties are small and derived ion temperatures are accurate.

The uncertainty introduced into each measurement by statistical fluctuations is plotted in Figure 3.2C. Poisson theory states that the uncertainty in the number of counts in a bin is given by the square root of the number of counts, N, which is assumed to be known exactly. However, for measurements obtained by spacecraft, N is measured only once and is subject to statistical fluctuations. Taking the statistical uncertainty to be the square root of $N_{measured}$ can therefore over- or underestimate the uncertainty in the temperature by as much as 35%, with larger effects for smaller values of N. To ensure accurate calculation of the statistical uncertainty, we simulate repeated measurements of each distribution with

random noise added, until N for the peak bin tops changing. The statistical uncertainty is then propagated in the usual way.

We examined the results of artificially changing the measured spacecraft potential on the temperature measurements, since uncertainty in the absolute spacecraft potential could be one of the biggest sources of uncertainty in our measurements. As we expected, the analyzer response correction $T_{response}$, which corrects for the different resolution of the instrument at different energies, causes the final measured temperature to shift by a small amount linearly, which should be negligible for nominal uncertainties of calculated potential.

Validation

Although no external dataset exists that covers all the conditions sampled by STATIC, the large volume of data collected by STATIC makes validation possible. The most compelling evidence that all systematic errors have been removed from STATIC data is the agreement between the two independent measurements of the O_2^+ temperature. The energy and angular beamwidths generally agree within 10% (Fig. 3.2C), and any significant discrepancies between them can often be explained on a case-by-case basis.

The terms in the temperature correction T_{AC} were calculated independently using empirical methods and ground calibrations. These corrections have been validated via investigation of hundreds of orbits spanning a range of conditions that are known to influence T_{AC}, including spacecraft orientation, instrument mode, attenuator state, and solar zenith angle. These orbits also sampled many different geographic locations, Mars seasons, and solar conditions in order to verify that accurate, continuous temperature profiles are produced regardless of environmental conditions. We will now describe how each term in T_{AC} was independently verified.

The analyzer response term $T_{response}$ varies with instrument mode and attenuator state. STATIC's energy and deflector sweeps sample different energy and angular ranges depending on instrument mode, but the 4-second sweep time is constant. The energy and angular resolutions are therefore different in different modes and require different corrections. Additionally, the energy-angle response differs if ions can enter across the entire field of view, or are restricted to the edges by the attenuators. The form and constants used to calculate $T_{response}$ were determined from analyzer design simulations and ground calibrations [70], and then slightly adjusted to eliminate discontinuities in temperature profiles which coincide with changes in instrument mode and attenuator state.

The analyzer response correction was also verified using a simulation. Maxwellian distribution functions of known temperature, density, and drift velocity were generated and sampled using a simulated version of STATIC. We used the empirically derived analyzer response functions to introduce instrument broadening, measured the temperature as described above, then applied the analyzer broadening correction $T_{response}$. A random number generator was used to account for the effects of statistical fluctuations. The simulation was repeated for all combinations of activation states of the mechanical and electrostatic attenuators; the results are shown in Figure 3.3. Above 100 K, the analyzer broadening is

successfully corrected. Residual errors average around 5% for ion temperatures of 100 K and grow significantly for colder temperatures. Measurements of corrected temperature below 60 K, where the corrected temperature levels off in Figure 3.3E, are removed from the dataset.

The scattering term $T_{scatter}$ is a function of spacecraft potential, which can be intentionally varied by flying the spacecraft in different orientations. Since large (i.e. order-of-magnitude) changes in temperatures below the exobase region are not expected between adjacent orbits, corrections based on the spacecraft potential can be tested by varying the attitude of the spacecraft on adjacent orbits and comparing the measured temperature profiles. Specifically, the spacecraft is oriented so that ram flow impacts the solar panels edge-on ("Fly-Y") or face-on ("Fly-Z"). In Fly-Y, the ram ion current is collected by the side of the spacecraft bus facing the flow and by the "gull-wing" outer segment of the leading solar panel with its conducting back face at an 80° angle to the flow. In this configuration, the total ion current is somewhat less than the electron current, so the spacecraft charges a few Volts negative to repel some of the electrons and achieve zero net current. However, in Fly-Z, the broad faces of the backs of the solar panels collect enough ion current to cancel the electron current, so the spacecraft potential is close to zero. A representative value for spacecraft potential at periapsis in Fly-Z is -0.12 V, while the spacecraft potential ranges from -1 to -4 V in Fly-Y. We have conducted six "Alternating Fly-Y Fly-Z Campaigns" of 11-15 orbits each in order to verify the scattering correction. An example of data collected during a campaign that took place May 28-30, 2019 is shown in Figure 3.4. There is no significant difference between temperatures measured in either orientation. MAVEN is always oriented in Fly-Z during Deep Dips, meaning that $T_{scatter}$ is small. If the spacecraft was oriented in Fly-Y before or after the Deep Dip, temperatures can be compared to look for changes in $T_{scatter}$ as a result of the Deep Dip. Such a comparison is shown in Figure 3.5. The shapes of the profiles cannot be compared directly because different solar zenith angles are sampled before and after the Deep Dip; however, the variation in measurements does not appear to change, giving confidence that the effects causing the scattering are understood. The warmer angular beamwidths observed below 130 km might indicate an underestimate of the angular component of $T_{scatter}$ in that region.

Finally, we can compare profiles measured by STATIC to the profiles measured by the Viking RPAs (Figure 3.6). Viking 1 landed at 16:00 local time, near the Northern summer solstice with a solar longitude $L_S = 97°$ and Viking 2 landed at 10:00, $L_S = 117°$. MAVEN's orbital configuration is closest to the Viking lander trajectories during DD 8 for which periapsis occurred at 14:00 and $L_S = 76°$. At altitudes above the exobase, agreement between STATIC and both Vikings is good. At lower altitudes, both Vikings measured substantially colder temperatures than STATIC observed during DD 8. The difference in Viking profiles and DD 8 profiles cannot be explained by solar activity: we estimate solar Lyman-alpha fluxes at Mars of 2.2×10^{-3} W/m^2 and 2.4×10^{-3} W/m^2 for Viking 1 and 2, and 2.2×10^{-3} W/m^2 for DD 8. Values of composite solar Lyman-alpha fluxes were taken from the LASP Interactive Solar Irradiance Datacenter and extrapolated to Mars using the method described in [87]. It is important to note that at different local times, STATIC can and does observe temperatures as cold as those measured by the Viking landers. The median temperature

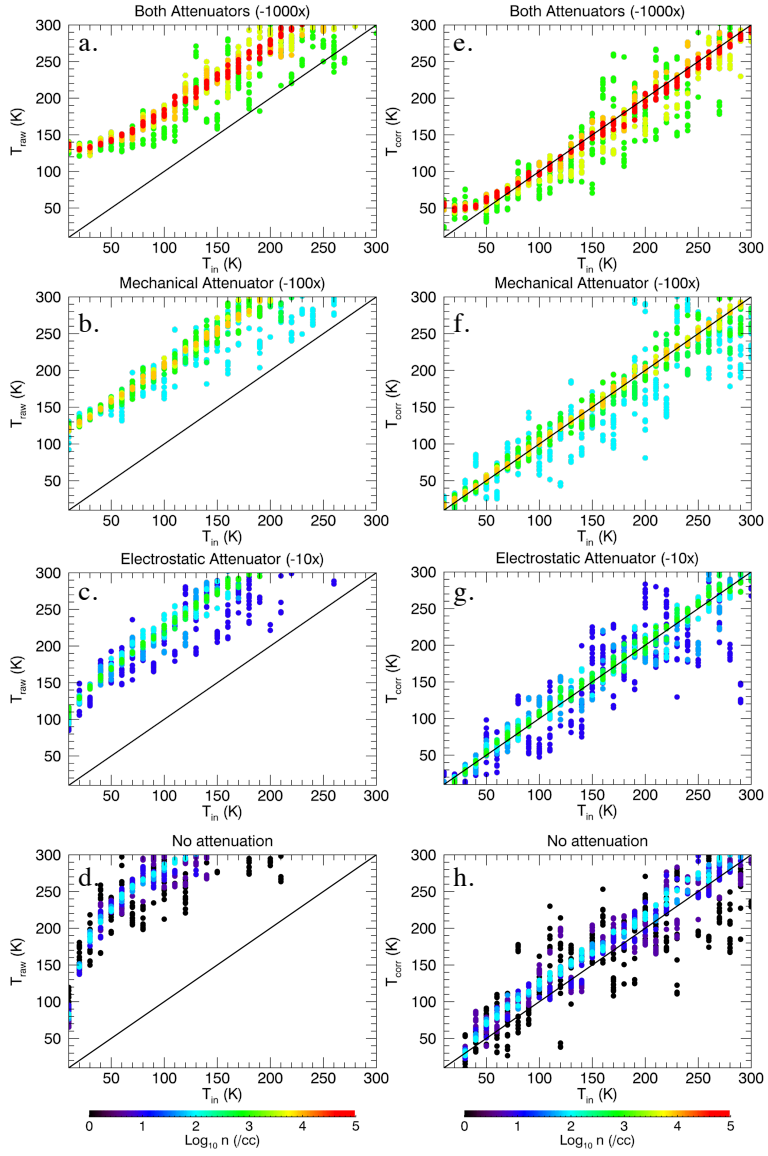

Figure 3.3: O_2^+ energy beamwidth temperatures, (A-D) raw and (E-H) corrected for analyzer response, as a function of the temperature T_{in} of a simulated Maxwellian distribution measured with a simulated STATIC. Color indicates the density of the simulated distribution function. Each row of figures represents a different attenuator state; the number in parentheses indicates the factor by which the ram flux is reduced. The effects of ion suppression and scattering are not included in the simulation. Ion suppression does not affect the temperature measurement; $T_{scatter}$ is zero during the passes analyzed in this work.

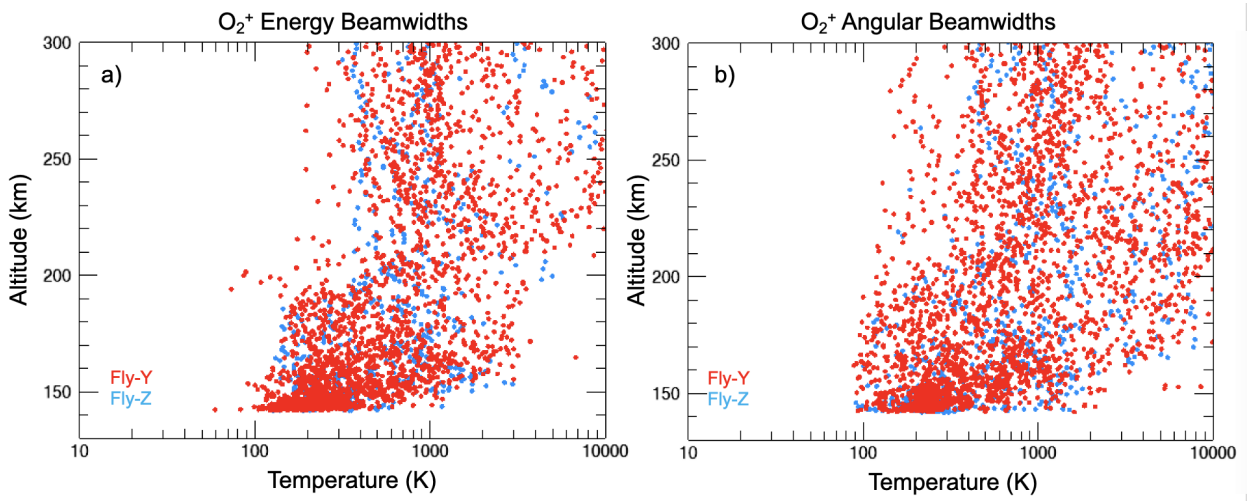

Figure 3.4: (A) Energy beamwidths and (B) angular beamwidths for O_2^+. Red dots represent measurements taken when MAVEN was in the Fly-Y attitude, where spacecraft potential is typically a few volts negative. Blue dots represent measurements taken in Fly-Z, where spacecraft potential is near zero.

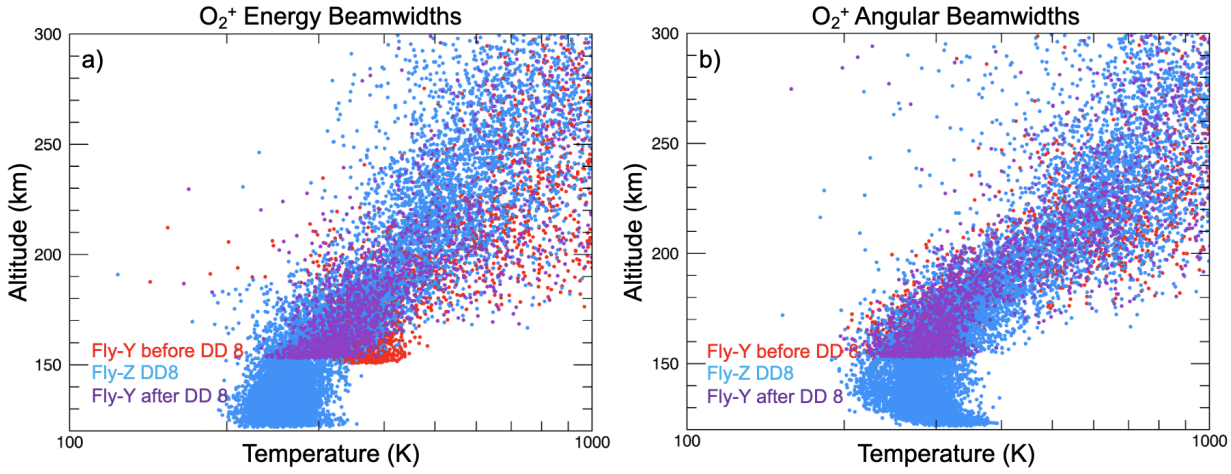

Figure 3.5: (A) Energy beamwidths and (B) angular beamwidths for O_2^+. Red dots represent measurements taken when MAVEN was in the Fly-Y attitude before Deep Dip 8, where spacecraft potential is typically a few volts negative. Purple dots are data taken with same attitude after the Deep Dip. Blue dots represent measurements taken in Fly-Z during the Deep Dip, where spacecraft potential is near zero.

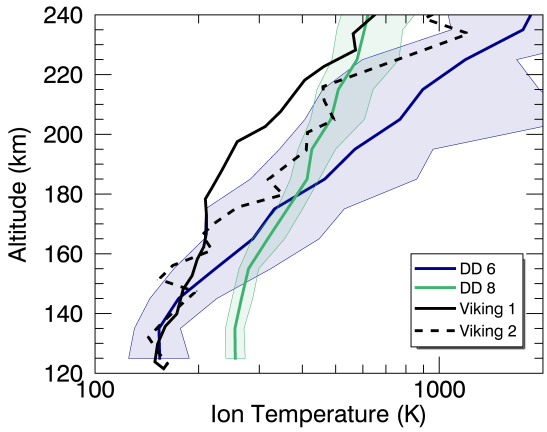

Figure 3.6: Median O_2^+ temperature profiles measured by STATIC during DDs 6 and 8 compared to the Viking RPA ion temperatures. Shaded regions indicate upper and lower quartiles for each 10-km altitude bin.

profile measured during DD 6, which occurred at 01:00 and $L_S = 194°$, is included in Figure 3.6 to illustrate the large variety of temperatures measured by STATIC at different locations.

The measurements and discussion presented here indicate that the corrections needed to calculate ion temperatures from STATIC data are well understood.

DD	Orbits	Latitude	SZA (°)	Local Time (h)	L_S (°)	Crustal Field
5	3285–3327	33.2°N	95	5.2	166.9	No
6	3551–3586	2.9°S	140	0.7	194.4	No
7	5574–5620	63.6°N	88	20.3	49.4	No
8	5909–5950	18.9°S	25	13.7	76.3	No
9	6935–6973	47.8°S	16	11.9	165.8	Yes

Table 3.2: MAVEN Deep Dip Periapsis Ephemeris Data

3.3 Measurements of Ion Temperature near Mars' Main Ionospheric Peak

Median O_2^+ temperature profiles measured during DDs 5-9, each of which occurred at different local times, are plotted in Figure 3.7, with upper and lower quartiles indicated by the shaded regions. Temperature measurements are binned by CO_2 density measured by the Neutral Gas and Ion Mass Spectrometer (NGIMS) [64] and median values indicate the median temperature measured in each pressure bin. The largest differences between Deep Dip profiles are likely due to the different solar zenith angles during each Deep Dip. The ephemeris data for each analyzed Deep Dip was taken in part from [86] and is shown in Table 3.2.

We find that dayside profiles are warmer than nightside profiles below the exobase region (∼140-210 km). At periapsis, the median temperature at 14:00 was 255 ± 13 K, compared to 162 ± 32 K at 01:00, where the given ranges indicate upper and lower quartiles rather than uncertainty. Dusk temperatures are warmer than dawn temperatures, which are of similar magnitude to temperatures at midnight. The neutral atmosphere is also warmer at dusk than at dawn [86], having been warmed by sunlight throughout the day, so this trend is likely explained by thermal inertia. However, we also note that MAVEN and the ionosphere were in darkness during the inbound orbit segments of DD 5, while DD 7 took place on the sunlit side of the terminator.

Below the exobase region, O_2^+ temperature measurements for subsequent orbits for which local solar time, latitude, and solar irradiation are similar are highly repeatable. Nightside temperatures are more variable than on the dayside. We expected higher variability on the nightside due to the patchy nature of electron impact ionization, which is a significant source of nightside ionospheric plasma [2].

Above the exobase, acceleration and heating by electromagnetic forces and waves on some orbits lead to a wider range of observed O_2^+ temperatures at all local times. A future study will investigate the ion heating processes operating near the exobase. Some differences in DD profiles may be driven by variations in solar flux due to changing seasons; an extensive discussion of the solar EUV flux measurements during DDs can be found in [86].

Interpretation of ion temperatures measured above the exobase must be handled care-

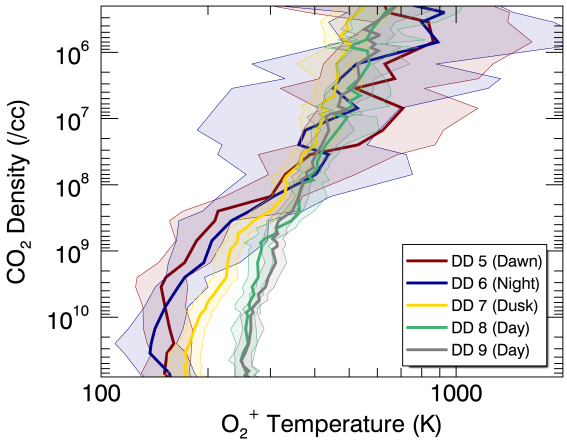

Figure 3.7: Median O_2^+ temperature profiles measured by STATIC during the inbound orbit segments of each orbit during DDs 5, 6, 7, 8, and 9, then binned by CO_2 density measured by NGIMS. Shaded regions indicate upper and lower quartiles.

fully. As stated, both the angular and energy beamwidth methods assume the presence of a dominant Maxwellian core to the distribution. Above the exobase, electromagnetic forces and precipitating pickup ions can lead to the development of a suprathermal tail on the ion distribution, invalidating our assumption of a perfect Maxwellian. While the temperature calculated using our method still accurately characterizes the Maxwellian portion of the distribution, the core temperature does not accurately describe the suprathermal portion of the distribution, which may contain a significant amount of energy compared to the cold core. Temperatures calculated using the second moment (Equation 3.1) will always be higher than

the core temperatures derived from the energy and angular beamwidths.

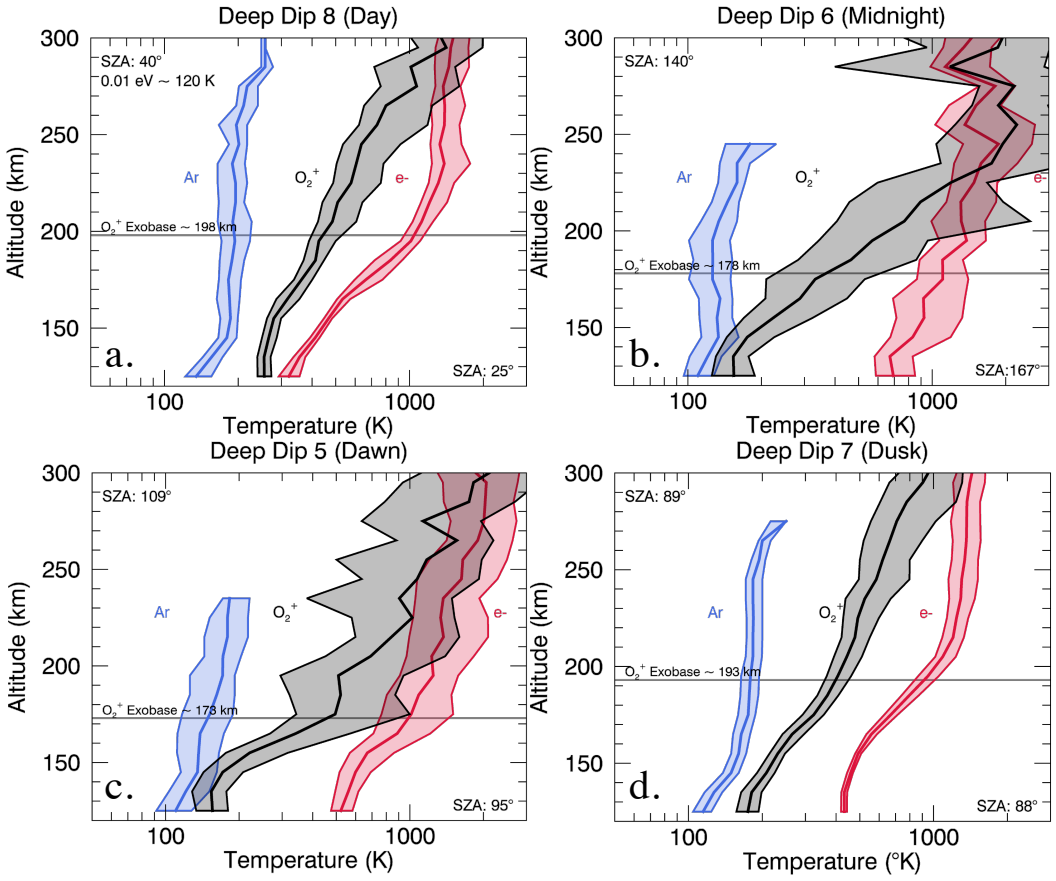

Figure 3.8: Median temperature profiles as a function of altitude for O_2^+, Ar, and electrons collected during (A) Deep Dip 8 at 14:00 local time, (B) Deep Deep 6 at 01:00, (C) Deep Dip 5 at 05:00, and (D) Deep Dip 7 at 20:00. O_2^+ temperatures from STATIC are shown in black, neutral Ar temperatures measured by MAVEN NGIMS are shown in blue, and electron temperatures from MAVEN LPW are shown in red. Shaded regions represent upper and lower quartiles. Solar zenith angles at the top and bottom of the profiles, which vary by 16° at most, are indicated on the plots. Exobase altitudes indicate where the ion scale height exceeds the mean free path between ion-neutral collisions.

Figures 3.8 and 3.9 show temperature profiles for O_2^+, Ar, and electrons measured during MAVEN DDs 5-8. The Ar temperature is measured by MAVEN NGIMS using a scale-height method based on the work of [17] and described by [86]. Though Ar is not the dominant neutral species, all neutral species have been measured to have the same temperature throughout this altitude regime, and since Ar is a noble gas, its temperature is less sensitive to instru-

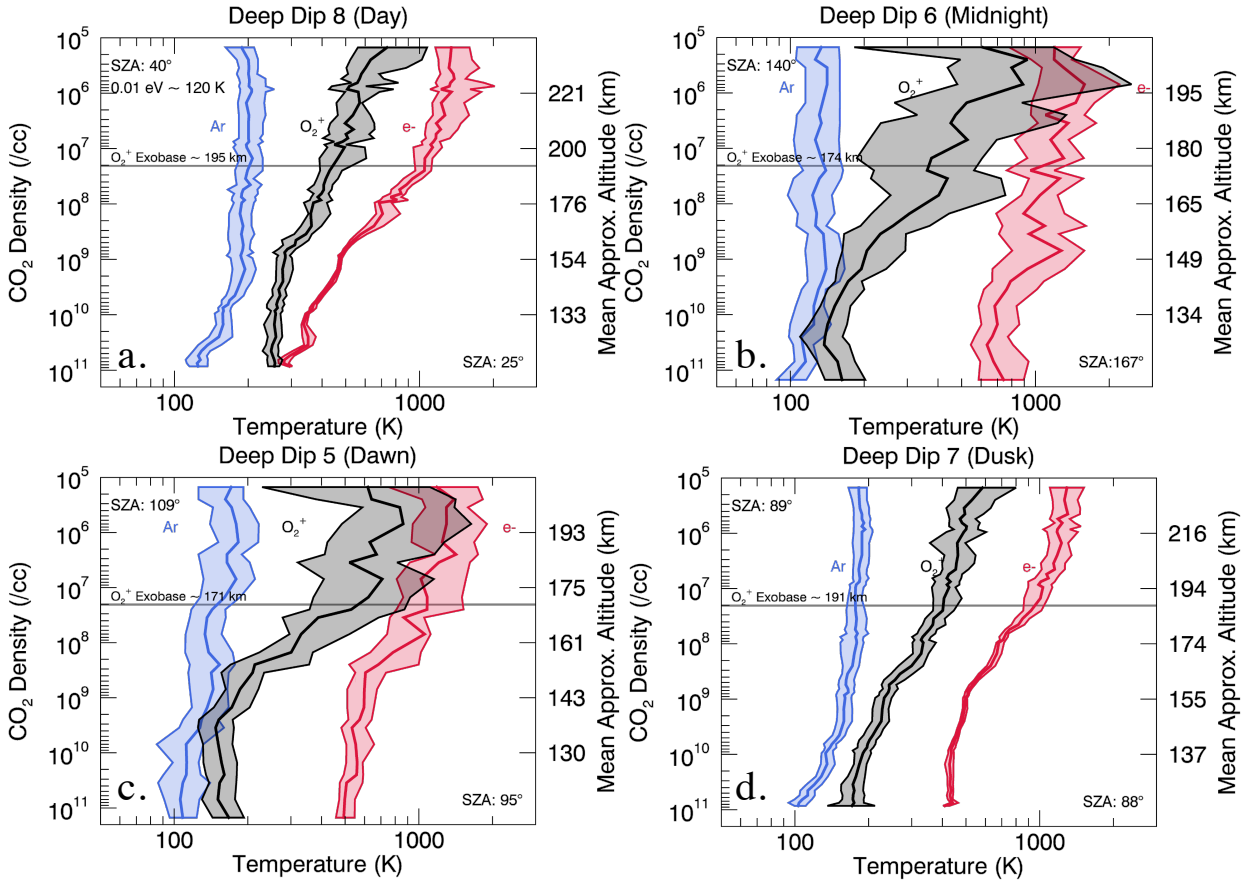

Figure 3.9: Median temperature profiles as a function of CO_2 density for O_2^+, Ar, and electrons collected during (A) Deep Dip 8 at 14:00 local time, (B) Deep Deep 6 at 01:00, (C) Deep Dip 5 at 05:00, and (D) Deep Dip 7 at 20:00. O_2^+ temperatures from STATIC are shown in black, neutral Ar temperatures measured by MAVEN NGIMS are shown in blue, and electron temperatures from MAVEN's Langmuir probe are shown in red. Shaded regions represent upper and lower quartiles. Solar zenith angles at the top and bottom of the profiles, which vary by 16° at most, are indicated on the plots. Exobase altitudes indicate where the ion scale height exceeds the mean free path between ion-neutral collisions.

mental effects than the CO_2 temperature [86]. The electron temperature is measured by MAVEN's Langmuir Probe and Waves experiment, recalibrated as described by [26].

All temperature profiles plotted in Figures 3.7, 3.8, and 3.9 were derived from data collected only on inbound orbit segments for two reasons. First, Ar temperatures are not available on the outbound orbit segment due to increased levels of background in NGIMS, as discussed by [86]. Additionally, temperatures for all populations depend on SZA, so using

only measurements from the inbound orbit segment eliminates some of the variability caused by changing SZA.

Most interestingly, we find that temperature differences between ions, neutrals, and electrons persist down to the lowest altitudes sampled by MAVEN. Dayside ions are significantly hotter than the neutral atmosphere at all altitudes, while nightside ion temperatures approach neutral temperatures below the exobase, but are even hotter than dayside ions at high altitudes. Median periapsis O_2^+ temperatures are at least 15 K higher than median Ar temperatures at all local times. At the highest CO_2 densities during DD 8, the median O_2^+ temperature is 255 ± 13 K, while the median neutral temperature is 125 ± 11 K and the median electron temperature is 294 ± 7 K. On the nightside, during DD 6, the ion and neutral temperatures drop to 162 ± 32 K and 100 ± 14 K, while the electron temperature rises to 742 ± 154 K. High temperatures in the morning (DD 5) may be associated with the morning overshoot, which was observed in electrons and ions at Earth [28, 79] and has been seen in electrons at Mars [76]. The sustained temperature differences between populations, which are significant compared to the uncertainties, suggest that a fundamental piece of physics is missing from existing models of the Mars ionosphere, which assume that ion and neutral temperatures converge quickly below the exobase.

At higher altitudes, where neutral densities drop below 10^8/cc, nightside ion temperatures can approach and even exceed the electron temperature, reaching 1000s of K, while dayside temperatures remain well below 1000 K. At all local times, ion temperatures are hundreds of Kelvins higher than neutral temperatures for neutral densities lower than 10^8/cc. The convergence of ion and electron temperatures at higher altitudes is expected as the plasma transitions from collisional to magnetized [84]. Discrepancies between median ion and electron temperatures at high altitudes are likely to result from the exclusion of suprathermal ions.

3.4 Gaps in Understanding Ion Thermalization at Mars

Here we investigate the steps of ion production and thermalization in an attempt to identify processes that could energize ions at a sufficient rate to maintain the observed temperature difference between ions and neutrals. The even larger discrepancy between electron and neutral temperatures is discussed in detail by [25]. We begin with photoionization, which produces radicals that participate in a network of chemical reactions. We then consider Coulomb collisions with electrons, energy transport by ions, Joule heating, and interactions with electromagnetic waves, crustal magnetic fields, or the spacecraft itself. In order to quantitatively compare the different processes, we have used a 1-D fluid model of the Mars ionosphere coupled to a kinetic suprathermal electron transport model as described by [65] to calculate ion heating and cooling rates and the energy contribution due to thermal conductivity. Median ion, neutral, and electron density and temperature profiles from each Deep

Dip were used as model inputs; the input temperature profiles are shown in Figure 3.8 and the input density profiles are shown in Figure 3.10. Density and temperature profiles for all species were extrapolated down to 80 km using parametric fits to the measurements, as was done by [71] and [65]. The simulation results are plotted in Figure 3.11.

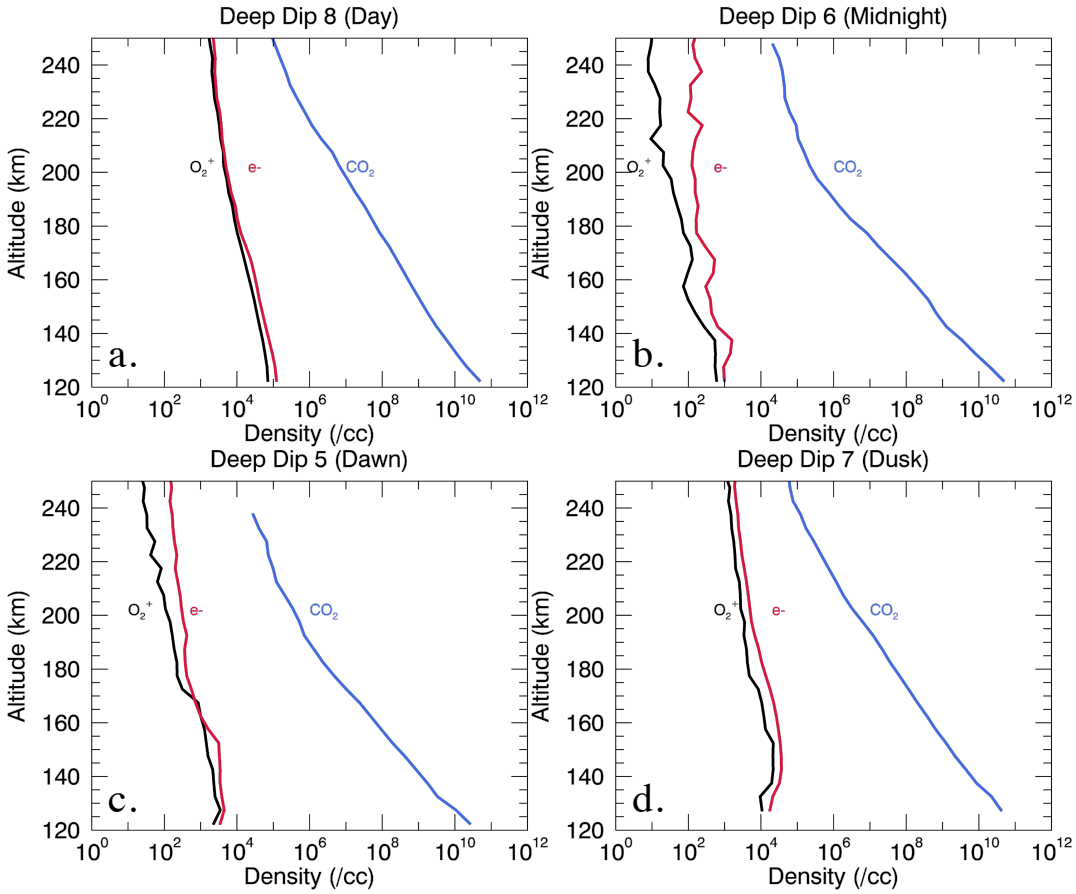

Figure 3.10: Median density profiles as a function of altitude for O_2^+, CO_2, and electrons collected during (A) Deep Dip 8 at 14:00 local time, (B) Deep Deep 6 at 01:00, (C) Deep Dip 5 at 05:00, and (D) Deep Dip 7 at 20:00. O_2^+ densities from STATIC are shown in black, neutral CO_2 densities measured by MAVEN NGIMS are shown in blue, and electron densities from MAVEN LPW are shown in red. Differences in O_2^+ and electron densities are partly due to the presence of additional ion species. Larger discrepancies may occur at high altitudes because uncertainties in electron density increase as the density decreases [35]. These differences do not significantly affect model output.

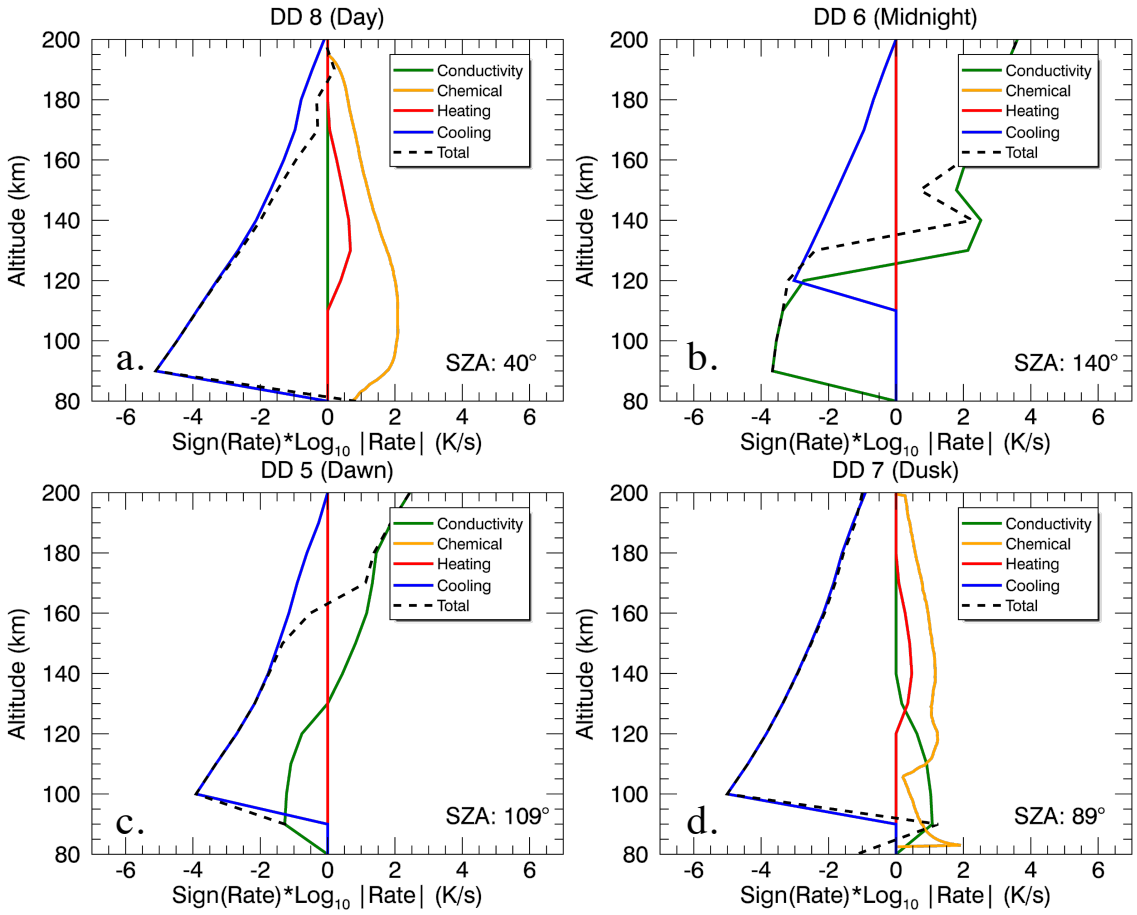

Figure 3.11: Heating and cooling rates for O_2^+ during DDs 5-8 assuming a single SZA as indicated on each plot. The log of each rate in K/s is plotted on the x-axis, where negative rates indicate cooling and positive rates indicate heating. Rates below 1K/s, which would result in a negative log, were excluded from the dataset. The thermal conductivity term accounts for the effects of temperature gradients, the heating rate represents the energy gained through Coulomb collisions with electrons, and the cooling rate represents the energy lost through collisions with neutrals. The conductivity, heating, and cooling terms are calculated using the [65] ionosphere model. The chemical heating term represents energy deposited by atmospheric chemistry and is calculated as described in the text.

Photoionization

The first step in the formation of ionospheric O_2^+ is the photoionization of CO_2, which is rapidly converted to O_2^+ via atmospheric chemistry. During photoionization, the majority of the energy in excess of the ionization potential is carried away by the much lighter electron,

while the energy delivered to the ion is usually assumed to be negligible.

The photoelectron spectrum near the peak of the Martian ionosphere has peaks between 21 and 24 eV and at 27 eV [38]. During the production of a 27 eV photoelectron from a CO_2 gas at 125 K, momentum conservation requires that the CO_2^+ ion gain a velocity that is lower than the electron's velocity by a factor of 10^{-5}, corresponding to ∼3 K of heating. Photoionization cannot provide the energy required to sustain the temperature difference between O_2^+ and neutral species, which was observed to be ∼130 K during DD 8.

Atmospheric chemistry

After photoionization, the CO_2^+ that is produced near the ionospheric peak is quickly converted into O_2^+ via a network of reactions:

$$CO_2^+ + O \longrightarrow CO + O_2^+ + 1.33\,\text{eV} \tag{3.6}$$

$$CO_2^+ + O \longrightarrow CO_2 + O^+ + 0.13\,\text{eV} \tag{3.7}$$

$$CO_2 + O^+ \longrightarrow CO + O_2^+ + 1.2\,\text{eV} \tag{3.8}$$

No measurements of the branching ratios, which describe the fraction of the products that are produced in each excitation state, have been made for Reaction 3.6 . However, [88] measured branching ratios for Reaction 3.8 and found that roughly 40% of the energy released in the reaction was partitioned to internal excitation of the O_2^+ ions. In order to estimate a chemical heating rate, we therefore assume that 40% of the energy released in each reaction excites internal states of the O_2^+, and the remaining energy is divided amongst the products according to their mass ratio. In total, the newly produced O_2^+ ion gains a translational kinetic energy of ∼0.35 eV, which will be transferred to the neutral population via collisions. If O_2^+ ions are produced faster than they can transfer this excess energy away, then the O_2^+ ions can maintain a higher temperature than the neutrals.

The chemical heating rate (orange line) in Figure 3.11 is not calculated by the model and was derived separately using O_2^+ production rates and electron density profiles plotted in Figures 3 and 5 of [66], assuming that ions gain 0.35 eV per reaction. On the dayside, translational kinetic energy deposited into the O_2^+ by atmospheric chemistry is not sufficient to balance the energy lost to collisions with neutrals. On the nightside, the parametric fit to the ion temperature profile decreases with altitude between about 80 km and 110 km, then starts increasing, causing thermal conductivity to dominate over collisional cooling at the lowest altitudes. The chemical heating rate drops to zero because of the lack of photoionization. Chemical heating apparently cannot explain the observed temperature differences. Even if 100% of the energy released during the reaction is assumed to be deposited as heat, with no energy partitioned to internal excitation, the chemical heating rate is orders of magnitude lower than the cooling rate and any energy gained from the chemistry is quickly transferred to the neutrals.

Coulomb collisions with electrons

Ions can be preferentially heated by Coulomb collisions with thermal electrons if electrons deposit energy into ions faster than the ions transfer energy into neutrals via collisions. However, the heating rate due to Coulomb collisions (red line in Figure 3.11) is orders of magnitude lower than the estimated cooling rates due to elastic and inelastic collisions (blue line) or thermal conduction (green line).

In addition to thermal electrons, photoelectrons may be important to the ionospheric energy balance. We investigated whether collisions with photoelectrons, which have much higher energies than the thermal electron population, could preferentially heat the ions. [83] state that the transfer rate of energy from photoelectrons to ions is negligible. This can be explained by a small collision cross-section. Expressions for the energy loss of a test particle in a plasma [51] depend on the ratio of the velocities of the test particle and ambient particles, with the largest cross-section occurring when the ratio is of order unity. Because photoelectrons travel much faster than thermal ions, the cross-section is very small and the energy transfer is inefficient.

Energy transport by ions

We used the [65] model to investigate whether adiabatic expansion or ion advection, which can transport heat vertically, could explain the observed ion temperatures. By setting the transport terms equal to the cooling rate, it is possible to derive plasma velocity profiles as a function of altitude. However, the resulting ion velocity profiles required to maintain the observed ion temperatures are nonphysical, approaching the speed of light near the ionospheric main peak.

Joule heating

In the terrestrial ionosphere, electric fields push ions through the neutral gas, creating drag and heating the ions. [84] provide expressions to calculate ion temperatures as a function of neutral temperature and the electric and magnetic field vectors (Equations 5.35–5.37). In order to explain the temperature difference of ∼130 K observed at the highest CO_2 densities during DD 8, we find that a bulk differential velocity of hundreds of meters per second is required, corresponding to an electric field on the order of 1 mV/m.

At Earth, convection electric fields can be mapped downwards along magnetospheric magnetic field lines, creating powerful electric fields deep in the ionosphere. No clear candidate exists for an electric field to drive strong differential ion flows at Mars, which lacks a global magnetic field. The ambipolar electric field created by the electron pressure gradient has been estimated at the order of μV/m based on MAVEN measurements in the ionosphere [96, 3]. Model predictions indicate that the fields induced by the interaction with the solar wind are similarly insufficient in magnitude; [20] showed that the $-\vec{u} \times \vec{B}$ force will be of similar magnitude to the ambipolar field in the ionosphere, while the $\vec{J} \times \vec{B}/ne$ force will

be much weaker. Neutral winds may also drive ionospheric currents. We used profiles of ionospheric conductivity and current density modeled by [58] to estimate the strength of electric fields in current systems driven by neutral winds at the order of 1 μV/m. None of these electric fields is strong enough for Joule heating to explain the temperature difference.

Localized interactions with crustal magnetic fields or electromagnetic waves

While Mars lacks a global magnetic field, portions of its crust are strongly magnetized, and magnetic fields in the upper atmosphere can reach thousands of nanoTeslas in magnitude [1]. Crustal fields are mainly concentrated in the Southern hemisphere, meaning that ionospheric plasma could be heated in certain geographic locations with strong crustal magnetic fields. In strong field regions, O_2^+ becomes magnetized and flows along magnetic field lines, meaning that neutral winds blowing across field lines can set up relative motion between ions and neutrals. If this were the case, then temperatures measured near crustal fields should be warmer and more variable than temperatures measured away from crustal fields. In Figure 3.7, we compare temperature profiles measured during DDs 8 and 9, which occurred at similar local times. The periapsis of DD 9 was located in the Southern hemisphere near the strong crustal field regions, while DD 8 was in the Northern hemisphere. We see no evidence of significantly warmer, more variable ion temperatures near crustal fields.

Electromagnetic waves have been shown as a viable heat source for ionospheric plasma by both models [4] and MAVEN data [31]. However, all evidence to date suggests that electromagnetic waves damp and deposit their energy to the ionospheric constituents well above the exobase region, and are an unlikely sustained heating source at the ionospheric peak.

In situ heating by particles reflected off the spacecraft

The difficulties in measuring in situ plasma parameters due to the interaction of spacecraft with ambient plasma have been under study for decades [18, 91, 49]. These issues range from the relatively simple acceleration of plasma by a charged surface, to the generation of a complex cloud of plasma surrounding the spacecraft and interacting with the environment. MAVEN's orbital velocity is about 4 km/s at periapsis, too slow to result in impact ionization of CO_2; however, it is possible that particles reflect off the spacecraft, travel back upstream and heat the ions that STATIC then measures.

The reflected ion heating rate should depend on spacecraft attitude: a larger surface area in the ram direction would reflect more particles and lead to more heating. As described in Section 3.2, we have investigated the effect of spacecraft attitude on temperature profiles during MAVEN's nominal science orbit, with periapsis at 150 km. We find no systematic difference in temperatures measured in different spacecraft orientations in the nominal orbit. It is possible that the effect only becomes significant at Deep Dip altitudes.

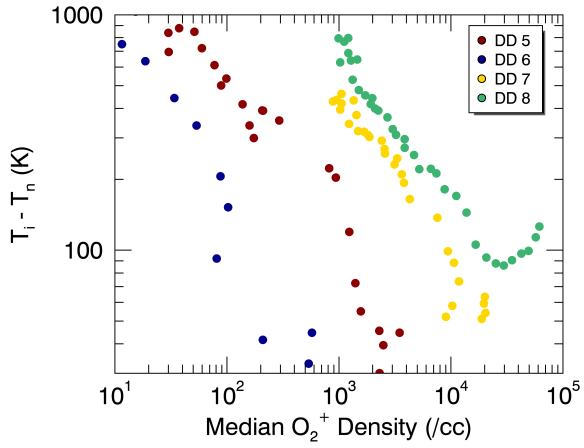

Figure 3.12: Median temperature discrepancy between ions and neutrals vs ion density. Considering all four DDs, the temperature discrepancy is not a function of ion density, which would be expected if the discrepancy were caused by reflected ion heating.

In addition to spacecraft attitude, the reflected ion heating rate is expected to be a function of ion density because larger temperature discrepancies were observed in the denser dayside ionosphere than on the nightside. In Figure 3.12, we have binned values of the difference between ion and neutral median temperatures by median ion density, which varies with the different Deep Dips. The local minimum observed in the discrepancy profiles is expected because the neutral temperature decreases at the highest CO_2 densities. While the temperature discrepancy and ion density are generally anti-correlated, the discrepancy does not appear to be a function of ion density when all the Deep Dips are considered together.

Heating of ionospheric plasma by particles reflected off the spacecraft is therefore unlikely to explain the temperature discrepancy.

Unidentified instrumental errors

It is possible, but unlikely that the measured discrepancy is due to an uncorrected instrumental effect or a systematic error introduced during data calibration. NGIMS temperatures are measured to be generally in agreement with temperatures measured by the MAVEN accelerometer experiment [97] and other measurements by accelerometers, landers, and remote sensing investigations [86]. While no comparable dataset exists to validate STATIC data, extensive steps have been taken by the team to identify instrumental effects that could impact ion temperatures, as described in Section 3.2. The value of T_{AC} can be adjusted to remove discrepancies between ion and neutral temperatures on any given orbit; however, applying these adjusted calibrations to other orbits produces results that are obviously incorrect, including negative temperatures. It is not possible to systematically correct the ion temperature with a single fixed algorithm to remove discrepancies with neutral temperatures on a by-orbit basis.

3.5 Summary and Conclusion

We have used two independent methods to calculate thermal ion temperatures at Mars for the first time since the Viking lander descents in 1976. We find that dayside profiles show little variability below the exobase region; above the exobase, electromagnetic forces and wave heating cause temperatures to vary from orbit to orbit. On the nightside, variability is more common at all altitudes due to the patchy nature of the nightside ionosphere. Our future work will use the methods described here to calculate ion temperatures for over 10,000 MAVEN orbits spanning wide ranges of latitude, local time, Mars season, and solar conditions.

Analysis of STATIC data show that ion temperatures are enhanced over neutral temperatures by typically dozens of K at periapsis, a difference that is statistically significant. Our rigorous methods for validating STATIC ion temperatures through simulations and observational procedures provide us with confidence that the derived ion temperatures are correct. Subsequent analysis has eliminated several possible mechanisms that may cause this temperature difference, including photoionization, chemical heating, Coulomb collisions with electrons, Joule heating, energy transport by ions, heating by plasma waves or crustal fields, and heating by ions reflected off the spacecraft. The source of the energy sustaining the higher ion temperatures remains unclear.

The unexpected enhancement of ion temperatures over neutral temperatures in Mars' lower ionosphere reveals a gap in our understanding of thermalization in planetary ionospheres. The authors are not aware of any simultaneous in situ measurements of ion, neutral, and electron temperatures in the terrestrial ionosphere. A mission to measure these quanti-

ties in the terrestrial ionosphere is a logical next step in addressing the questions raised by this study.

The focus of this chapter has been the development of techniques to accurately measure cold ion temperatures from velocity distribution functions, and the application of those techniques to a subset of MAVEN data collected near the main ionospheric peak. In the next chapter, we will apply the techniques developed here to more than 10,000 orbits worth of MAVEN data in order to conduct a statistical study of ion temperatures at Mars. We will also develop further tools for analyzing velocity distribution functions in an automated fashion by identifying the presence of suprathermal ions. These techniques will be used to study the evolution of the ion velocity distribution function with altitude at different locations in the Mars environment.

Chapter 4

Properties of O_2^+ distribution functions at Mars

4.1 Introduction

Having thoroughly explored the use of electrostatic analyzers in measuring properties of space plasmas, we are ready at last to conduct a statistical study of major ion distributions under a large variety of conditions at Mars. The majority of the remainder of this chapter was published in the Geophysical Research Letters in 2022 under the title "MAVEN-STATIC Observations of Ion Temperature and Initial Ion Acceleration in the Martian Ionosphere" [46].

Mars has lost most of its atmosphere through escape to space, which has played a critical role in the planet's climate evolution [52]. Although most atmospheric neutrals are cold and heavy, so that Jeans escape is negligible, photochemistry in the thermosphere produces some hot neutral species that can escape in appreciable quantities [39, 10, 59]. In the current epoch, this photochemical escape is the dominant loss process, but observations have shown that ion escape could account for as much as 30% of the total loss [61, 52, 78]. However, ions are created from the neutral atmosphere through photoionization or impact ionization, typically at energies far below the energy needed to escape the planet's gravity [84]. The processes through which planetary ions are accelerated to escape energy at Mars (4.2 eV for O_2^+) have not yet been fully identified and quantified.

Some steps in the process of ion acceleration are understood. Because the major source of ions is ultimately the cold neutral atmosphere ($\sim$200 K in the dayside ionosphere [86]), Jeans escape of the highest energy ions can remove only a small fraction of the gravitationally bound thermal ion population. The ambipolar electric field, generated by the difference in thermal velocities of ions and electrons, accelerates ions upward and provides a boost to Jeans escape [24]. The total potential drop due to the ambipolar field in Mars' ionosphere has been estimated to be $<$1.5 V [96, 3], not enough to accelerate most ions to escape energy. The solar wind convection electric field can energize ions above the exobase, in addition to

electromagnetic waves [21, 27]. Case studies have shown that wave heating can lead to the development of suprathermal ion tails at Mars, e.g. [14, 34, 33]. However, the processes that form these suprathermal tails and their importance for ion escape are not yet fully understood.

This paper is the first step in comprehensively addressing the problem of suprathermal tail formation by determining in statistical fashion where suprathermal ion populations are observed in data collected by the Mars Atmosphere and Volatile EvolutioN (MAVEN) mission [54]. We also present ion temperature profiles as a function of solar zenith angle (SZA) and altitude between 150 km and 500 km. Finally, we discuss variations in ion temperature and energization with changing SZA and altitude, and the effects of crustal magnetism.

4.2 A Method for Identifying Energized Ion Distributions

Data

Data used in this study were collected by MAVEN's SupraThermal And Thermal Ion Composition (STATIC) instrument [70], a toroidal top hat electrostatic analyzer with attached time-of-flight velocity analyzer. STATIC is capable of distinguishing Mars' main ionospheric and escaping species (H^+, H_2^+, He^+, C^+, O^+, O_2^+ and CO_2^+) with a field-of-view (FOV) covering 360°x90°. The energy and angular widths of measured O_2^+ velocity distribution functions are used to determine O_2^+ temperature using the method described by [45], which assumes the ions have a dominant Maxwellian component. Distribution functions and temperatures are sampled every 4 seconds and corrected for spacecraft potential and instrument effects. Details of these calibrations, including the spacecraft potential correction, are described by [45] and [32]. Data used in this paper were measured during more than 10,400 MAVEN orbits ranging from February 2016 to December 2020, excluding orbits when STATIC was in protect mode. MAVEN's precessing elliptical orbit allows periapsis to sample the full range of SZA, local time, and longitude for latitudes equatorward of 75°. We have binned the data into 25 km altitude bins and SZA bins of 10°, 20°, or 30°, as indicated in each figure, to investigate how O_2^+ distributions vary depending on these parameters. Given temperature ranges correspond to interquartile ranges of a group of binned measurements, not uncertainties in a particular measurement (typically ∼10% [45]).

Identification of suprathermal ions

Below the exobase (∼140-210 km [53]), high collision rates should result in rapid thermalization with neutrals, so ion distribution functions are expected to be approximately Maxwellian. After correcting for spacecraft potential, we fit the core of each measured distribution with a drifting Maxwell-Boltzmann function. The fit is performed using the IDL function "amoeba.pro," which utilizes the downhill simplex method to minimize the differ-

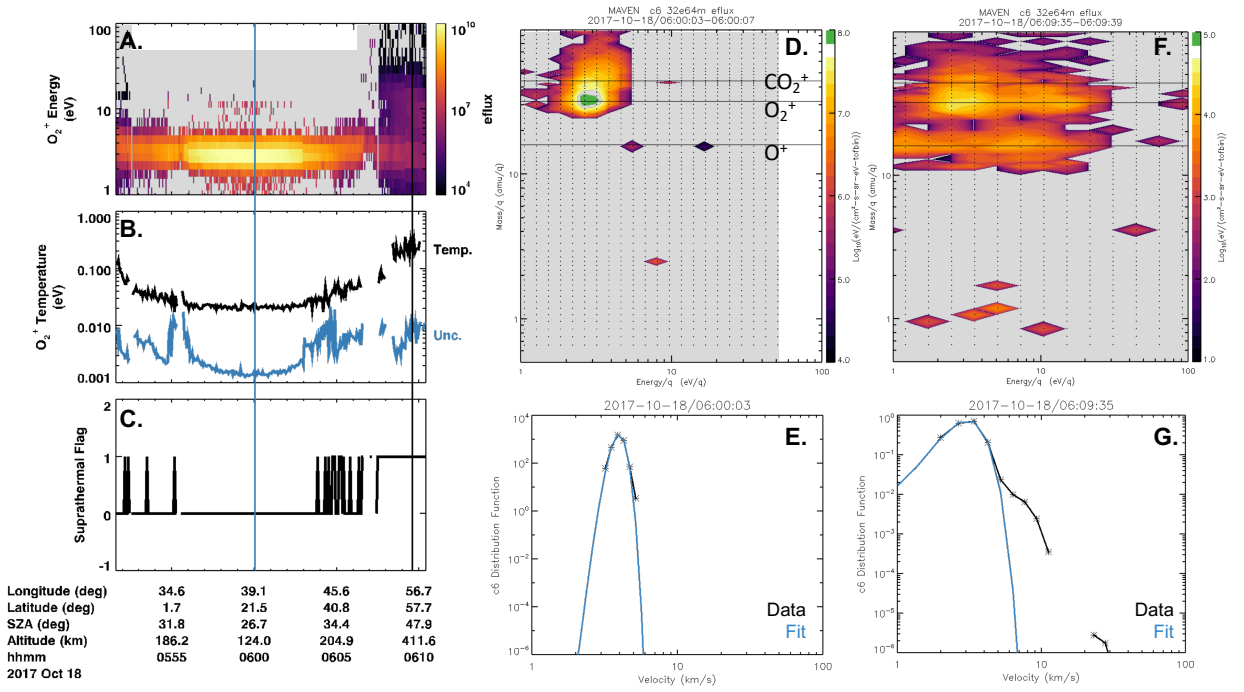

Figure 4.1: An example of STATIC data for one periapsis pass. Panel A: O_2^+ energy flux (eV/cm^2/s/steradian/eV). Panel B: O_2^+ temperature (black) and statistical uncertainty (blue). Panel C: A flag where 1 (0) indicates the presence (absence) of a suprathermal population. Vertical blue and black lines in panels A-C indicate the events shown in panels D/E and F/G, respectively. Panels D and F: Differential energy flux (color scale) vs energy and mass. Dotted lines show the locations of STATIC energy bins and shading shows the extent of the energy sweep. Panels E and G: Measured velocity distribution function (symbols with black lines) for O_2^+ with Maxwell-Boltzmann fits to the core (blue).

ence between the data and the Maxwellian. The three fit parameters (density, bulk velocity, and temperature) are allowed to vary from initial inputs by 100%, 10%, and 50%, respectively. Initial inputs are determined from the amplitude, energy, and width of the peak of each distribution. Allowed ranges of variation were chosen by manually testing the fitting procedure on hundreds of distributions, including high-altitude data where the fit is expected to perform poorly. When the fit does not converge (<1% of data below 500 km), the distribution is removed from the analysis. The fit is subtracted from the data, and the energy flux (eflux) in the residual suprathermal component is compared to the eflux contained in the best-fit Maxwell-Boltzmann function to identify any suprathermal ions.

An example of STATIC data collected during a periapsis pass is shown in Figure 4.1. The pass occurred during a Deep Dip, an orbit maneuver designed to sample the ionospheric peak and to approach the well-mixed region of the atmosphere. Periapsis is located near the center

of Figure 4.1A-C. Figure 4.1A and B shows measured efluxes and temperatures for O_2^+ and Figure 4.1C shows a flag that indicates the presence of a significant suprathermal component. Shaded regions in Figure 4.1A, D, and F indicate different regions of energy space that STATIC sampled during different parts of the orbit. During the low-altitude segment, ion thermal velocities are much smaller than the spacecraft velocity, so that ions are beamed at the ram energy (2.7 eV for O_2^+); the energy sweep is subsequently restricted to energies<50 eV. At higher altitudes (>∼300 km), where suprathermal components may appear, the instrument sweeps up to 500 eV. A distribution observed near periapsis is shown in Figure 4.1D and E. In the collisional region around periapsis, a drifting Maxwellian contains nearly all measured eflux (Panel E). Above the exobase, a suprathermal tail appears (Panel F,G) that increases the density above escape energy from 0 to 10/cc (∼20% of the total density).

4.3 Evolution of the Distribution Function with Altitude

Using the fitting routine described in Section 4.2, we have separated distributions into three categories based on eflux; the fraction of distributions in each category is shown as a function of altitude and SZA in Figure 4.2. The categories are:

- Maxwellian: The fit contains >90% of the eflux of the measured distribution (Figure 4.2A).
- Significant suprathermal component: The suprathermal eflux is between 10% and 100% of the eflux in the fit to the Maxwellian core (Figure 4.2B).
- Mostly suprathermal: The suprathermal eflux exceeds the eflux in the fit (Figure 4.2C).

O_2^+ distribution functions are dominated by the Maxwellian core at all SZAs below altitudes of 150-200 km, in agreement with predictions from photochemical theory [39] that the exobase region is located there and collisions quickly thermalize ions at lower altitudes. The location of the exobase varies by tens of kilometers depending on external drivers that are averaged over in this study, such as Martian season and solar conditions [53].

The transition from collision-dominated Maxwellian distributions to distributions with a significant suprathermal component occurs between 150 and 250 km for all SZAs at Mars (Figure 4.2). Panel A shows that Maxwellian distributions dominate below ∼250 km on the dayside and below ∼175 km on the nightside, which is consistent with the variation of the exobase altitude with SZA [53]. Above this transition, only a few percent of nightside distributions are Maxwellian, but up to 40% of dayside distributions are Maxwellian up to 400 km. This difference is likely due to differences in magnetic topology between the day and night, but we defer discussion of magnetic topology to Section 4.5. In panel B, suprathermal components begin to appear above the exobase, consistent with energized ions becoming unable to thermalize due to decreasing ion-neutral collision rates. These

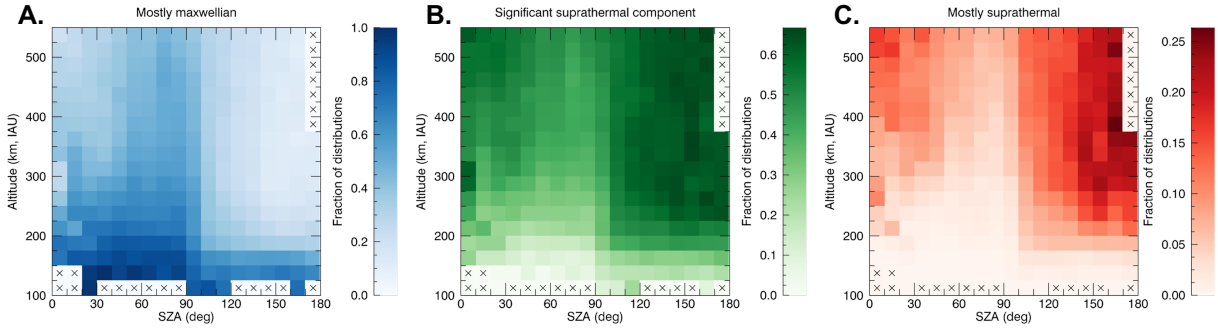

Figure 4.2: Occurrence rates for distribution functions classified as (A) mostly Maxwellian, (B) having a significant suprathermal component, or (C) mostly suprathermal as described in the text, sorted by solar zenith angle (SZA) and altitude. Each colorbar has a different upper bound. Xs indicate bins with no data.

suprathermal components are typically non-Maxwellian and appear at different energies and directions depending on their energization mechanisms. At high altitudes, non-thermal distributions are significant, especially on the night side (Panel C).

On the nightside, the transition occurs over a narrow altitude range. By 250 km, suprathermal ions are observed in most distributions. The transition region occurs over a broader altitude range on the dayside, but most distributions include suprathermal ions by ∼400 km. It is important to note that we have not compared suprathermal ion energies to escape energy to quantify the fraction of ions that can actually escape; however, the region where suprathermal ions appear is important as this marks the region where energized ions can no longer thermalize with the main population. Future work will investigate the likelihood that suprathermal ions escape to space, as well as mechanisms leading to the development of the suprathermal component at different SZAs.

4.4 Diurnal Variations in Ion Temperature

Figure 4.3A shows median ion temperatures for Maxwellian distributions as a function of altitude and SZA (line color). Ion temperatures are calculated assuming a dominant Maxwellian core using the method described by [45] for their case studies of temperature profiles. Separating distributions with significant suprathermal components before beginning a statistical analysis reduces systematic errors, which will be discussed in Section 4.6.

Figure 4.3B shows the variability in ion temperatures measured on different orbits in the same SZA-altitude bins; that is, a measure of inter-orbit variability on orbits that are not required to be consecutive, the same definition used by [32] when analyzing ion density. Variability is calculated using the interquartile range of O_2^+ temperatures in each SZA-

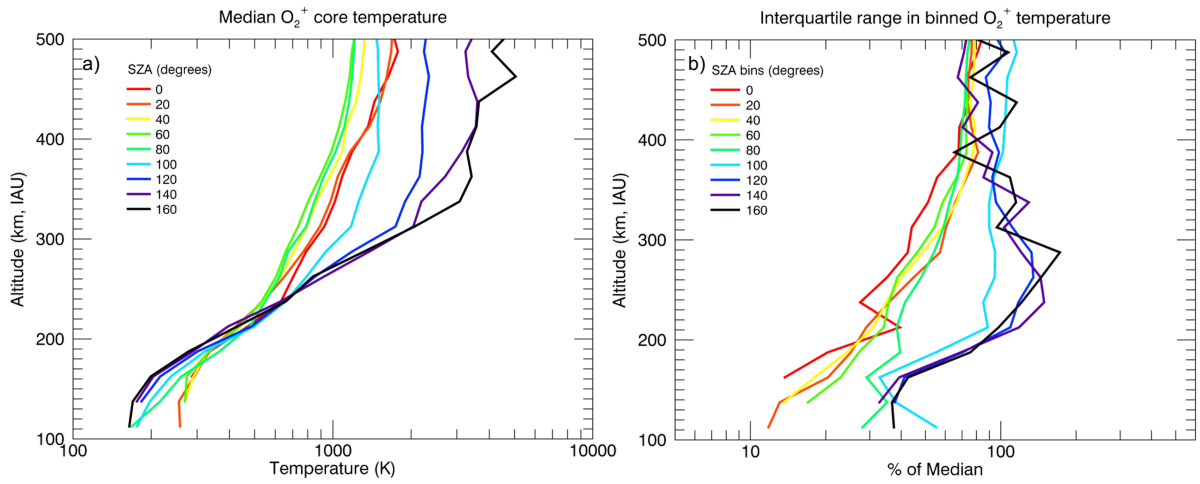

Figure 4.3: Panel A: Median temperatures for O_2^+ as a function of altitude and SZA. Panel B: Interquartile ranges of O_2^+ temperatures measured in each SZA-altitude bin, as a percentage of the median temperature in the same bin.

altitude bin.

In the collisional region below the exobase, the dayside neutral atmosphere is warmer than the nightside [86], so ions in the collisional region should also be warmer on the dayside. [45] first reported dayside ion temperatures significantly hotter than expected, suggesting that an important source of ion energy is missing from current photochemical theory. The same trend is observed using the entire MAVEN dataset in Figure 4.3. Below 180 km, temperatures decrease with increasing SZA. Near the subsolar point, the median temperature at MAVEN's nominal periapsis altitude of 150 km is 287 ± 39 K, decreasing to 261 ± 76 K near the terminator and 199 ± 84 K near the antisolar point. Inter-orbit variability is as low as 15% on the dayside and increases with SZA, up to 40% near midnight. Low dayside variability indicates highly repeatable structure there, while the higher variability on the nightside likely reflects variability in electron impact ionization, an important source of nightside plasma [84, 2].

As ion-neutral collisional cooling becomes less efficient than ion heating towards the top of the exobase region, median temperatures begin to rise more quickly with altitude at all SZAs. This behavior is also observed at Earth as Coulomb collisions with electrons and electromagnetic waves provide heat sources for ions that increase in effectiveness with altitude [84].

Above 250 km, the coldest temperatures are found near the terminator, with subsolar temperatures ∼20% higher. In this altitude region, suprathermal components are more common at low SZAs than near the terminator: median temperatures are higher (Figure 4.3A) and Maxwellian distributions are rarer for SZAs <60° (Figure 4.2). Between SZAs

of 60° and 90°, median temperatures are coldest and most distributions are Maxwellian up to 400 km. Very few distributions are mostly suprathermal, although a suprathermal component does develop up to 50% of the time above 400 km (Figure 4.2). These hot ions are likely created near the top of the collisional atmosphere and do not collide enough times to thermalize with the neutral atmosphere. The magnetic geometry of the typical solar wind interaction with the planet may explain this behavior. Below 400 km near the terminator, field lines are closed crustal loops, draped interplanetary field lines, or open to the solar wind, usually through the dayside [95]. Closed fields rotating out of the solar wind dynamic pressure expand outwards, allowing thermalized ions to reach higher altitudes than at the subsolar point. Open and draped field lines crossing the terminator also flare outwards, similarly allowing thermalized ions to reach higher altitudes in the terminator region.

On the nightside, median core temperatures are very high above 250 km (Figure 4.3A). For SZAs>100°, median temperatures increase with SZA and are hottest at midnight, reaching up to 5050 ± 3825 K while dayside temperatures remain below 1780 ± 220 K. Variability increases with altitude, reaching 50-100% of the dayside median and 100-200% of the nightside median above 250 km (∼5x more variability than at 180 km, Figure 4.3B). Maxwellian distributions represent a very small fraction of measurements at these altitudes. Nearly all nightside distributions include suprathermal ions, indicating that ion-neutral collisional coupling is less important than energization mechanisms on the nightside.

Figure 4.4 provides another way of visualizing the structure described in this section, as each temperature profile can be thought of as a horizontal slice through Figure 4.3. Diurnal variations in temperature are small in the collisional ionosphere, <100 K between noon and midnight. Diurnal changes in temperature grow with altitude up to several hundred K at 450 km. At altitudes above 200 km, the coldest temperatures are observed at dawn and dusk, a reflection of the thermalized plasma flowing up magnetic field lines near the terminator. The highest temperatures are observed on the nightside, where suprathermal ions are also observed.

4.5 Influence of Crustal Fields

Figure 4.5A and C compare O_2^+ core temperatures inside and outside regions characterized by strong crustal magnetism [1]. These regions are defined the same way as by [32]: the crustal field region covers the area of Mars' surface defined by 135° < longitude < 225°, -80° < latitude < 0°, while the non-field region covers 225° < longitude < 315°, 0° < latitude < 80°. Some fluctuations in Figure 4.5 likely result from a smaller number of samples; however, the general trends are still clear. No clear trend is observed in the collisional region below 200 km. Between 200 and 350 km, core ion temperatures are significantly reduced in crustal field regions at all SZAs (Figure 4.5C). For SZAs of 0-30° (red), crustal fields reduce temperatures by a factor of ∼10%, while nightside temperatures (dark blue) can be reduced by up to 80%.

Figure 4.6 shows the fraction of distribution functions categorized as mostly Maxwellian, significantly suprathermal, or mostly suprathermal in the strong and weak crustal field re-

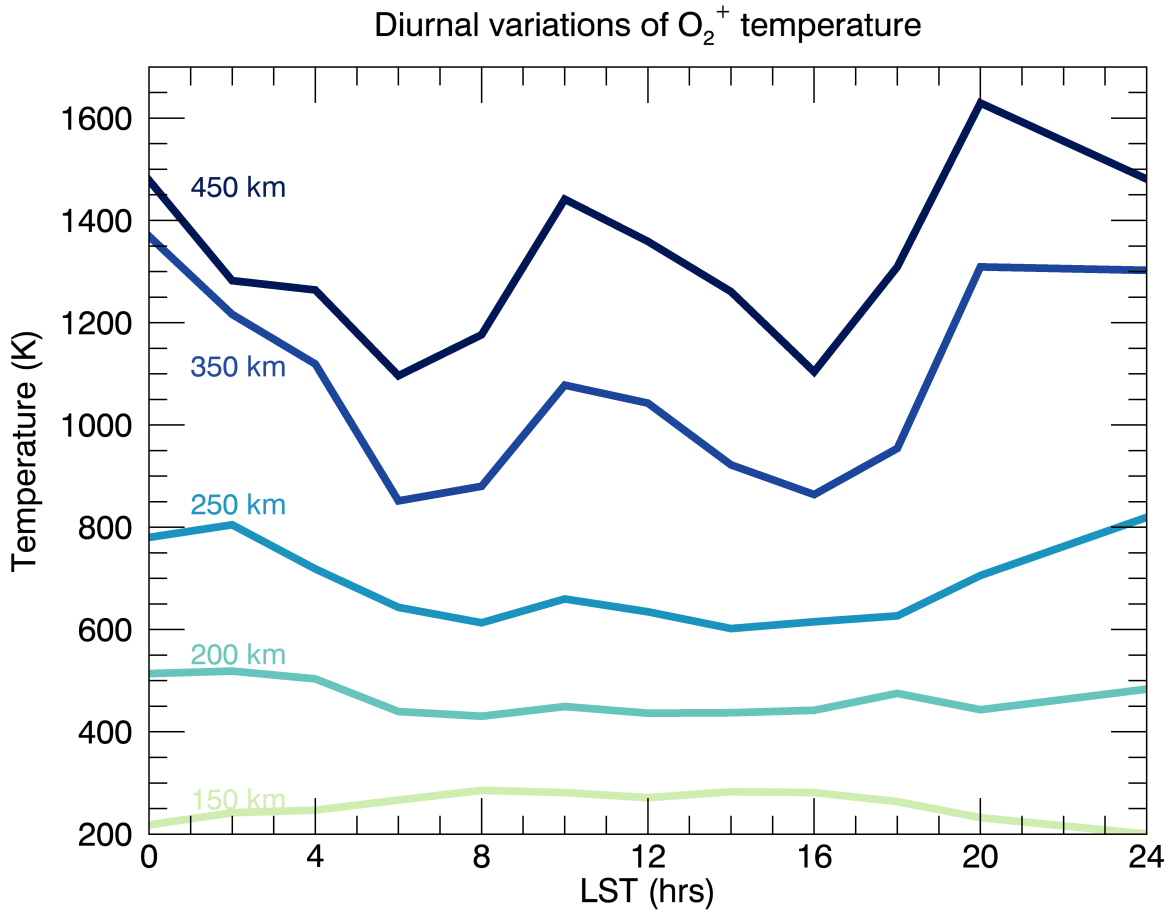

Figure 4.4: O_2^+ temperature as a function of local solar time for various altitudes in the Martian ionosphere.

gions. Above the exobase, crustal fields appear to have significantly different effects on distribution functions at different SZAs.

On the dayside, crustal fields appear to shield ionospheric O_2^+ from being energized by the solar wind interaction: inter-orbit variability is reduced inside crustal fields (Figure 4.5B). For SZAs of 0-30° (red), variability is reduced from 100% to 40% at 300 km in the strong field region. Also, the fraction of distributions that are Maxwellian is larger and extends to higher altitudes inside the strong field region (blue color in Figure 4.6G). Suprathermal components appear at lower altitudes in dayside weak field regions (red color in Figure 4.6H,I). The geometry of the crustal fields is critical in allowing thermalized ions access to higher altitudes than horizontal draped fields. In Figure 4.6G-I, suprathermal ions are observed less frequently in strong field regions all across the dayside, where crustal fields

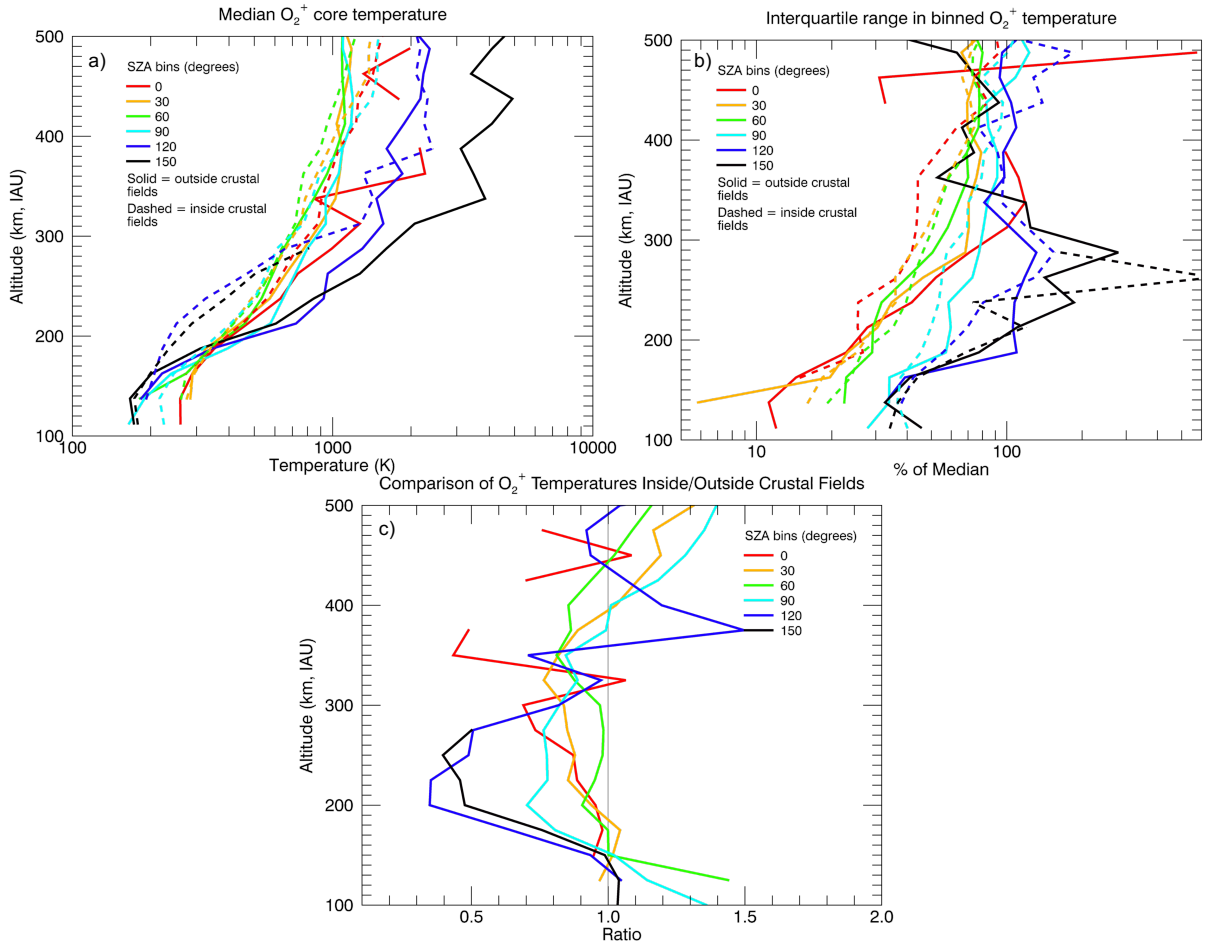

Figure 4.5: Solid and dashed lines indicate data collected away from and near crustal magnetic fields, respectively. Panel A: Median temperatures for O_2^+ as a function of altitude and SZA. Panel B: Interquartile ranges of O_2^+ temperatures measured in each SZA-altitude bin, as a percentage of the median temperature in the same bin. Panel C: The ratio of median O_2^+ temperatures inside and outside crustal field regions.

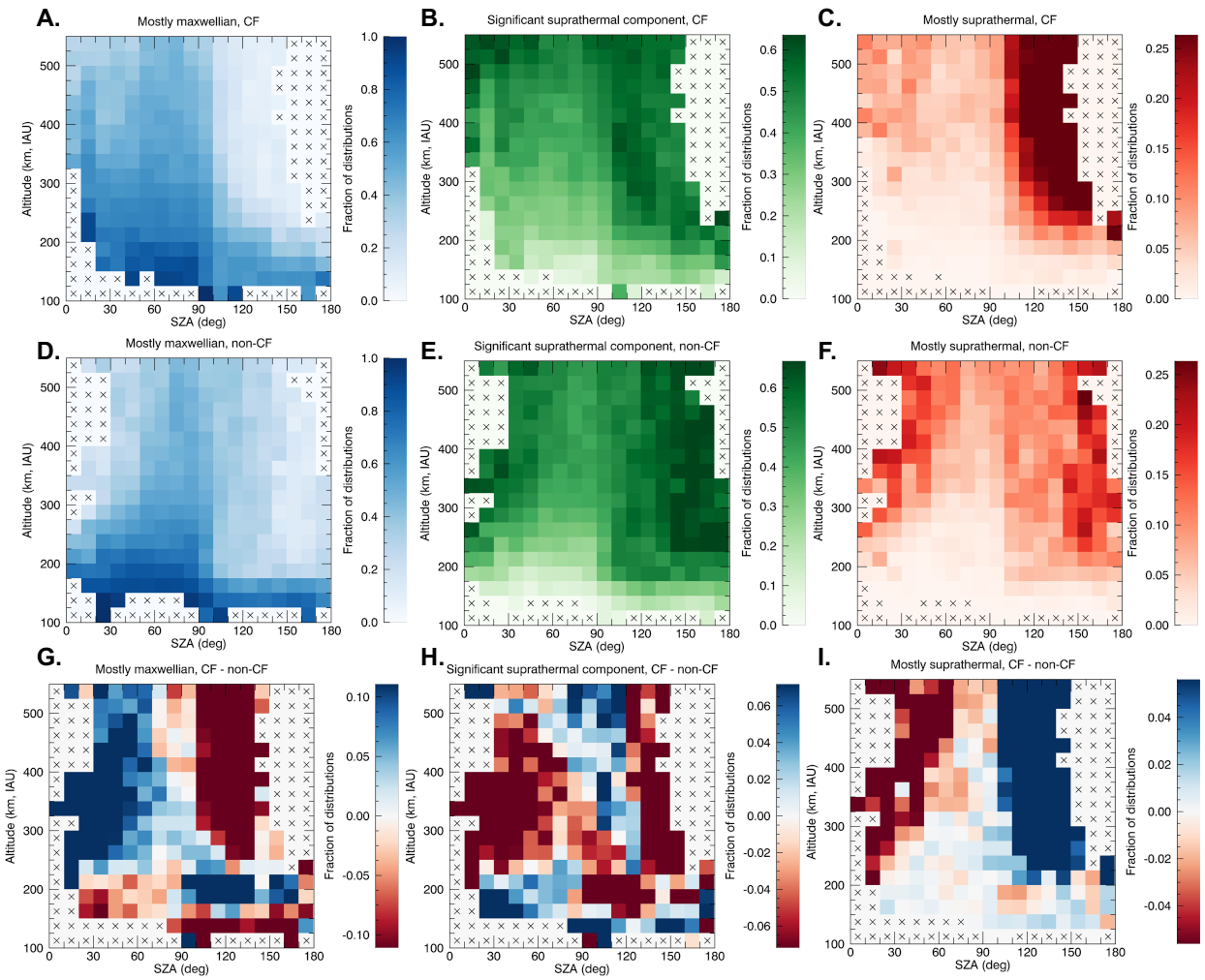

Figure 4.6: Panels A-C (D-F) are similar to Figure 2, representing data collected in the strong (weak) crustal field region defined in the text. Panels G-I are difference maps of panels A-F.

appear to protect planetary plasma from heating and acceleration.

Near the terminator between SZAs of 90° and 120° and altitudes of 150 and 300 km, Maxwellian core temperatures are colder (Figure 4.5C) and more distributions are mostly Maxwellian (Figure 4.6G) inside crustal field regions. The transition from cold to hot core temperatures is more gradual and extends to higher altitudes in crustal field regions near the terminator, occurring at lower altitudes for higher SZAs (Figure 4.5A). Together, these observations imply that thermalized dayside plasma is trapped inside closed crustal fields as they rotate past the terminator. This interpretation supports previous results, e.g. [2], that transport across the terminator is an important source of plasma at these SZAs. In contrast to the dayside, the fraction of Maxwellian distributions above 300 km inside strong crustal fields is reduced for SZAs>100° (Figure 4.6G). The increased incidence of suprathermal ions in crustal field regions suggests that crustal fields create conditions that enhance the efficiency of nightside ion energization at collisionless altitudes. Nightside thermal ions that do persist to high altitudes remain colder inside crustal fields: median core temperatures are reduced between 200 and 350 km (Figure 4.5C). This can be understood using magnetic topology. [89] showed that open topologies dominate on the nightside above 180 km for magnetic field strengths < 10 nT, while closed topologies dominate up to 500 km in stronger fields. Particle precipitation down open field lines in weak field regions can lead to higher temperatures there, and thus an apparent reduction in temperature in strong field regions. Of the closed topologies seen in strong fields, plasma voids become less common above ∼300 km, giving way to trapped electron distributions. These transitions in topology, indicating increasing efficiency of energization of planetary plasma, roughly coincide with the transitions from cold to hot nightside ions seen in Figure 4.5A. Again, magnetic topology is key for understanding trends in ion energization.

Above 350 km, the effect of crustal fields on core temperatures is less clear. The large fluctuations in Figure 4.5 make sense in the context of Figure 4.6A and D, which show that only a small fraction of distribution functions are Maxwellian above 350 km, and many bins have no data.

The effect of crustal fields on diurnal temperature variations at a fixed altitude is shown in Figure 4.7. Deep in the collisional atmosphere at 150 km, crustal fields have no clear effect on ion temperatures. However, for all altitudes near and above the exobase region, thermalized ions in strong crustal fields are much colder than ions outside these strong field regions. Again, we stress that most ions in strong crustal field regions show evidence of energization on the nightside, so cold thermal ions are a minority there; however, the cooling effect is seen at all local times, not just at night, implying that strong crustal fields do have a shielding effect on planetary plasma.

4.6 Sources of Measurement Bias

Care must be taken when interpreting ion temperatures measured above the exobase region, where suprathermal components appear in measured ion distribution functions. If multiple

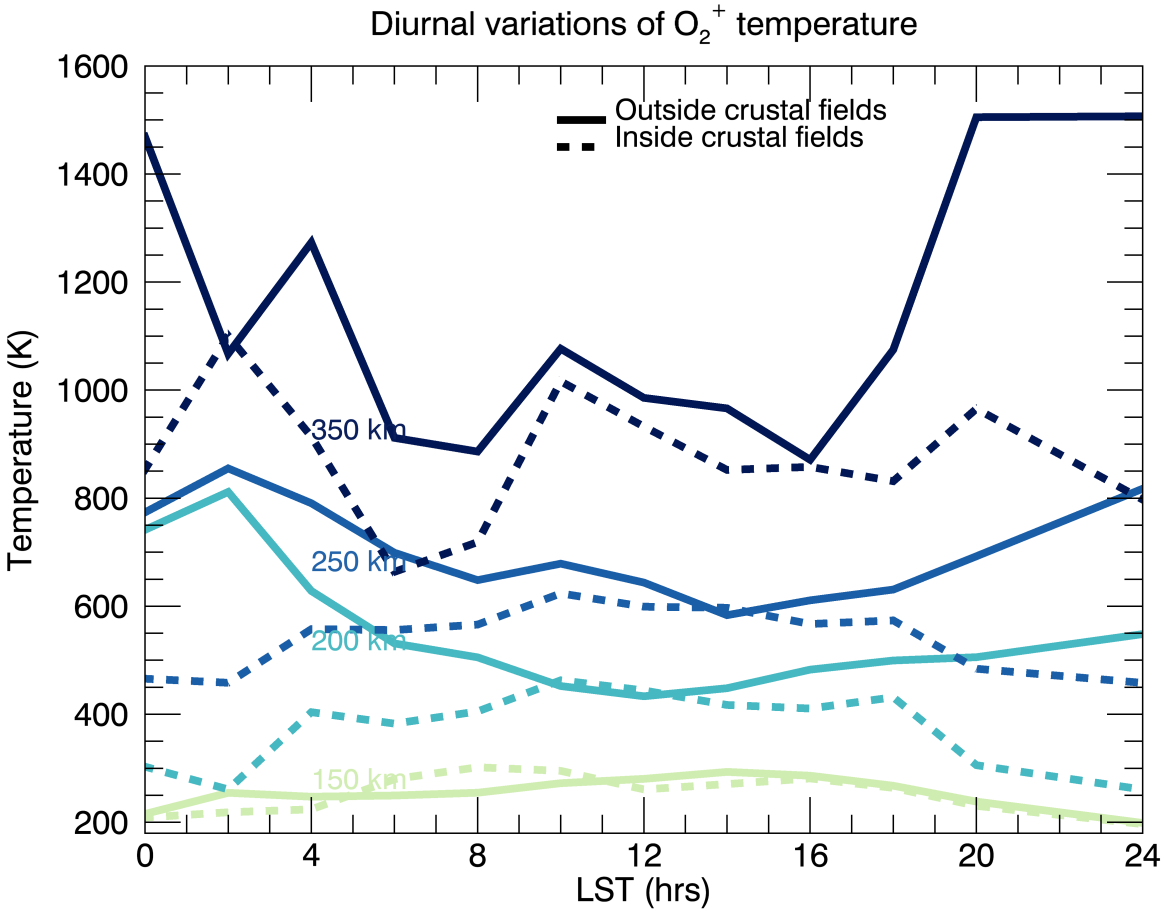

Figure 4.7: O_2^+ temperature as a function of local solar time for various altitudes in the Martian ionosphere. Again, solid and dashed lines indicate data collected away from and near crustal magnetic fields, respectively.

populations are present at different energies, or the eflux in the suprathermal portion of the distribution is significant compared to the eflux of the thermalized core, then the meaning of temperatures calculated assuming a dominant Maxwellian core becomes unclear. Data in Figures 4.3 and 4.5 are restricted to Maxwellian distributions so that the meaning of the calculated temperature is clear. Temperatures reported here should therefore be treated as a lower limit if used to calculate the amount of energy or pressure carried by the ions. Even a small fraction of suprathermal ions can represent a significant amount of energy compared to the cold core.

The most significant source of uncertainty in long-term statistical studies of STATIC data is the instrument's finite FOV, which covers 360°x90°, not the entire sky. The peak of the distribution function may lie outside the FOV and lead to an inaccurate estimate of the temperature and/or errors in categorizing the distribution function. At low altitudes when the spacecraft travels supersonically, all ions enter as a narrow beam centered on the ram direction, meaning it is straightforward to remove data collected when the instrument is mispointed and misses the beam, such as during orbits when the spacecraft communicates with Earth. At higher altitudes ($>\sim$200 km) where distributions are broader, ion flow speeds can exceed the spacecraft speed, and the spacecraft can block a portion of the FOV from which ions might enter, determining whether the peak of the distribution is in the FOV is very difficult to automate. We have used the quality flag described by [32] in order to remove data collected with incorrect pointing at low altitudes. FOV errors can be identified by manually inspecting the individual measurements made every 4 s, but this is unfeasible for a statistical study. We report median values and interquartile ranges rather than averages and standard deviations, which can be influenced by outliers, in an attempt to minimize the effect of FOV errors on altitude profiles.

Uncertainty in the categorization of distribution functions may also result from the fitting procedure. Entirely non-Maxwellian distribution functions, for which the fit described in Section 2.2 does not converge, are not represented in Figures 4.2 and 4.6. Such distribution functions are a small fraction of the dataset ($<$1% below 500 km) and are almost never observed below the exobase. We thus expect uncertainties in the percentages of distributions in each category reported in Figures 4.2 and 4.6 to be on the order of a few percent. The smooth transitions between categories provide confidence that our qualitative description of ion behavior is correct.

Some of the variability in Figures 4.3 and 4.5 is a result of combining data measured in different Mars seasons, solar conditions, and magnetic topologies. A future study will investigate how solar drivers (e.g. dynamic pressure, interplanetary magnetic field direction) affect O_2^+ temperatures and distribution functions.

4.7 Summary

We present a statistical investigation of O_2^+ distribution functions measured in Mars' ionosphere with MAVEN-STATIC. Drifting Maxwell-Boltzmann functions are fitted to measured

distributions in order to separate energized and thermalized distributions. The fraction of distributions categorized as Maxwellian, having a significant suprathermal component, and mostly suprathermal are presented as a function of SZA and altitude. Median temperatures for Maxwellian distributions as a function of SZA and altitude, as well as inside and outside regions of strong crustal magnetism, are also presented.

Ions are mostly Maxwellian below the exobase, in agreement with photochemical theory as collisions with neutrals are expected to rapidly thermalize the distributions. Above the exobase, ions are coldest near the terminator and hottest on the nightside; median ion temperatures increase with altitude, e.g. from 660 K at 250 km to 3650 K at 400 km on the nightside. Cold, thermalized ions reach higher altitudes near the terminator by following magnetic field lines, which tend to flare outward while approaching the terminator.

Crustal fields appear to significantly reduce the presence of suprathermal ions on the dayside, likely by shielding planetary plasma from heating and acceleration mechanisms, while enhancing ion energization on the nightside. Between 200 and 350 km, core ion temperatures are significantly reduced in crustal field regions, particularly on the nightside.

Knowledge of where ion distributions transition from Maxwellian (driven by photochemistry and collisions) to suprathermal (driven by electromagnetic forces and transport) is a crucial first step in understanding the processes that control how ions at Mars are energized and can escape to space.

Chapter 5

Summary and Conclusion

In this work we have addressed the motivation behind using electrostatic analyzers with mass resolution for the study of planetary environments. We also developed a series of tools for understanding and analyzing the data returned by such instruments, beginning with understanding how to convert counts to physical units and ending with a statistical study of ion distribution functions collected under a huge range of environmental conditions.

Chapter 1 introduced the basic physics of planetary ionospheres. We investigated how ions are produced and how energy flows in a general ionosphere, then transitioned into specific properties of the Martian hybrid magnetosphere. Finally we introduced the concept of the electrostatic analyzer with attached time-of-flight velocity analyzer, and motivated why such instruments are ideal for studying planetary ionospheres.

In Chapter 2, we made a case study of the SupraThermal And Thermal Ion Composition (STATIC) instrument at Mars in order to understand the principles behind operating ESAs and TOF analyzers in space. We derived expressions for the energy passband and geometric factor of an ESA. Sources of background counts, correction for spacecraft potential, and the generation of different data products were described in detail. We emphasized the importance of ensuring the instrument is suitable for the ambient environment, including analyzing examples of data where the instrument biased the measurement of the velocity distribution function.

Chapter 3 developed methods for analyzing velocity distribution functions, specifically two independent methods to calculate thermal ion temperatures. The methods include corrections for instrument response and internal scattering. These techniques were used to conduct a case study of the MAVEN Deep Dips and extract the first measurements of Martian thermal ion temperatures since the Viking lander descents in 1976. Ion temperatures were found to be enhanced over neutral temperatures by typically dozens of K, deep in the collisional atmosphere below the exobase region. We showed that no known mechanism could easily explain the sustained temperature difference, excluding photoionization, chemical heating, Coulomb collisions with electrons, Joule heating, energy transport by ions, heating by plasma waves or crustal fields, and heating by ions reflected off the spacecraft as possible explanations. The source of the energy sustaining the higher ion temperatures

remains unclear.

Finally, in Chapter 4, we applied the methods discussed in the previous chapters to conduct a statistical investigation of O_2^+ distribution functions in Mars' ionosphere. Temperature profiles extending the case study from Chapter 3 to over 10,000 MAVEN orbits were reported. The evolution of thermal and suprathermal ion distributions with altitude was also investigated; suprathermal ions were shown to appear just above the top of the collisional atmosphere at all solar zenith angles. Additionally, the effects of crustal fields on the ion distribution function were investigated. We showed that crustal fields are likely to shield cold planetary plasma on the dayside while creating conditions that are favorable for energization and outflow on the nightside.

Knowledge of where ion distributions transition from Maxwellian (driven by photochemistry and collisions) to suprathermal (driven by electromagnetic forces and transport) is a crucial first step in understanding the processes that control how ions at Mars are energized and can escape to space. Such knowledge can only be achieved with instruments capable of measuring mass-resolved three-dimensional ion velocity distribution functions with sufficient field-of-view and time cadence to resolve the main characteristics of the distribution. The environmental interactions of instruments capable of making such measurements must be carefully considered by experimenters so that the data can be accurately analyzed. It is our hope that this work can serve as a useful manual for experimenters using STATIC-like instruments in the future, so that the techniques developed here can be applied to data from other missions.

In addition to motivating the use of ESAs with mass resolution for the study of planetary environments, we have taken a significant step towards answering the fundamental question of how ions gain the energy to escape from Mars. With STATIC data, we have, for the first time, the ability to directly study the evolution of the ion velocity distribution function at many different locations in Mars' space environment. These data have helped to form a more complete picture of cold ion outflow at Mars than at our own planet. We have shown that the mystery of ion outflow begins well below the exobase, with ions that are significantly hotter than the neutral atmosphere even in regions with strong collisional coupling. We have also shown that significant energization begins right at the top of the collisional atmosphere, as soon as ions can no longer deposit energy into the neutrals, and we have demonstrated that crustal fields are likely to strongly influence the efficiency of ion energization.

While we have made a good start towards forming a more complete picture of ion escape from Mars, many open questions remain. Is there an analogy to be made between ion energization at Mars and Earth? At Earth, ions experience heating perpendicular to the magnetic field through wave-particle interactions at low altitudes. As ions rise in altitude due to the gradient of the magnetic field or the mirror force, the first adiabatic invariant is conserved so that low-altitude perpendicular heating manifests as conic ion distributions streaming parallel to the magnetic field at high altitudes. While Mars lacks a global magnetic field, its remnant crustal magnetism may provide regions where a similar series of events can occur. However, much of Mars' ionosphere is very weakly magnetized. What processes lead to ion energization in the different regions of the magnetosphere? Are wave-particle inter-

actions responsible for forming suprathermal tails on ion distributions, and how important are these tails to the ion escape rate? How do solar cycle effects, seasonal effects, crustal magnetism, and magnetic topology affect the occurrence of different energization processes and their relative efficiencies? The statistical studies discussed above provide insight into where case studies should be focused in order to analyze the physical processes depositing energy into ions in the Martian ionosphere. My future work will include case studies of specific ion acceleration events in order to identify different ion energization processes, their efficacy, and the conditions under which they are likely to occur. Additionally, I aim to find ways of quantifiably characterizing suprathermal ion distributions. Can distributions with a suprathermal component be well-described by bi-Maxwellian distributions, or kappa distributions, or are they more complex? Are suprathermal tails observed coming from the same direction as the thermal population, or from some other direction (e.g. aligned with the magnetic field direction)? Are suprathermal tails produced from the thermal population, or are they the result of precipitating ions mixing with the thermal population?

The questions raised in this thesis focus on the processes energizing ions at and above the exobase region of the Martian atmosphere. However, similar processes are likely active in many planetary and exoplanetary ionospheres, meaning that analysis of the MAVEN dataset can continue to inform the planetary science community for decades to come.

Bibliography

[1] M. H. Acuña et al. "Global distribution of crustal magnetization discovered by the Mars Global Surveyor MAG/ER experiment". In: *Science* 284.5415 (1999), pp. 790–793. ISSN: 00368075. DOI: 10.1126/science.284.5415.790.

[2] D. Adams et al. "Using Magnetic Topology to Probe the Sources of Mars' Nightside Ionosphere". In: *Geophysical Research Letters* 45.22 (2018), pp. 12, 190–12, 197. ISSN: 19448007. DOI: 10.1029/2018GL080629.

[3] H. Akbari et al. "Ambipolar Electric Field in the Martian Ionosphere: MAVEN Measurements". In: *Journal of Geophysical Research: Space Physics* 124.6 (2019), pp. 4518–4524. ISSN: 21699402. DOI: 10.1029/2018JA026325.

[4] L. Andersson, R. E. Ergun, and A. I.F. Stewart. "The Combined Atmospheric Photochemistry and Ion Tracing code: Reproducing the Viking Lander results and initial outflow results". In: *Icarus* 206.1 (2010), pp. 120–129. ISSN: 00191035. DOI: 10.1016/j.icarus.2009.07.009.

[5] S. Barabash et al. "The Analyzer of Space Plasmas and EneRgetic Atoms (ASPERA-3) for the Mars Express mission". In: *Space Science Reviews* 126.1-4 (2006), pp. 113–164. ISSN: 00386308. DOI: 10.1007/s11214-006-9124-8.

[6] S. W. Bougher et al. "Mars Global Ionosphere-Thermosphere Model: Solar cycle, seasonal, and diurnal variations of the Mars upper atmosphere". In: *Journal of Geophysical Research: Planets* 120 (2015), pp. 311–342. DOI: 10.1002/2014JE004715.

[7] D. A. Brain et al. *Solar Wind Interaction and Atmospheric Escape*. Ed. by Robert M. Haberle et al. Cambridge Planetary Science. Cambridge University Press, 2017, pp. 464–496. DOI: 10.1017/9781139060172.015.

[8] D. A. Brain et al. "The spatial distribution of planetary ion fluxes near Mars observed by MAVEN". In: *Geophysical Research Letters* 42.21 (2015), pp. 9142–9148. DOI: https://doi.org/10.1002/2015GL065293.

[9] C. W. Carlson et al. "An instrument for rapidly measuring plasma distribution functions with high resolution". In: *Advances in Space Research* 2.7 (1982), pp. 67–70.

[10] M. Chaffin et al. "Elevated atmospheric escape of atomic hydrogen from Mars induced by high-altitude water". In: *Nature Geoscience* 10 (2017), pp. 174–178. DOI: 10.1038/NGEO2887.

[11] S. Chapman. "The absorption and dissociative or ionizing effect of monochromatic radiation in an atmosphere on a rotating Earth". In: *Proceedings of the Physical Society* 43.1 (1931), pp. 26–45. ISSN: 09595309. DOI: 10.1088/0959-5309/43/1/305.

[12] E. Chassefière and F. Leblanc. "Mars atmospheric escape and evolution; interaction with the solar wind". In: *Planetary and Space Science* 52.11 (2004), pp. 1039–1058. ISSN: 00320633. DOI: 10.1016/j.pss.2004.07.002.

[13] R. H. Chen, T. E. Cravens, and A .F. Nagy. "The Martian Ionosphere in Light of the Viking Observations". In: *Journal of Geophysical Research* 83.A8 (1978), pp. 3871–3876.

[14] G. Collinson et al. "Solar Wind Induced Waves in the Skies of Mars: Ionospheric Compression, Energization, and Escape Resulting From the Impact of Ultralow Frequency Magnetosonic Waves Generated Upstream of the Martian Bow Shock". In: *Journal of Geophysical Research: Space Physics* 123 (2018), pp. 7241–7256. DOI: 10.1029/2018JA025414.

[15] J. E. P. Connerney et al. "The global magnetic field of Mars and implications for crustal evolution". In: *Geophysical Research Letters* 28.21 (2001), pp. 4015–4018.

[16] J. E. P. Connerney et al. "The MAVEN Magnetic Field Investigation". In: *Space Science Reviews* 195 (2015), pp. 257–291. DOI: 10.1007/s11214-015-0169-4.

[17] J. Cui et al. "Analysis of Titan's neutral upper atmosphere from Cassini Ion Neutral Mass Spectrometer measurements". In: *Icarus* 200.2 (2009), pp. 581–615. ISSN: 10902643. DOI: 10.1016/j.icarus.2008.12.005.

[18] S. E. DeForest. "Spacecraft charging at synchronous orbit". In: *Journal of Geophysical Research* 77.4 (1972), pp. 651–659. ISSN: 0148-0227. DOI: 10.1029/ja077i004p00651.

[19] C. Dong et al. "Solar wind interaction with Mars upper atmosphere: Results from the one-way coupling between the multifluid MHD model and the MTGCM model". In: *Geophysical Research Letters* 41.8 (2014), pp. 2708–2715. ISSN: 19448007. DOI: 10.1002/2014GL059515.

[20] Y. Dong et al. "Localized Hybrid Simulation of Martian Crustal Magnetic Cusp Regions". In: *EPSC-DPS Joint Meeting*. Geneva, Switzerland, 2019.

[21] Y. Dong et al. "Strong plume fluxes at Mars observed by MAVEN: An important planetary ion escape channel". In: *Geophysical Research Letters* 42 (2015), pp. 8942–8950. DOI: 10.1002/2015GL065346.Received.

[22] E. Dubinin et al. "Field-aligned currents and parallel electric field potential drops at Mars. Scaling from the Earth' aurora". In: *Planetary and Space Science* 56.6 (2008), pp. 868–872.

[23] R. E. Ergun et al. "Dayside electron temperature and density profiles at Mars: First results from the MAVEN Langmuir probe and waves instrument". In: *Geophysical Research Letters* 42.21 (2015), pp. 8846–8853. ISSN: 19448007. DOI: 10.1002/2015GL065280.

[24] R. E. Ergun et al. "Enhanced O2+ loss at Mars due to an ambipolar electric field from electron heating". In: *Journal of Geophysical Research: Space Physics* 121 (2016), pp. 4668–4678. DOI: 10.1002/2016JA022349.Received.

[25] R. E. Ergun et al. "In-Situ Measurements of Electron Temperature and Density in Mars' Dayside Ionosphere". In: *Geophysical Research Letters* 48.14 (2021), pp. 1–10. ISSN: 19448007. DOI: 10.1029/2021GL093623.

[26] R. E. Ergun et al. "Kinetic Modeling of Langmuir Probes in Space and Application to the MAVEN Langmuir Probe and Waves Instrument". In: *Journal of Geophysical Research: Space Physics* 126.3 (2021), pp. 1–17. ISSN: 21699402. DOI: 10.1029/2020JA028956.

[27] R. E. Ergun et al. "Role of plasma waves in Mars' atmospheric loss". In: *Geophysical Research Letters* 33.14 (2006), pp. 3–7. ISSN: 00948276. DOI: 10.1029/2006GL025785.

[28] J. V. Evans. " Cause of the midlatitude winter night increase in f 0 F 2 ". In: *Journal of Geophysical Research* 70.17 (1965), pp. 4331–4345. DOI: 10.1029/jz070i017p04331.

[29] K. Fallows, P. Withers, and M. Matta. "An observational study of the influence of solar zenith angle on properties of the M1 layer of the Mars ionosphere". In: *Journal of Geophysical Research: Space Physics* 120.2 (2015), pp. 1299–1310. ISSN: 21699402. DOI: 10.1002/2014JA020750.

[30] K. Fallows, P. Withers, and M. Matta. "An observational study of the influence of solar zenith angle on properties of the M1 layer of the Mars ionosphere". In: *Journal of Geophysical Research: Space Physics* 120.2 (2015), pp. 1299–1310. ISSN: 21699402. DOI: 10.1002/2014JA020750.

[31] C. M. Fowler et al. "Electric and magnetic variations in the near-Mars environment". In: *Journal of Geophysical Research: Space Physics* 122.8 (2017), pp. 8536–8559. ISSN: 21699402. DOI: 10.1002/2016JA023411.

[32] C. M. Fowler et al. "In-Situ Measurements of Ion Density in the Martian Ionosphere: Underlying Structure and Variability Observed by the MAVEN-STATIC Instrument". In: *Journal of Geophysical Research: Space Physics* 127 (2022), pp. 1–31. DOI: 10.1029/2022JA030352.

[33] C. M. Fowler et al. "MAVEN Observations of Low Frequency Steepened Magnetosonic Waves and Associated Heating of the Martian Nightside Ionosphere". In: *Journal of Geophysical Research: Space Physics* 126.e2021JA029615 (2021). DOI: 10.1029/2021JA029615.

[34] C. M. Fowler et al. "MAVEN Observations of Solar Wind-Driven Magnetosonic Waves Heating the Martian Dayside Ionosphere". In: *Journal of Geophysical Research: Space Physics* 123 (2018), pp. 4129–4149. DOI: 10.1029/2018JA025208.

[35] C. M. Fowler et al. "The first in situ electron temperature and density measurements of the Martian nightside ionosphere". In: *Geophysical Research Letters* 42.21 (2015), pp. 8854–8861. ISSN: 19448007. DOI: 10.1002/2015GL065267.

[36] J. L. Fox. "The chemistry of protonated species in the martian ionosphere". In: *Icarus* 252 (2015), pp. 366–392. ISSN: 10902643. DOI: 10.1016/j.icarus.2015.01.010.

[37] J. L. Fox, J. F. Brannon, and H.S Porter. "Upper Limits to the Nightside Ionosphere of Mars". In: *Geophysical Research Letters* 20.13 (1993), pp. 1391–1394.

[38] J. L. Fox and A. Dalgarno. "Ionization, luminosity, and heating of the upper atmosphere of Mars". In: *Journal of Geophysical Research* 84.A12 (1979), p. 7315. ISSN: 0148-0227. DOI: 10.1029/ja084ia12p07315.

[39] J. L. Fox and A. B. Hać. "Photochemical escape of oxygen from Mars: A comparison of the exobase approximation to a Monte Carlo method". In: *Icarus* 204.2 (2009), pp. 527–544. ISSN: 00191035. DOI: 10.1016/j.icarus.2009.07.005.

[40] J. L. Fox et al. "Rate coefficients for the reactions of CO2+ with O: Lessons from MAVEN at Mars". In: *Icarus* 358 (2021), p. 114186. ISSN: 0019-1035. DOI: https://doi.org/10.1016/j.icarus.2020.114186.

[41] Z. Girazian et al. "Ion Densities in the Nightside Ionosphere of Mars: Effects of Electron Impact Ionization". In: *Geophysical Research Letters* 44.22 (2017), pp. 11, 248–11, 256. ISSN: 19448007. DOI: 10.1002/2017GL075431.

[42] F. González-Galindo et al. "Seasonal and Geographical Variability of the Martian Ionosphere From Mars Express Observations". In: *Journal of Geophysical Research: Planets* 126.2 (2021), pp. 1–15. ISSN: 21699100. DOI: 10.1029/2020JE006661.

[43] J. T. Gosling et al. "Effects of a long entrance aperture upon the azimuthal response of spherical section electrostatic analyzers". In: *Review of Scientific Instruments* 49 (1978), pp. 1260–1268. DOI: 10.1063/1.1135566.

[44] S. A. Haider, K. K. Mahajan, and E. Kallio. "Mars ionosphere: A review of experimental results and modeling studies". In: *Reviews of Geophysics* 49.4 (2011), pp. 1–37. ISSN: 87551209. DOI: 10.1029/2011RG000357.

[45] K. G. Hanley et al. "In Situ Measurements of Thermal Ion Temperature in the Martian Ionosphere". In: *Journal of Geophysical Research: Space Physics* 126.12 (2021). DOI: 10.1029/2021JA029531.

[46] K. G. Hanley et al. "MAVEN-STATIC Observations of Ion Temperature and Initial Ion Acceleration in the Martian Ionosphere". In: *Geophysical Research Letters* 49.18 (2022), e2022GL100182. DOI: https://doi.org/10.1029/2022GL100182.

[47] W. B. Hanson, S. Sanatani, and D. R. Zuccaro. "The Martian ionosphere as observed by the Viking retarding potential analyzers". In: *Journal of Geophysical Research* 82.28 (1977), pp. 4351–4363. DOI: 10.1029/js082i028p04351.

[48] Y. Harada et al. "Magnetic Reconnection on Dayside Crustal Magnetic Fields at Mars: MAVEN Observations". In: *Geophysical Research Letters* 45.10 (2018), pp. 4550–4558. DOI: https://doi.org/10.1002/2018GL077281.

[49] D. E. Hastings. "A review of plasma interactions with spacecraft in low Earth orbit". In: *Journal of Geophysical Research* 100.A8 (1995), p. 14457. ISSN: 0148-0227. DOI: 10.1029/94ja03358.

[50] A. Hughes and V. Rojansky. "On the analysis of electronic velocities by electrostatic means". In: *Physical Review* 34 (1929), pp. 284–290.

[51] Y. Itikawa and O. Aono. "Energy change of a charged particle moving in a plasma". In: *Physics of Fluids* 9.6 (1966), pp. 1259–1261. ISSN: 10706631. DOI: 10.1063/1.1761835.

[52] B. M. Jakosky et al. "Loss of the Martian atmosphere to space: Present-day loss rates determined from MAVEN observations and integrated loss through time". In: *Icarus* 315.June (2018), pp. 146–157. ISSN: 10902643. DOI: 10.1016/j.icarus.2018.05.030.

[53] B. M. Jakosky et al. "Mars ' atmospheric history derived from upper-atmosphere measurements of 38 Ar/ 36 Ar". In: *Science* 355 (2017), pp. 1408–1410.

[54] B. M. Jakosky et al. "The Mars Atmosphere and Volatile EvolutioN (MAVEN) mission". In: *Space Science Reviews* 195.1-4 (2015), pp. 3–48. ISSN: 15729672. DOI: 10.1007/s11214-015-0139-x.

[55] A. M. Krymskii et al. "Effect of crustal magnetic fields on the near terminator ionosphere at Mars: Comparison of in situ magnetic field measurements with the data of radio science experiments on board Mars Global Surveyor". In: *Journal of Geophysical Research: Space Physics* 108.A12 (2003). DOI: https://doi.org/10.1029/2002JA009662.

[56] S. A. Ledvina et al. "Ion escape rates from Mars: Results from hybrid simulations compared to MAVEN observations". In: *Journal of Geophysical Research: Space Physics* 122.8 (2017), pp. 8391–8408. DOI: https://doi.org/10.1002/2016JA023521.

[57] R. J. Lillis, M. O. Fillingim, and D. A. Brain. "Three-dimensional structure of the Martian nightside ionosphere: Predicted rates of impact ionization from Mars Global Surveyor magnetometer and electron reflectometer measurements of precipitating electrons". In: *Journal of Geophysical Research: Space Physics* 116.12 (2011), pp. 1–15. ISSN: 21699402. DOI: 10.1029/2011JA016982.

[58] R. J. Lillis et al. "Modeling Wind-Driven Ionospheric Dynamo Currents at Mars: Expectations for InSight Magnetic Field Measurements". In: *Geophysical Research Letters* 46.10 (2019), pp. 5083–5091. ISSN: 19448007. DOI: 10.1029/2019GL082536.

[59] R. J. Lillis et al. "Photochemical escape of oxygen from Mars: First results from MAVEN in situ data". In: *Journal of Geophysical Research: Space Physics* 122 (2017), pp. 3815–3836. DOI: 10.1002/2016JA023525.

[60] R. Livi et al. "The Solar Probe ANalyzer—Ions on the Parker Solar Probe". In: *The Astrophysical Journal* 938.2 (2022), p. 138.

[61] R. Lundin et al. "First measurements of the ionospheric plasma escape from Mars". In: *Nature* 341 (1989), pp. 609–612.

[62] R. Lundin et al. "Plasma Acceleration Above Martian Magnetic Anomalies". In: *Science* 311.5763 (2006), pp. 980–983.

[63] Y. J. Ma et al. "Importance of Ambipolar Electric Field in Driving Ion Loss From Mars: Results From a Multifluid MHD Model With the Electron Pressure Equation Included". In: *Journal of Geophysical Research: Space Physics* 124.11 (2019), pp. 9040–9057. ISSN: 21699402. DOI: 10.1029/2019JA027091.

[64] P. R. Mahaffy et al. "The Neutral Gas and Ion Mass Spectrometer on the Mars Atmosphere and Volatile Evolution Mission". In: *Space Science Reviews* 195.1-4 (2015), pp. 49–73. ISSN: 0038-6308. DOI: 10.1007/s11214-014-0091-1.

[65] M. Matta et al. "Numerical simulations of ion and electron temperatures in the ionosphere of Mars: Multiple ions and diurnal variations". In: *Icarus* 227 (2014), pp. 78–88. ISSN: 00191035. DOI: 10.1016/j.icarus.2013.09.006.

[66] M. Mayyasi and M. Mendillo. "Why the Viking descent probes found only one ionospheric layer at Mars". In: *Geophysical Research Letters* 42.18 (2015), pp. 7359–7365. ISSN: 19448007. DOI: 10.1002/2015GL065575.

[67] M. Mayyasi et al. "Ion-Neutral Coupling in the Upper Atmosphere of Mars: A Dominant Driver of Topside Ionospheric Structure". In: *Journal of Geophysical Research: Space Physics* 124.5 (2019), pp. 3786–3798. DOI: https://doi.org/10.1029/2019JA026481.

[68] D. McComas et al. "The solar wind around Pluto (SWAP) instrument aboard New Horizons". In: *Space Science Reviews* 140.1-4 (2007), pp. 261–313. DOI: 10.1007/s11214-007-9205-3.

[69] M. B. McElroy. "Mars: An evolving atmosphere". In: *Science* 175.4020 (1972), pp. 443–445. ISSN: 00368075. DOI: 10.1126/science.175.4020.443.

[70] J. P. McFadden et al. "MAVEN SupraThermal And Thermal Ion Compostion (STATIC) instrument". In: *Space Science Reviews* 195.1-4 (2015), pp. 199–256. DOI: 10.1007/s11214-015-0175-6.

[71] M. Mendillo et al. "Modeling Mars' ionosphere with constraints from same-day observations by Mars Global Surveyor and Mars Express". In: *Journal of Geophysical Research: Space Physics* 116.11 (2011), pp. 1–22. ISSN: 21699402. DOI: 10.1029/2011JA016865.

[72] M. Neugebauer and C. Snyder. "Solar Plasma Experiment". In: *Science* 138 (3545 1962), pp. 1095–1097. DOI: 10.1126/science.138.3545.1095.b.

[73] H. Nilsson et al. "RPC-ICA: The Ion Composition Analyzer of the Rosetta Plasma Consortium". In: *Space Science Reviews* 128 (2007), pp. 671–695. DOI: 10.1007/s11214-006-9031-z.

[74] G. Paschmann and P. W. Daly, eds. *Analysis Methods for Multi-Spacecraft Data*. Noordwijk, The Netherlands: ESA Publications Division, 1998.

[75] N. B. Pickett et al. "Carbon Ion Fluxes at Mars: First Results of Tailward Flows From MAVEN-STATIC". In: *Journal of Geophsyical Research: Space Physics* 127.e2021JA029635 (2022).

[76] M. Pilinski et al. "Electron Temperature Response to Solar Forcing in the Low-Latitude Martian Ionosphere". In: *Journal of Geophysical Research: Planets* 124.11 (2019), pp. 3082–3094. ISSN: 21699100. DOI: 10.1029/2019JE006090.

[77] E. M. Purcell. "The Focusing of Charged Particles by a Spherical Condenser". In: *Physical Review* 54 (1938), pp. 818–826.

[78] R. Ramstad et al. "Ion Escape From Mars Through Time: An Extrapolation of Atmospheric Loss Based on 10 Years of Mars Express Measurements". In: *Journal of Geophysical Research: Planets* 123 (2018), pp. 3051–3060. DOI: 10.1029/2018JE005727.

[79] R. J. Redmon et al. "Dawnward shift of the dayside O+ outflow distribution: The importance of field line history in O+ escape from the ionosphere". In: *Journal of Geophysical Research: Space Physics* 117.12 (2012), pp. 1–9. ISSN: 21699402. DOI: 10.1029/2012JA018145.

[80] H Reme et al. "The Cluster ion spectrometry (CIS) experiment". In: *The cluster and phoenix missions* (1997), pp. 303–350.

[81] K. J. Roeten et al. "MAVEN/NGIMS thermospheric neutral wind observations: Interpretation using the M-GITM general circulation model". In: *Journal of Geophysical Research: Planets* 124 (2019), pp. 3283–3303.

[82] R. P. Rohrbaugh et al. "The effect of energetically produced O2+ on the ion temperatures of the Martian thermosphere". In: *Journal of Geophysical Research* 84.9 (1979), pp. 3327–3338.

[83] R. W. Schunk and P. B. Hays. "Photoelectron energy losses to thermal electrons". In: *Planetary and Space Science* 19.1 (1971), pp. 113–117. ISSN: 00320633. DOI: 10.1016/0032-0633(71)90071-7.

[84] R. W. Schunk and A. F. Nagy. *Ionospheres*. Ed. by John T. Houghton, Michael J. Rycroft, and Alexander J. Dessler. 2nd. Cambridge, United Kingdom: Cambridge University Press, 2009.

[85] G. A. Soffen and C. W. Snyder. "The First Viking Mission to Mars". In: *Science* 193.4255 (1976), pp. 759–766. DOI: 10.1126/science.193.4255.759.

[86] S. W. Stone et al. "Thermal Structure of the Martian Upper Atmosphere from MAVEN NGIMS". In: *Journal of Geophysical Research: Planets* 123.11 (2018), pp. 2842–2867. ISSN: 21699100. DOI: 10.1029/2018JE005559.

[87] E. M. B. Thiemann et al. "The MAVEN EUVM model of solar spectral irradiance variability at Mars: Algorithms and results". In: *Journal of Geophysical Research: Space Physics* 122.3 (2017), pp. 2748–2767. ISSN: 21699402. DOI: 10.1002/2016JA023512.

[88] C. W. Walter, P. C. Cosby, and J. R. Peterson. "Rovibrational product distributions of O2+ from the reaction of O+(4S) with CO2". In: *Journal of Chemical Physics* 98.4 (1993), pp. 2860–2871. ISSN: 00219606. DOI: 10.1063/1.465072.

[89] T. Weber et al. "Characterization of Low-Altitude Nightside Martian Pitch Angle Distributions". In: *Journal of Geophysical Research: Space Physics* 122 (2017), pp. 9777–9789. DOI: 10.1002/2017JA024491.

[90] T. Weber et al. "Martian Crustal Field Influence on O+ and O2+ Escape as Measured by MAVEN". In: *Journal of Geophysical Research: Space Physics* 126.8 (2021). e2021JA029234 2021JA029234, e2021JA029234. DOI: https://doi.org/10.1029/2021JA029234.

[91] E. C. Whipple. "Potentials of surfaces in space". In: *Reports on Progress in Physics* 44.11 (1981), pp. 1197–1250. ISSN: 00344885. DOI: 10.1088/0034-4885/44/11/002.

[92] P. L. Whittlesey et al. "The solar probe analyzers—electrons on the Parker Solar Probe". In: *The Astrophysical Journal Supplement Series* 246.2 (2020), p. 74. DOI: 10.3847/1538-4365/ab7370.

[93] P. Withers. "A review of observed variability in the dayside ionosphere of Mars". In: *Advances in Space Research* 44.3 (2009), pp. 277–307. ISSN: 02731177. DOI: 10.1016/j.asr.2009.04.027.

[94] M. Wüest, D. S. Evans, and R. von Steiger, eds. *Calibration of Particle Instruments in Space Physics*. Noordwijk, The Netherlands: ESA Publications Division, 2007.

[95] S. Xu et al. "A Technique to Infer Magnetic Topology at Mars and Its Application to the Terminator Region". In: *Journal of Geophysical Research: Space Physics* 124 (2019), pp. 1823–1842. DOI: 10.1029/2018JA026366.

[96] S. Xu et al. "Field-Aligned Potentials at Mars From MAVEN Observations". In: *Geophysical Research Letters* 45.19 (2018), pp. 10, 119–10, 127. ISSN: 19448007. DOI: 10.1029/2018GL080136.

[97] R. W. Zurek et al. "Application of MAVEN accelerometer and attitude control data to Mars atmospheric characterization". In: *Space Science Reviews* 195.1-4 (2015), pp. 303–317. ISSN: 15729672. DOI: 10.1007/s11214-014-0095-x.